Anisotropic Properties of a Mid-Lithospheric Discontinuity in eastern North America

Mari Farestveit

Thesis for the degree
Master of Science

Department of Earth Science
University of Bergen
June, 2017

Abstract

During the last few years the occurrence of a mid-lithospheric discontinuity (MLD) has been observed in lithospheric studies of cratons. Studies using receiver functions have focused mainly on extracting high resolution information about the depth and extent of this discontinuity. Surface wave studies detect a change in anisotropy occurring over the same interval where the MLD is mapped, but no one has yet investigated whether these two features actually coincide. The nature of the MLD could therefore be anisotropic. In this thesis I use an new database of earthquake recordings to investigate the MLD in eastern North America. The focus is primarily on station HRV near Boston, containing 486 receiver functions with good backazimuthal coverage. Through forward modeling of receiver functions and harmonic decomposition, I find that the best fit to the MLD at HRV is obtained without a velocity reduction, but with a change in anisotropy. A change from a horizontal axis of anisotropy to a plunging axis provides the simplest model to reproduce the observed HRV data. I attribute this change of anisotropy to a division between "frozen-in" anisotropy from the formation of the Appalachian chain in the upper lithosphere, and reworked fabric in the lower lithosphere from heating by the mantle plume of the Great Meteor hotspot. This interpretation implies that the fabric in the lower lithosphere is a localized phenomenon, which should be distinguished from the craton-wide MLD signal observed in North America. Regional profiles indicate a reduction of MLD signal strength towards the craton, suggesting that the lower lithospheric layer mapped in previous craton wide studies does not extend outside the craton boundaries. However, such an interpretation cannot be based on only one station, and should be tested with an expanded study of the entire eastern North America using semi-automated inversion methods.

Acknowledgements

First I would like to thank my main supervisor Professor Stéphane Rondenay, who's unstoppable enthusiasm for subsurface inquiries kept me in the field of geophysics. This thesis would not have been written without you. I would also like to thank my co-supervisor Associate Professor Henk Keers for helpful feedback and comments.

In addition to my supervisors I would like to thank the seismo-group at the Department of Earth Science (UiB) for input and feedback on presentations, Einar Mæland for interesting discussions about anisotropy, and Marthe Vestly for feedback on the writing.

I am highly grateful for all the support my family and loved ones have provided in these last years, particularly in terms of motivation and food. Finally I would like to direct a special thanks to the people who made my years as a student such a memorable time, in particular fellow students, travel companions, flatmates and studentkoret BLAK.

Contents

Chapter 1

Introduction

The history of the Earth's evolution is stored in rocks around the world, enabling us to gain insight into past and present deformation mechanisms shaping the outer shell of our planet. Some details can be investigated in the field, but a great deal of important information is contained within the subsurface. Today there is an abundance of available tools for subsurface characterization, but the use of naturally occurring earthquakes is still a popular choice (see e.g. Fouch and Rondenay (2006) for a review). Since the hypothesis of drifting continents was put forward by Alfred Wegener in 1912, considerable effort has been made to explain how the continents have formed and evolved through time. This thesis is my contribution to one piece of the great puzzle; an investigation of the presence and characteristics of a mid-lithospheric discontinuity (MLD) at a seismic station outside the North American craton.

1.1 Lithospheric discontinuities

The concept of a weak and relatively rigid lithosphere moving over a weaker asthenosphere form the basis for the plate tectonic theory (Rychert et al., 2005). The partitioning between the lithosphere and the asthenosphere can

also be seen as a thermal boundary, where the transition from conductive to convective heat transport marks the depth extent of the layer (Yuan and Romanowicz, 2010). At fast spreading ridges the lithosphere can be nearly non-existent, while under under cratonic roots it can be up to 200-250km thick (Lin and Parmentier, 1989; Yuan and Romanowicz, 2010). The depth which marks the separation of lithosphere and asthenosphere is referred to as the Lithosphere-Asthenosphere Boundary (LAB).

The lithosphere can, to first order, be considered to be a single layer, extending from the Earth's surface down to the LAB. During the last century it has however become evident through seismic studies that there are discontinuities within the lithosphere, marked by jumps in seismic velocities at a certain depth (Prodehl et al., 2013). One such boundary is the Mohorovičić discontinuity (Moho for short), a compositional boundary marking the transition from the Earth's crust to mantle (Lovering, 1958). Investigations of the Moho initiated with the discovery by Andrija Mohorovivičić in 1909, eventually leading to global maps of crustal thickness and detailed studies of the boundary properties (Prodehl et al., 2013; Reguzzoni and Sampietro, 2015; Levin et al., 2017).

Recently, a new discontinuity has been observed within the lithosphere by a range of imaging techniques (see Selway et al. (2015)). This discontinuity is called the Mid-Lithospheric Discontinuity (MLD), and is observed as a 2-10% velocity reduction at depths between 60km and 160km (Selway et al., 2015; Yuan and Romanowicz, 2010). So far, the MLD has mainly been identified within cratons, which are long-term stable continental regions with little internal deformation (Bleeker and Davis, 2004). The studied regions, i.e. Australia, Africa, and North America, are cratonic regions with very different tectonic histories, giving rise to the question about the boundary's origin (Fouch and Rondenay, 2006).

Eastern North America is a particularly interesting place to study lithospheric discontinuities, as the continent has provinces dating back to the Archean at the center, with progressively younger provinces towards the At-

lantic ocean (Hoffman, 1989; Yuan and Romanowicz, 2010). In the case of eastern North America, the nature of the boundary can be traced across different tectonic regions, and in particular be studied outside the craton. By determining the presence and potentially lateral extent of the MLD outside the craton, we acquire more information which can be used to better resolve the origin of this boundary.

1.2 Suggested origin of the MLD

The attempt to find explanations of an MLD's origin that does not necessarily depend on tectonic history is an ongoing challenge (Selway et al., 2015). Three main theories have been proposed to explain the widespread observations of an MLD: a thermal, a compositional, and anisotropy (Karato et al., 2015).

The rather consistent depth of the MLD globally could indicate that the velocity reduction has a thermal explanation, as thermal variations provide large constraint on shear wave velocity (Selway et al., 2015). Partial melt has been proposed as an explanation of the observed negative velocity gradient, but at least in the case of North America, a rigid mantle has been found to extend down to the proposed LAB at around 200km (Hansen et al., 2015). This leads to the assumption that the observed signal arise from a solid phenomenon(Selway et al., 2015). Another thermal explanation is called Elastic Accommodated Grain Boundary Sliding (EAGBS), which is the idea that the grain boundary is weakened with increased temperature, thus allowing for elastic deformation through grain boundary sliding (Karato et al., 2015). This elastic deformation leads to reduced elastic moduli, and thereby decreases the seismic velocity with depth.

The second explanation to the MLD's origin is based on a velocity change from differences in composition. The relation between iron and magnesium is the second most important factor controlling shear wave velocity (Selway et al., 2015). However, expected magnesium reductions at MLD depths have

been estimated to result in only a 2% velocity reduction, which in most cases is insufficient to explain the MLD signal (Selway et al., 2015). Another compositional suggestion is metasomatism of rocks, meaning that the composition changes due to interaction with water (Hansen et al., 2015). Such low velocity minerals could cause an abrupt velocity reduction, but for hydrous minerals to explain the occurrence of the MLD, they must be located only below the MLD (Selway et al., 2015). A solution to this is that the MLD signal arises from amphibole which is stable only above 3 GPa, a pressure threshold which matches MLD depths. This hypothesis is not supported in all regions, as some xenolith sections contain no amphibole (Selway et al., 2015)

The third suggestion to explain the MLD is that it appears in seismic studies because of an abrupt change in seismic anisotropy. This would require changes in deformational fabric and/or geometry within at depths within 60-150 km (Karato et al., 2015). Some anisotropy studies have found the discontinuity to be anisotropic, but the problem is not well resolved and requires further testing (Fischer et al., 2010).

A natural way to investigate this third possibility is to use receiver functions (e.g. Rondenay (2009)). Most studies of the MLD based on receiver functions utilize only the radial component, which is indicating the location of the boundary to high precision, but does not provide information about the boundary's anisotropic features. In North America, several studies using receiver functions have indicated the presence of a mid-lithospheric discontinuity, and surface wave studies have detected a change in anisotropy occurring over the same depth range (Rychert et al., 2005; Rondenay et al., 2017; Yuan and Romanowicz, 2010). As the anisotropic properties have not been indicated in the receiver function studies, and surface waves do not provide the exact location of anisotropic properties, we still do not know if these two features coincide.

1.3 Objective and outline

If we understand the nature of the MLD, both in terms of lateral extent and origin, then we are probably closer to resolving the ongoing debate about the ancient processes that formed the stable continents. The aim of this project is therefore to map the MLD using receiver functions from a new database of seismic events with global coverage, to see if it exhibits anisotropic features which could explain recent observations of the discontinuity.

The thesis is therefore initiated with some theory on anisotropy (Chapter 2) and seismic wave conversion (Chapter 3), prior to the description of how receiver functions and other imaging techniques can be used to map lithospheric anisotropy (Chapter 4). The study are is described in Chapter 5, followed by a description of data used in this thesis (Chapter 6). A description of the work-flow is presented in Chapter 7, along with important considerations which should be kept in mind prior to interpretation. Chapter 8 presents the main findings from synthetic modeling, which is used for investigation of data and forward modeling in Chapter 9. Chapter 10 provides a discussion of the main result obtained: a lithospheric model for the study area, and provides an interpretation of the model parameters. A summary of the main results and interpretation is presented in Chapter 11, along with some concluding remarks.

Chapter 2

Anisotropy

Anisotropy, the directional dependence of elastic properties in a medium, is a highly useful geophysical property for improved understanding of the lithosphere's composition and evolution (Babuska and Cara, 1991; Fuchs, 1977). The signature of an anisotropic signal depends on the properties of the medium it arises from, so by recognizing and understanding different anisotropic signals we have a powerful tool for subsurface investigations. The magnitude of the anisotropic signal[1] depends on the type and amount of anisotropic material in a region, thereby providing additional information about the subsurface (Christensen, 1984).

Several studies of lithospheric anisotropy have been carried out around the world in the last few decades with the goal of mapping both the amount of anisotropy, and the type of anisotropy in a region (see e.g. Fouch and Rondenay (2006) for a review). Through such studies, the presence of anisotropic layers in the crust and upper mantle have been mapped in subduction zones, oceanic basins and within the continents (Fuchs, 1977; Fouch et al., 2000). The most complex anisotropic signals arise from studies of the continental lithosphere, and the debate has been ongoing whether anisotropy resides in the lithosphere or the asthenosphere (Babuska and Cara, 1991; Levin et al.,

[1]Defined in Babuska and Cara (1991, p.187) for velocity anisotropy as "the percentage of velocity variation between the fastest and slowest directions"

1999). In recent years it has however become accepted that both the lithosphere and the asthenosphere have anisotropic features, and the problem is then to separate the contribution of anisotropy from various depths (Yuan and Romanowicz, 2010).

This chapter describes anisotropy at all scales, starting with elastic properties and crystal structure before expanding to larger scale anisotropic features found in the lithosphere and the sub-lithospheric mantle.

2.1 Anisotropic properties of solid materials

A medium is said to be anisotropic when seismic waves experience slower and faster velocities depending on the directions they traverse the medium (Babuska and Cara, 1991). The direction of highest seismic velocity is aligned with the fast axis, which is described by its direction (azimuth) and plunge (dip). The direction of and symmetry around the fast axis determines the type of anisotropy in a medium.

This directional dependence of velocity can best be described by the elastic stiffness tensor of the medium. The components of the elastic stiffness tensor C_{ijkl}, are measures of a medium's response (strain, ϵ) to applied forces (stress, σ) (where the individual components describe the strain resulting from stress in a specific direction) (Equation 2.1) (Babuska and Cara, 1991).

$$\sigma_{ij} = C_{ijkl}\epsilon_{kl} \tag{2.1}$$

As indices *ijkl* correspond to directions (xyz) relative to a coordinate system, the matrix has 3^4 (81) components. The number of independent components (n) can be interpreted as the number of individual strain responses resulting from stress applied in all directions. In the most anisotropic case n is 21, and it decreases with increasing symmetry in the medium (Babuska and Cara, 1991).

A medium can be anisotropic on a crystal scale and/or on a regional scale. In this thesis I investigate seismic anisotropy, i.e. features that are anisotropic on a scale greater than the wavelength of seismic waves (Babuska and Cara, 1991). Classification of an anisotropic medium is however based on the medium's symmetry and number of independent components in the elastic stiffness tensor, regardless of scale. For simplicity, I therefore describe the main types of axial symmetry based on crystal structure.

A simple system to describe crystal orientation is by the Bravais lattice, which can be seen as "the periodic array in which the repeated units of the crystal are arranged" (Rohrer, 2001, p.29). The lattice is defined by three non-coplanar vectors (**a**, **b**, **c**), specified by their magnitude (a,b,c) and relative orientation (α, β, γ) (Figure 2.1).

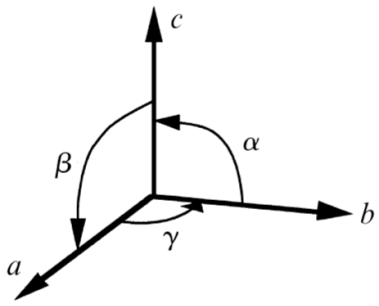

Figure 2.1: *The six scalar quantities describing the Bravais lattice in terms of magnitude (a,b,c) and relative orientation (α, β, γ) of the primitive vectors. From Rohrer (2001).*

A classification of crystal structure can then be based on the configuration of these three vectors with respect to each other. The main lattice structures are summarized in Table 2.1 and Figure 2.2, along with the number of independent constants in the elastic stiffness tensor.

Table 2.1: *Orientation and magnitude of primitive vectors in the different lattice systems and independent components in the elastic stiffness tensor (n), summarized from Rohrer (2001) and Babuska and Cara (1991).*

System	**Magnitude axes**	**Angles**	**n**
Triclinic	$a \neq b \neq c$	$\alpha \neq \beta \neq \gamma$	21^2
Monoclinic	$a \neq b \neq c$	$\alpha = \gamma = 90°$, $\beta \neq 90°$	13
Orthotropic	$a \neq b \neq c$	$\alpha = \beta = \gamma$	9
Tetragonal	$a = b \neq c$	$\alpha = \beta = \gamma$	5
Cubic	$a = b = c$	$\alpha = \beta = \gamma$	3

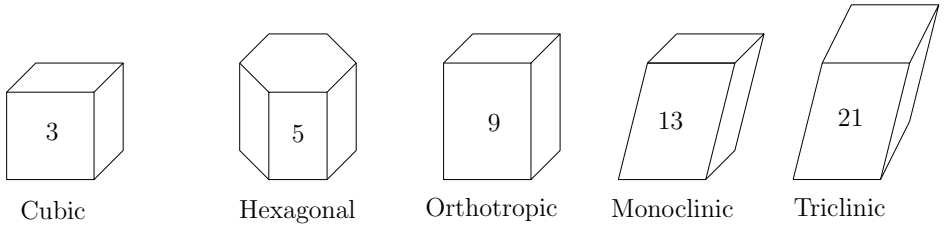

Figure 2.2: *Main types of symmetry in anisotropic media. The number inside each figure represents the number of independent elastic constants for the specific type of symmetry, summarized from Babuska and Cara (1991). The figure is modified from wwwf.imperial.ac.uk/earthscienceandengineering/ rocklibrary/symmetry.jpg, (Downloaded January 12, 2017).*

The anisotropic complexity depends on the number of independent components, so simplifications to complex lattice systems are often assumed. In this thesis it is assumed that lithospheric media can be described by hexagonal symmetry, which is a specific type of tetragonal symmetry ($a = b \neq c$, $\alpha = \beta = 90°, \gamma = 120°$) (Rohrer, 2001).

This simplification has been adopted as it provides an acceptable approximation to different types of anisotropy, such as crustal elongated cracks in isotropic media or olivine orientation in the mantle (Maupin and Park, 2007). The orthotropic symmetry of olivine can be approximated as hexagonal, making the assumption of hexagonal symmetry widely used in anisotropy studies of the mantle (Frederiksen and Bostock, 2000; Babuska and Cara, 1991). The program for synthetic modeling also assumes hexagonal symmetry. This

simplifies computations of anisotropic wave propagation, as the fast axis's orientation in a medium with hexagonal symmetry coincides with the symmetry axis of the stiffness tensor (Levin et al., 1999).

The symmetry axis of a hexagonal medium can of course be in any direction, but for simplicity many methods assume that it is either in the horizontal or the vertical plane (Maupin and Park, 2007). Two media with hexagonal symmetry are shown in Figure 2.3. These materials are sometimes also referred to as transversely isotropic. In seismology, the term transverse isotropy is often restricted to a symmetry axis in the vertical plane, but in general terms the symmetry axis of a transversely isotropic medium can be in any direction (Maupin and Park, 2007). The potential of separating anisotropic features from varying isotropic features is always a question of available resolution (Savage, 1999). Due to the resolution provided by low-frequent teleseismic events used in this thesis I am not able to distinguish between thin isotropic layering with alternating properties and intrinsic anisotropy, and therefore consistently refer to these materials as being radially or azimuthally anisotropic in this thesis. A material exhibiting radial anisotropy has properties which vary in the vertical plane, and when seismic velocity depends on the propagation direction within the horizontal plane the medium is characterized by azimuthal anisotropy (Babuska and Cara, 1991; Karato et al., 2015).

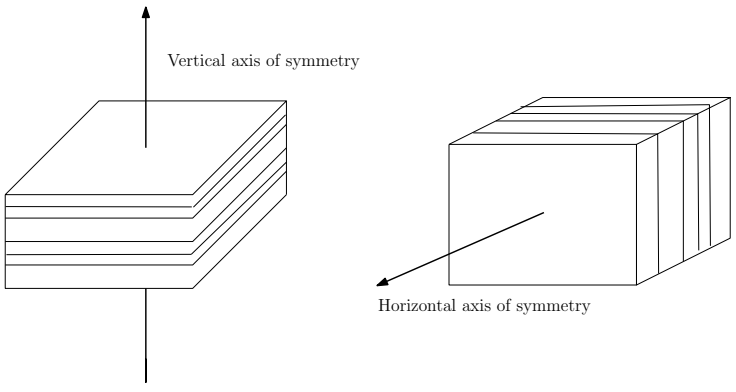

Figure 2.3: *Examples vertical and horizontal symmetry axes for thin isotropic layering, resulting in radial (left) and azimuthal (right) anisotropy.*

2.2 Anisotropy in the crust and upper mantle

Several mechanisms can produce anisotropy, such as alignment of crystals, grains, cracks and thin sedimentary beds within a layer (Fryer and Frazer, 1984; Savage, 1999). As the mechanisms causing anisotropy are quite different for the crust and the mantle, I discuss these features separately.

The upper mantle is dominated by dunite and periodite, two highly anisotropic rocks due to its content of olivine (Babuska and Cara, 1991). Olivine is a highly anisotropic mineral, where the magnitude anisotropy can be up to 25% (Christensen, 1984). When shear forces are applied to olivine above a certain temperature for a sufficiently long time, the minerals can form crystallographic alignment of their axes (Mainprice and Nicolas, 1989; Savage, 1999). The alignment causes the medium to have different seismic velocities depending on the direction of the incoming wave with respect to the orientation of the mineral's long axis (the a-axis). This origin of anisotropy is called lattice preferred orientation (LPO) (Fouch and Rondenay, 2006).

The magnitude of anisotropy in crystalline rocks is in the end a result of three distinct factors: the volume of various anisotropic minerals[3], the direction of active slip with respect to the orientation of axes in the minerals, and the degree of orientation (Babuska and Cara, 1991). The direction in which minerals align depends on the deformation mechanisms in a region (Levin et al., 1999). For the upper mantle, dislocation creep is generally assumed to align the fast axis in the direction of creep, as plastic flow induces a preferred mineral orientation in the direction of the flow by the force of neighboring grains (Mainprice and Nicolas, 1989; Christensen, 1984). LPO can be generated in the sub-lithospheric mantle by drag forces from the lithosphere if they are coupled, and anisotropy can therefore indicate the degree of coupling between the lithosphere and the asthenosphere (Levin et al., 1999). The degree of orientation depends on temperature and strain history, where higher temperatures and longer duration of strain enhances

[3]The mantle will for modeling purposes be assumed to be dominated by olivine, and contribution of other minerals will be discussed briefly in relation to the interpretation.

LPO (Savage, 1999).

When the temperature is below 1100 K (826.85°C), olivine minerals can no longer orient freely by the current stress field, and anisotropy must be explained by a different mechanism (Kosarian et al., 2011). The 1100 K thermal boundary occurs above the LAB, so a common explanation for anisotropy in the lithosphere is that it represents historical tectonic events, stored by a "frozen in" pattern of anisotropy (Savage, 1999). From regions of present compression it is found that the fast axis aligns sub-parallel with orogens, commonly attributed to flow related to transcurrent motion between the collisional plates (Levin et al., 1999; Park and Levin, 2002). We therefore expect "frozen in" anisotropy to follow geological surface trends.

The crust can also be anisotropic, but crustal anisotropy is more commonly caused by orientation of cracks or thin layering of materials with different velocities. Isotropic layers of alternating high and low velocities can cause an apparent anisotropic signal, where the slow direction is normal to the bedding, as illustrated in Figure 2.3 (Levin et al., 1999). In case of cracks or pore spaces, the slow direction will be normal to the average crack plane (Levin et al., 1999). Cracks and pores are assumed to reduce with increasing overburden pressure, making crack induced anisotropy less common at lower crustal depths. The same anisotropic signals can however arise at greater depths from melt filled lenses, as the presence of melt weakens the alignment of fast axes (Holtzman et al., 2003). The fast axis of melt filled lenses is found to be normal to the direction of highest shear (Holtzman et al., 2003). Melt lenses, crack orientation and compositional lamellae represent a type of anisotropy arising from geometrical patterns of impedance contrasts, referred to as shape preferred orientation (SPO) (Fouch and Rondenay, 2006).

As the anisotropic signals from SPO and LPO can yield different results in the same tectonic setting, it is important to consider what type of anisotropic material we are expecting (Fouch and Rondenay, 2006). The direction of greatest extension causes cracks to develop normal to the extensional direction, and thus a fast axis normal to the extension, while mantle fabric induced

by drag would have a fast axis in the direction of maximum extension, making interpretation ambiguous.

The complex nature of anisotropic signals requires anisotropy to be studied with imaging methods which allow for accurate interpretation, both in terms of location and magnitude. The presentation of one such method, the receiver function analysis, is therefore the topic of the next chapter.

Chapter 3

Receiver functions

The aim of this chapter is to introduce the concept of receiver functions (RFs) and discuss how they are affected by anisotropy. Although the RFs were generated ahead of this project, an in-depth understanding of the process is needed to fully understand the potential and limitations of the data. The RF analysis is based on seismic wave conversion, so energy conversions at solid-solid interfaces for isotropic and anisotropic media are discussed prior to the steps of generating RFs.

3.1 Teleseismic body waves

Receiver functions are normalized, converted seismic waves, measured at the surface (Langston, 1977). A converted seismic wave is a wave that has changed polarization after encountering a boundary. The converted wave thereby has a different travel time than the direct wave due to the velocity difference between the incident and converted waves, e.g., P-and S-waves (Fouch and Rondenay, 2006). The receiver function analysis utilizes differences in propagation velocity and particle motion of P-and S-waves to obtain information about discontinuities at depth. The particle motion of the P-wave is in the direction of wave propagation, while the particle motion of the

S-wave is orthogonal to direction of propagation, either in the vertical plane (SV) or horizontal plane (SH).

The receiver functions used in this thesis are generated from teleseismic events, defined as seismic events occurring at distances greater than 2000km from the seismic stations. This corresponds to 18° epicentral distance (Havskov and Ottemoller, 2010), but the limit for events considered teleseismic is often set to 30° in order to avoid triplications caused by the mantle transition zone (Stein and Wysession, 2009).

Teleseismic body waves are commonly used in receiver function analysis for two main reasons. First, P-waves propagate at a higher velocity than S-waves, separating the P-wave and its wave train of scattered and/or converted waves (called the P-coda) from the other phases at teleseismic distances (Rondenay, 2009). With a clearer separation of the phases it is easier to identify the conversions, which could improve the accuracy of the analysis. Secondly, the wavefront at teleseismic distances has small enough curvature that the front can be considered planar. For a planar wavefront, the angle of incidence is equal for the entire region beneath the recording site, which simplifies travel time calculations

3.2 Body wave conversions

The abrupt release of energy in an earthquake produces a seismic wave field. In the receiver function analysis, information is obtained from specific trajectories of the wave field from source to station, described by seismic rays. The ray path of a seismic wave can be estimated from Fermat's principle, where the path is approximated as a ray by the stationary travel time between two points (a local minimum or maximum) (Ĉervenŷ, 2001). Due to triplications, diffractions and conversions of the direct wave, the ray paths can become quite complex. Triplications are avoided by using teleseismic events, and diffractions are beyond the scope of this thesis. Converted waves form the basis of the receiver function analysis, and since energy conversion

depends highly on anisotropic properties on both sides of an interface, seismic wave conversion is the topic of the following subsections.

3.2.1 Seismic impedance

When a plane wave encounters a boundary between two isotropic and homogeneous media, the energy of the wave is partitioned between a reflected and a transmitted wave. Energy is conserved, which means that no more energy can be transmitted than was originally present. What might seem contrary to this is that the amplitude of the reflected/transmitted wave can be larger than the amplitude of the incoming wave. This can occur as the amplitude depends not only on energy initially present, but also on the material properties of the medium. As the waveform is affected by the material it has propagated through, the shape of the wave itself provides information about the subsurface.

A common way to describe material properties when discussing reflection and transmission is by acoustic impedance (I). The acoustic impedance is defined as the product of seismic velocity (V_P) and density (ρ) (Equation 3.1) (Kearey et al., 2013).

$$I = v\rho \tag{3.1}$$

A discussion about the acoustic impedance implies that only vertically incident pressure waves are considered, which is not the case in the receiver function analysis. In the industry the term elastic impedance is more commonly used, where both shear waves and angle of incidence is considered[1] (Connolly, 1999). This term is, however, rarely used in academia, so throughout this thesis I use the term seismic impedance, indicating a pulse which can arise from both P- and S-waves incident upon a solid-solid boundary.

[1]Equation for elastic impedance (EI) from Connolly (1999). K= Vs/Vp

$$EI = V_P(V_P^{tan^2\theta}V_S^{-8Ksin^2\theta}\rho^{1-4Ksin^2\theta})$$

Increases in seismic impedance with increasing depth is indicated by a red peak, and a reduction is indicated by a blue trough.

Energy partitioning of a seismic wave across an interface must occur in compliance with physical laws of traction and displacement. In case of a solid-solid interface, both traction and displacement must be continuous across the boundary (Stein and Wysession, 2009). This means that a wave propagating in the lower layer will cause an imbalance of traction and displacement across the boundary, thus generating a wave field in the upper layer (Lay and Wallace, 1995). For a solid-solid boundary, the transmitted and reflected P-waves are not parallel across the interface, resulting in non-continuous shear stresses and generation of shear waves in order to fulfill boundary conditions (Figure 3.1).

Many methods assume planar and horizontal interfaces and layers with isotropic properties, but due to a highly complex Earth this is often not the case. The following section therefore describes how energy partitioning can be estimated for isotropic and anisotropic layers, both for horizontal and dipping interfaces.

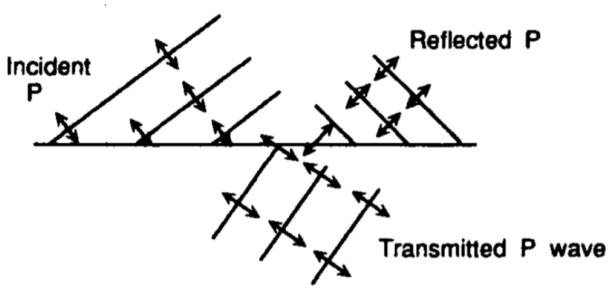

Figure 3.1: *Particle motion of incident, reflected, and transmitted P-waves. The shear stresses in the two layers are not continuous, thus requiring the generation of shear waves. From Lay and Wallace (1995).*

3.2.2 Isotropic boundaries

A direct P-wave upon a boundary between two solid isotropic media will split into reflected and transmitted P- and S-waves in order to fulfill the boundary

conditions. When the boundary is horizontal, the S-wave will have particle motion perpendicular to the direction of wave propagation within a vertical plane. If the boundary is dipping, the generated S-waves can have particle motion in the horizontal plane as well as a vertical plane, but as the velocities of SV and SH waves are equal in isotropic media, the rays coincide (Lay and Wallace, 1995).

The angle of reflection and transmission for isotropic media separated by a horizontal boundary can be described by Snell's law, following a constant ray parameter p (Equation 3.2).

$$\frac{\sin(\theta_1)}{v_1} = \frac{\sin(\theta_2)}{v_2} \tag{3.2}$$

The ray parameter $p = \sin(\theta)/v$ can be seen as the horizontal slowness of the ray. θ is the angle of incidence, and v is the P- or S-wave velocity in the medium.

The amount of energy reflected and transmitted is calculated from reflection and transmission coefficients. These depends on material properties on both sides of the interface, and the incidence angle of the ray (Lay and Wallace, 1995). By using teleseismic waves, which are always sub-critical conversions, all waves in and out of the boundary are in phase, thus avoiding the problem of phase shift between different waves (see Lay and Wallace (1995), Ch.3). The reflection and transmission coefficients for a solid-solid interface are summarized in Equation 3.3, where α and β correspond to P-wave and S-wave velocities, ρ is the material's density, and the vertical slowness η is defined as $cosi/\alpha$ (other coefficients explained on the next page).

$$\begin{aligned}
R_{PP} =& [(b\eta_{\alpha 1} - c\eta_{\alpha 2})F - (a + d\eta_{\alpha 1}\eta_{\beta 2}Hp^2)]/D \\
R_{PS} =& -[2\eta_{\alpha 1}(ab + cd\eta_{\alpha 2}\eta_{\beta 2})p(\alpha_1/\beta_1)]/D \\
T_{PP} =& [2\rho_1\eta_{\alpha_1}F(\alpha_1/\alpha_2)]/D \\
T_{PS} =& [2\rho_1\eta_{\alpha_1}Hp(\alpha_1/\beta_2)]/D
\end{aligned} \tag{3.3}$$

$$
\begin{aligned}
a =& \rho_2(1-2\beta_2^2p^2) - \rho_1(1-2\beta_1^2p^2) & E =& b\eta_{\alpha_1} + c\eta_{\alpha_2} \\
b =& \rho_2(1-2\beta_2^2p^2) - 2\rho_1\beta_1^2p^2 & F =& b\eta_{\beta_1} + c\eta_{\beta_2} \\
c =& \rho_1(1-2\beta_1^2p^2) + 2\rho_2\beta_2^2p^2 & G =& a - d\eta_{\alpha_1}\eta_{\beta_2} \\
d =& 2(\rho_2\beta_2^2 - \rho_1\beta_1^2) & H =& a - d\eta_{\alpha_2}\eta_{\beta_1} \\
& & D =& EF + GHp^2
\end{aligned}
$$

The amplitude ratio as a function of incidence angle between reflected and transmitted waves is shown in Figure 3.2, for a P-wave incident upon a solid-solid interface.

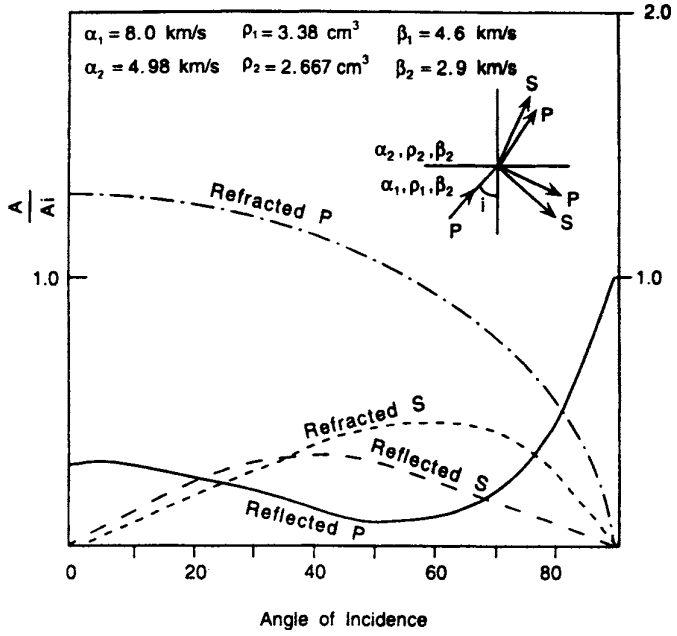

Figure 3.2: *Variations in amplitude ratio between incident and reflected/refracted wave for different incidence angles. There are no critical angles in this case. From Lay and Wallace (1995).*

The angle of incidence is measured at the station with respect to the vertical, yet reflection and transmission occur in relation to the reference frame of the

system (see Figure 3.3). For a dipping interface, this means that Snell's law applies to a rotated coordinate system. If the dip angle ψ of the boundary is known, the incidence angle with respect to the interface can be estimated from Equation 3.4, which is a geometrical correction of Equation 3.2, where ϵ is the measured angle of incidence (Figure 3.3). The coefficients for reflection and transmission for horizontal layering then applies to the dipping layer in the corrected reference frame (Langston, 1977).

$$p' = \frac{\sin(\theta_1')}{v_1} = \frac{\sin(\epsilon - \psi)}{v_1} \tag{3.4}$$

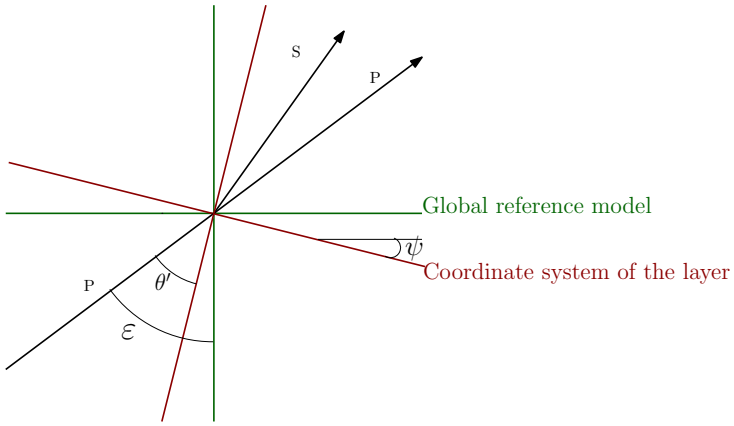

Figure 3.3: *A ray incident upon a dipping interface will have the angle of incidence measured according to the global reference (ϵ) , while the transmission occurs according to angle of incidence normal to the layer θ'.*

Reflection of SH-waves must also be considered when the interface is dipping. For SH polarization parallel to the interface, the equations for reflection and transmission of an incident SH-wave are fairly simple (Lay and Wallace, 1995):

$$\begin{aligned} T_{SH} &= \frac{2\mu_1\eta_{\beta_1}}{\mu_1\eta_{\beta_1} + \mu_2\eta_{\beta_2}}, \\ R_{SH} &= \frac{\mu_1\eta_{\beta_1} - \mu_2\eta_{\beta_2}}{\mu_1\eta_{\beta_1} + \mu_2\eta_{\beta_2}}. \end{aligned} \tag{3.5}$$

3.2.3 Anisotropic boundaries

Three independent body waves are generated in anisotropic media. All planes of particle motion are orthogonal to each other, but the velocity at which they propagate differ (Maupin and Park, 2007). The waves are usually named 'quasi-waves'[2], to separate them from the waves generated in isotropic media. The main distinguishable feature between these quasi-waves and the body waves generated at isotropic boundaries is that the direction of propagation for quasi-waves is generally not perpendicular to the wavefront (Lay and Wallace, 1995).

For anisotropic media, Snell's law can still be used to calculate the angle at which the waves are reflected/transmitted, the main challenge is to calculate the reflection and transmission coefficients (Lay and Wallace, 1995). Since velocities of the waves depend on the trajectory of the wave through the media, the amount of energy being reflected and transmitted across an anisotropic interface depends both on the direction of the incoming wave and the type of anisotropy in question (Fryer and Frazer, 1984; Lay and Wallace, 1995). As hexagonal anisotropy is assumed in this thesis, this section only discusses reflection and transmission in an anisotropic medium with hexagonal symmetry .

Fryer and Frazer (1984) came up with a recursive scheme that computes the structural response through reflection and transmission coefficients in strongly anisotropic media. Development of the equations for energy partitioning across anisotropic boundaries is beyond the scope of this thesis, so only the results are presented here. The reader is referred to the original article for the full development of equations.

The coefficients are obtained by evaluating the eigenvalues E of the wave propagator Q for each layer in question for quasi P- and S-waves. The eigenvalues and eigenvectors correspond to the independent portions of the up-going and down-going anisotropic wave field. qP is the quasi P-wave, and

[2]For weak anisotropy, where the direction of particle motion follows approximately that of an isotropic medium.

qS1 qS2 are the two quasi S-waves, z_1 is some reference depth, and U, D are superscripts indicating whether the wave is up-going (U) or down-going (D). This results in reflection and transmission coefficients for up-going and down-going incident waves of all wave types :

$$R_D = \begin{pmatrix} R^D_{PP} & R^D_{P1} & R^D_{P2} \\ R^D_{1P} & R^D_{11} & R^D_{12} \\ R^D_{2P} & R^D_{21} & R^D_{22} \end{pmatrix} \tag{3.6}$$

The first term with subscripts of the matrix elements correspond to the incident wave type, and the second term to the wave type after the wave encountered the interface (1 is qS1, 2 is qS2). R^D_{P2} is thereby the amplitude of a reflected qS2 wave resulting from a down-going qP wave. The same calculations can also be used to compute a reflected up-going wave (R_U), a down-going transmitted wave (T_D) and an up-going transmitted wave (T_U). These are gathered in a full reflection matrix R:

$$R = \begin{pmatrix} T_U & R_D \\ R_U & T_D \end{pmatrix} = \begin{pmatrix} Q^{-1}_{11} & -Q^{-1}_{11}Q_{12} \\ Q_{21}Q^{-1}_{11} & Q_{22} - Q_{21}Q^{-1}_{11}Q_{12} \end{pmatrix} \tag{3.7}$$

where Q can be regarded as the wave propagator, consisting of the eigenvalues E defining the orthogonal planes in which the seismic waves propagate:

$$Q(z, z_1) = \begin{pmatrix} E_U & 0 \\ 0 & E_D \end{pmatrix} \tag{3.8}$$

$$E_U = diag\left\{e^{i\omega(z-z_1)}qP^U, e^{i\omega(z-z_1)}qS1^U, e^{i\omega(z-z_1)}qS2^U\right\} \tag{3.9}$$

$$E_D = diag\left\{e^{i\omega(z-z_1)}qP^D, e^{i\omega(z-z_1)}qS1^D, e^{i\omega(z-z_1)}qS2^D\right\} \tag{3.10}$$

and *diag* denotes the eigenvalues along the diagonal of the system matrix.

When the boundary between two anisotropic materials is dipping, the angle at which they are reflected/transmitted must again be corrected for, as in the isotropic case. The reflection and transmission coefficients are not affected by dip, allowing us to use the same equations for dipping anisotropic models as for horizontal anisotropic models (Lay and Wallace, 1995).

3.3 From seismic wave to receiver function

The receiver function analysis utilizes either S-waves converted to P-waves (Sp), or P-waves converted to S-waves (Ps). Receiver functions based on Sp waves are called SRFs, while receiver functions based on Ps are called PRFs (Selway et al., 2015). Both methods hold desirable attributes for analysis of the subsurface. At teleseismic distances the P-wave coda is less likely to contain other phases, thus the P-wave coda is comprised only of the scattered P-waves, which are the desired conversions for the analysis (Rondenay, 2009). The Ps conversion can be masked by crustal reverberations when mapping mantle discontinuities. For mantle imaging at certain depths it can then be beneficial to use Sp conversions, as the Sp arrives prior to the S-wave coda, which is separated from the P-wave coda at teleseismic distances (Fischer et al., 2010). Only PRFs are considered in this thesis, and the abbreviation RFs is therefore used for receiver functions based on Ps conversions.

Development of the following subsections is in large part based on the work of Rondenay (2009) and references therein.

3.3.1 Coordinate rotation

Three component seismograms record energy arriving in the North-South direction (N), East-West direction (E) and vertical (Z). Although useful for location purposes, the energy from both P- and S-waves will in most cases be partly contained on all components. It is desirable to rotate the coordinate system to separate the recorded energy, ideally so that the P-wave is

constrained to one component, and the S-wave(s) constrained to the other two components.

The separation is performed by a rotation of each component around the vertical axis using the backazimuth of the incoming wave, where the backazimuth is the azimuth from the north to the source when viewed from the station (Langston, 1979). The newly rotated components are called the radial (R), transverse (T) and vertical (Z, unchanged) component. The radial component is in the direction of the incoming wave field, and the transverse component is normal to the radial component (Figure 3.4a) (Rondenay, 2009). With this rotation, and a vertical incidence of a P-wave, the P-wave is recorded only on the vertical component (Z) and the Ps conversion is captured on the radial component. However, as the angle of incidence for teleseismic P-waves at the surface normally vary between 10° and 30°, both the incident (non-converted P-wave) and the Ps wave fields will be recorded on both the radial and the transverse component.

The converted waves are better constrained to one component when the wave fields are rotated in the R-Z plane (around the transverse component) based on the polarization of the P-wave. The new coordinate system is then defined from the direction of particle motion of the P-wave (L) and the direction perpendicular to it and the z-axis (Q) (Figure 3.4b)[3]. With this rotation the direct P-wave should be restricted to the L component, and the conversion should be restricted to the Q component, provided that assumptions about planar, horizontal, and isotropic discontinuities are valid.

[3]Throughout this thesis, the components referred to as "radial" and "transverse" components are in fact the Q and T components (respectively).

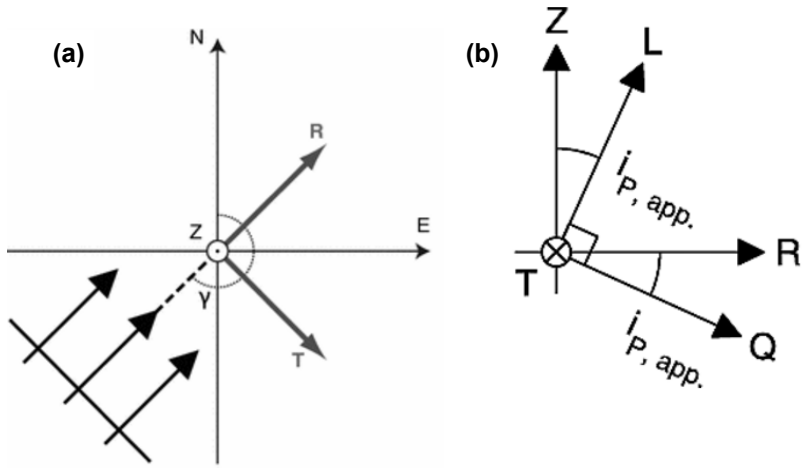

Figure 3.4: *(a) Coordinate rotation from N-E-Z components into the radial (R), transverse (T) and vertical (Z) component, viewed in the horizontal plane. Adapted from Rondenay (2009). (b) Rotation of the R-T-Z coordinate system into the L-Q-T system using the approximate incidence angle. Adapted from Svenningsen and Jacobsen (2004).*

3.3.2 Deconvolution

The seismic signal *d(t)* recorded at a station does not only contain the information we seek about the subsurface, as it is a convolution of several time signals. In particular, *d(t)* is a combination of the source signature *s(t)*, the Earth's impulse response *e(t)*, and the instrumental response from the seismic recorder *i(t)* (Langston, 1979):

$$d(t) = s(t) * e(t) * i(t), \tag{3.11}$$

where $*$ denotes the convolution operator.

Due to the difference in particle motion of body waves, the Earth does not affect the waveform of P- and S-waves in the same manner, and the recorded signal will be different for each component:

$$d_L(t) = s_L(t) * e_L(t) * i_L(t), \tag{3.12}$$

$$d_Q(t) = s_Q(t) * e_Q(t) * i_Q(t), \tag{3.13}$$

$$d_T(t) = s_T(t) * e_T(t) * i_T(t). \tag{3.14}$$

The source time function and the instrumental response are equal for all three components. As the interesting part of the signal for a RF study is the Earth's impulse response, we need to remove the source signature and the instrumental response from the recording. Due to the differences in particle motion, the shape of the P-wave is less affected by medium properties than S-waves. The L component can be therefore be used as an estimate of the combined source signature and instrumental response. Assuming then that the effect of travel path can be neglected for the P-wave, Equation 3.12 can be simplified to:

$$d_L(t) \cong s_L(t) * i_L(t) \tag{3.15}$$

By rearranging Equation (3.15), the Earth's impulse response can be approximated by a division in the frequency domain (marked by capital letters):

$$E_Q(\omega) = \frac{D_Q(\omega)}{S(\omega)I(\omega)} \cong \frac{D_Q(\omega)}{D_L(\omega)} \tag{3.16}$$

The process of deconvolving the L component from the two other components is called source normalization (Langston, 1979). After source normalization, E_Q is transformed back to the time domain through an inverse Fourier transform, and the resulting e_Q represents the Earth's impulse response.

Although this deconvolution provides a simple solution to a complex problem, there are some considerations that must be made when using this approach. Random noise will influence the recording, and the shape of the vertical component is to some extent affected by the Earth, causing D_L to be a less accurate estimate of the source time function (Langston, 1979). Another

issue is that the deconvolution is performed in the frequency domain, and various frequencies could be zero (or close to zero) in the vertical component, causing an unstable solution (Rondenay, 2009). A common approach to handle this problem is a normalization method called water-level deconvolution, where the frequency band of the L component is altered to be above a set water-level for all frequencies.

3.3.3 Time correction to align traces for stacking

It is beneficial to enhance the Ps conversion which is occurring within the P-wave coda by stacking traces from different sources. To achieve constructive stacking the traces must be corrected for differences in travel time. Rays arriving from sources at larger epicentral distances encounter the discontinuities beneath the station at an angle closer to the vertical than rays from nearby sources (Figure 3.5). The waveforms therefore have seismograms stretched out according to the additional travel time within each layer, resulting in a time difference between the direct wave (P) and the conversion (Ps) which depends on epicentral distance.

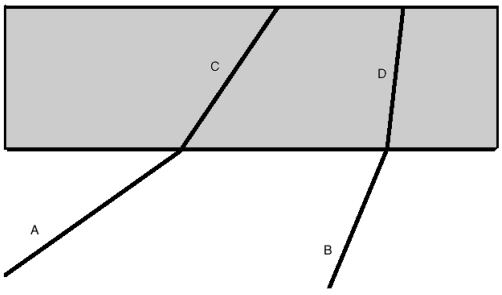

Figure 3.5: *Illustration of how differences in incidence angle lead to a stretching of seismograms. Two rays (A and B) arriving at an interface at depth with different angles. Segment C is longer than segment D, due to the angle of incidence upon the boundary.*

If we assume there are good estimates of the velocities above the discontinuity (α and β), and that these velocities are laterally continuous across the region sampled by both incident and converted waves recorded by a station, then the differential time between incident and converted wave can be expressed by (Rondenay, 2009):

$$\begin{aligned} T_{Ps}(p,h) &= \int_{z=0}^{z=h} \sqrt{\frac{1}{\beta^2(z)} - p^2} - \sqrt{\frac{1}{\alpha^2(z)} - p^2}\, dz \\ &= \int_{z=0}^{z=h} q(\beta)(p,z) - q(\alpha)(p,z)\, dz \end{aligned} \tag{3.17}$$

where p is the ray parameter, h is the depth of conversion, and q_α, q_β are the vertical slownesses.

The move-out correction can be estimated by subtracting the time delay of any ray parameter (p_0) with epicentral distance in the range 30-90° from the station's travel time (Equation 3.18).

$$\Delta T_{Ps}(p,h) = T_{Ps}(p,h) - T_{Ps}(p_0,h) \tag{3.18}$$

The move-out can then be calculated in the frequency domain using the inverse Fourier transform (IFT):

$$R(t) = R(h(t)) = IFT[\sum_{k=1}^{N} \hat{r}_k(\omega) e^{i\omega \Delta T_{Ps}(p_k, h(t))}] \tag{3.19}$$

This correction makes it possible to stretch or compress each trace, depending on whether the epicentral distance of the source is greater or smaller than the reference ray parameter (Rondenay, 2009).

3.4 Effect of anisotropy on receiver functions

From the previous discussion about seismic impedance it is seen that the velocity/density contrast across an interface affects the amplitude of the pulse recorded at the surface. For an interface with at least one anisotropic layer, this velocity/density contrast also depends on the backazimuth. As the particle motion in the horizontal plane is far more affected by anisotropy than the particle motion in the vertical plane, we primarily use the transverse component to investigate changes in seismic impedance with backazimuth, (Lay and Wallace, 1995). Changes in polarity of seismic impedance are here referred to as polarity reversals with backazimuth. If we have sufficient knowledge about how polarity reversals appear on the transverse component for various anisotropic scenarios, the transverse component can be used to map and characterize anisotropic properties of the subsurface (Frederiksen and Bostock, 2000).

It is important to note that polarity reversals also occur when the layer in question is dipping. This is one of the challenges for interpretation, that both dip and anisotropy produce differences in amplitude and travel time of the impulse response as a function of backazimuth (Frederiksen and Bostock, 2000). When the goal is to identify anisotropic features of a layer, one should first aim to determine whether the layer in question has a dip that contributes to the signal variation before continuing the analysis. The presence of dipping layers can be estimated based on polarity reversals in the direct P-wave, which according to Frederiksen and Bostock (2000) only occurs when the interface is dipping. Whenever available, RF data should be supplemented with a priori tectonic information about the study area.

It is also beneficial to know what type of anisotropy we are looking for when aiming to interpret the processes causing anisotropy. This is particularly important if we wish to determine whether anisotropy arises from layer composition, or if it is a result of current or historical tectonic processes.

Chapter 4

Imaging anisotropy

This chapter describes some of the common imaging methods used to study anisotropy. Although only receiver functions are used in this thesis, an introduction to other methods is required as several previously published results on the subject arise from these other imaging techniques. I therefore address the benefits and limitations to shear wave splitting and surface wave studies[1], before moving on to receiver functions. I discuss two tools that can be used to characterize anisotropy with RFs: forward modeling of synthetic RFs and computation of harmonics along the backazimuthal range.

4.1 Shear wave splitting and surface waves

At lithospheric scale, anisotropy has traditionally been studied with travel time variations in surface wave data, and shear wave splitting of the SKS/ SKKS phase (Fouch and Rondenay, 2006). This section provides a brief introduction to these imaging methods, focusing primarily on advantages and limitations of the methods.

[1]The use of Pn velocity variations with azimuth, which was among the first technique used to map anisotropy in oceanic lithosphere (Maupin and Park, 2007; Savage, 1999), has not been included in this chapter. This is because no results on lithospheric Pn-wave anisotropy are discussed in this thesis.

4.1.1 Shear wave splitting

In an anisotropic medium, the propagational velocity of a seismic wave depends on direction through the medium, as described in Chapter 2. For a shear wave, this results in different propagation velocities of the two phases (SH and SV), giving rise to a phenomenon referred to as shear wave birefringence, or shear wave splitting (Park and Levin, 2002). The fast axis is determined based on the polarization of the fastest shear wave (Fouch and Rondenay, 2006). The magnitude of anisotropy will be reflected in the travel time variations between the two phases, thus making shear wave splitting a powerful tool for detection of anisotropy within the mantle (Gaherty, 2004). A challenge with this approach of magnitude determination is that the splitting time is a signal integrated over the whole anisotropic region. It is therefore difficult to determine whether the anisotropic signal arise from a large weakly anisotropic region, or a thin strongly anisotropic region (Kosarian et al., 2011; Levin et al., 1999). Another challenge is that the SKS/ SKKS phase has a near vertical incidence, making it ideal for location of azimuthal anisotropy, but less sensitive to radial anisotropy. This makes it challenging to determine the precise location of anisotropic materials (Fouch and Rondenay, 2006). In conclusion, the shear wave splitting method provides good lateral resolution, but rather poor depth constraint.

4.1.2 Surface wave dispersion

Surface wave studies evaluate travel time variations of Love and Rayleigh waves, and holds the potential of detecting both radial and azimuthal anisotropy (Fouch and Rondenay, 2006). The Love-wave consists of SH-waves, while the Rayleigh wave is a juxtaposition of SV- and P-waves at the surface (Babuska and Cara, 1991). One particularly useful feature with surface waves is their dispersive nature, meaning that the phase velocity is a function of frequency or wavelength (Romanowicz, 2011). By matching observed dispersion curves to theoretical curves for a layered Earth model, the dispersion curves can be

inverted to find local variations of elastic parameters with depth, allowing for generation of 3D models of anisotropy across large regions (Romanowicz, 2011).

In many regions there have been noted differences between dispersion curves for Rayleigh- and Love-waves, which cannot be reproduced by purely isotropic models (Ekström et al., 1997). This difference in dispersion curves is what is referred to as a Love/Rayleigh discrepancy, and is commonly used in surface wave studies to characterize radial anisotropy (Babuska and Cara, 1991; Gaherty, 2004). Azimuthal anisotropy is evaluated based on travel time variations of the Rayleigh wave in different directions (Fouch and Rondenay, 2006). The main challenge with the surface wave method for interpretation of sharp anisotropic boundaries is that the discrepancies can arise from either anisotropic material or laterally heterogeneous isotropic materials (Fouch and Rondenay, 2006).

Both these methods provide the means of detecting anisotropy, but not the exact location or magnitude of the anisotropic material. As the goal of this thesis is to map anisotropic features of a boundary at specific depths, preferably ruling out the contribution of heterogeneties, neither of these approaches are ideal. Receiver functions provide the highest vertical resolution of the three methods (Fouch and Rondenay, 2006). When used for harmonic decomposition RFs can also provide further constraint on the contribution from 3-D complexities to the waveform (Bianchi et al., 2010).

4.2 Receiver function imaging

Receiver functions represent impulses corresponding to discontinuities below a station, and these impulses can in the simplest manner provide information about the interfaces' depth and velocity contrast of the layers. The depth can be estimated from the difference in arrival time between the direct P and the Ps conversion through a simple relation between S-wave velocity and time difference, given a well constrained background velocity model (Selway

et al., 2015). The magnitude of property variations across an interface can be estimated from the amplitude ratio of P to Ps. As seen in Chapter 3.2, the impulse of a wave (direct and converted) upon an interface can arise from a change in velocity/density, anisotropy, or a combination of the two.

RFs can also be used for more refined studies of the subsurface, and in the next two sub-sections I discuss two highly useful ways to utilize information contained in RFs to investigate anisotropy. I address how RFs can be used for forward modeling based on synthetic data, and how energy along each time step can be decomposed into harmonics along the backazimuths.

4.2.1 Forward modeling

As RFs from radial and transverse components contain different information, the components can be combined to create a model of the subsurface. RF studies most commonly utilize the radial component, to estimate the depth of each interface through a time-depth conversion. Impulses on the transverse component arise from areas of complex 3D-heterogeneties[2], anisotropy, or dip, and therefore provide additional information. Energy on the transverse component can be used for a thorough investigation of anisotropy and dip at a station with good backazimuthal coverage of RFs, through an examination of how the impulse response varies with backazimuth (Frederiksen and Bostock, 2000). Figure 4.1 shows an example of a synthetic section from Frederiksen and Bostock (2000), where amplitude variations is indicated as black and white signals. The most complex signals are found in the transverse (SH) component.

As both dip and anisotropy lead to variations in amplitude and travel time on the transverse component, it is important to be aware that the energy can arise from either of the two when making an interpretation. Luckily, the pattern of amplitude reversals provides additional clues as to whether the

[2]Assessment of complex 3-D heterogeneties will not be included in the forward modeling process as the software does not provide an option of adding this, but it will be considered when discussing harmonic decomposition.

energy is caused by anisotropy or dip (Frederiksen and Bostock, 2000).

The process of forward modeling RFs is based on trial-and error iterations. A synthetic model is created, and updated until its resulting RFs fit the real data. The forward modeling in this thesis is based on synthetic sections of RFs from a program called RAYSUM, which will be elaborated on in the method chapter. As the fast axis and dip is known for the forward modeling process, we aim to obtain the same result as those seen in the real data to gain information about the layer properties. An important note here is that several scenarios can produce similar signals, and the goal is therefore to find the simplest possible model that reproduces the real data.

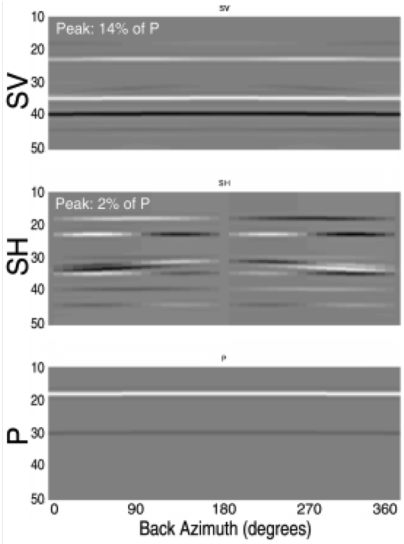

Figure 4.1: *Example of synthetic section generated with RAYSUM, for a ray parameter of 0.05 s/km incident upon a wedge model with a horizontal fast axis along strike. From Frederiksen and Bostock (2000).*

4.2.2 Harmonic decomposition

Harmonic decomposition is a process in which we map the amount of energy following simple harmonics along the backazimuthal range. In the harmonic decomposition process, the radial and the transverse component are combined to obtain information about isotropic and anisotropic features of the

subsurface (Bianchi et al., 2010). This is useful as the Q-component (radial) is most affected by isotropic features, and the T-component (transverse) contains Ps-conversions.

At each time step, amplitudes are extracted from the radial and transverse component. These amplitudes are converted to the frequency domain, though a fast fourier transform. Harmonic orders are extracted from backazimuthal variations in the amplitude spectra, and radial and transverse backazimuthal harmonics are summed. The components are summed in two different ways to separate the signal contribution from anisotropy and 3-D heterogeneties. A sum with a positive phase shift (Q+iT) is referred to as the "modeled" harmonics, and correspond to signals arising from anisotropy or dipping boundaries. A negative phase shift the components (Q-iT) is referred to as the "unmodeled" harmonics, and energy here arise from 3-D heterogeneties, such as scattering points. The layered earth structure is often assumed in studies of the lithosphere for simplicity, but strong signal on the "unmodeled" harmonics point towards a deviation from simple layering (Babuska and Cara, 1991; Bianchi et al., 2010). The "unmodeled" harmonics can thereby be used to check, to first order, whether an assumption about planar structures seems valid.

The way these harmonics are constructed is based on the periodicity of the modeled and unmodeled harmonics, arising from the assumption that amplitudes of RFs along a specific time can be expressed as a scaled sum of sines and cosines of harmonic degree k and backazimuth ϕ (Bianchi et al., 2010). The harmonic degree k can be seen as the number of full periods of sines/cosines along the backazimuthal range.

In this method, only the first three harmonics are considered (k=0,1,2) as they are the only harmonics that have been linked to physical features (Bianchi et al., 2010). Figure 4.2 shows an example of a harmonic decomposition of receiver functions for the first three harmonic orders. k=0 is called the constant backazimuth harmonic. For k=0, the energy on the transverse component disappears and the signal can be seen as the stack

of Q-components across all backazimuths. By eliminating the effect from the transverse component, only the isotropic part of the signal is represented, and k=0 is therefore referred to as the constant backazimuthal harmonic. k=1 and k=2 represent energy arising from a deviation to a planar, horizontal, isotropic model. On the modeled harmonics, k=1 represents the 2π polarity periodicity of the converted wave, which is likely to be produced by dipping layers or a plunging fast axis at depth (Bianchi et al., 2010). k=2 represents the π periodicity of polarity reversals for the converted wave, produced by anisotropy with a horizontal symmetry axis (Bianchi et al., 2010).

The preferred orientation of the fast axis can be evaluated from an assessment of the cos ϕ and sin ϕ contribution for k=1 on the modeled harmonics. Energy on cos ϕ is mapped on the NS axis, while energy on sin ϕ is mapped on the EW axis.

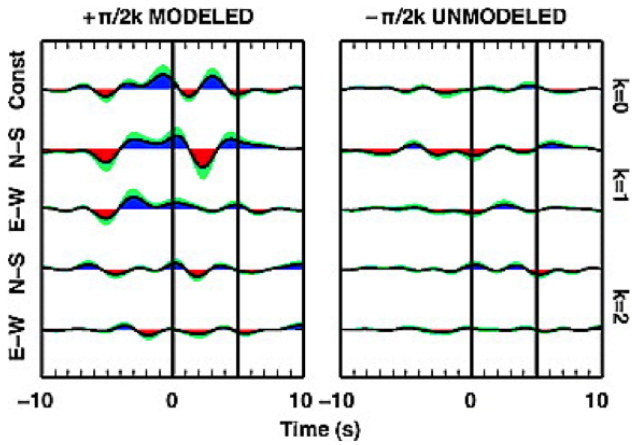

Figure 4.2: *Example of harmonic decomposition of RFs from Bianchi et al. (2010). See text for explanations of the different harmonics and components.*

Chapter 5

Study area

The main focus of this thesis is on the MLD beneath eastern North America. One of the interesting reasons to study the MLD in eastern North America is that the area is not cratonic like other locations where the MLD have been mapped (Fischer et al., 2010), but is a result of several collisional and extensional events extending back to Archean times. Chapter 5.1 discusses the main tectonic events that formed eastern North America, focusing on regional trends that could cause a "frozen in" anisotropic signal. Chapter 5.2 summarizes results from previous studies within the study area, focusing on large scale layering, velocities and anisotropy.

5.1 Geological and tectonic accretion of eastern North America

Due to the continent's rich tectonic history, only the main features of tectonic evolution in eastern North America will be discussed:

1. Archean crust - formation of the Superior province
2. The Grenville orogeny
3. The Appalachian chain formation

5.1.1 Archean - Superior

The Precambrian shield of North America was assembled around 1.7 Ga through a series of orogens (Hoffman, 1989). The shield consists of seven former micro-continents of early to mid-Archean age: The Superior, Wyoming, Slave, Nain, Hearne, Rae and Burwell (Figure 5.1). These micro-continents are usually referred to as Archean provinces. The assembly was a result of collisions between continents and arcs, and the provinces are therefore distinguished from each other based on signs of deformed margins, such as sedimentary prisms, and foreland thrust-fold belts (Hoffman, 1989).

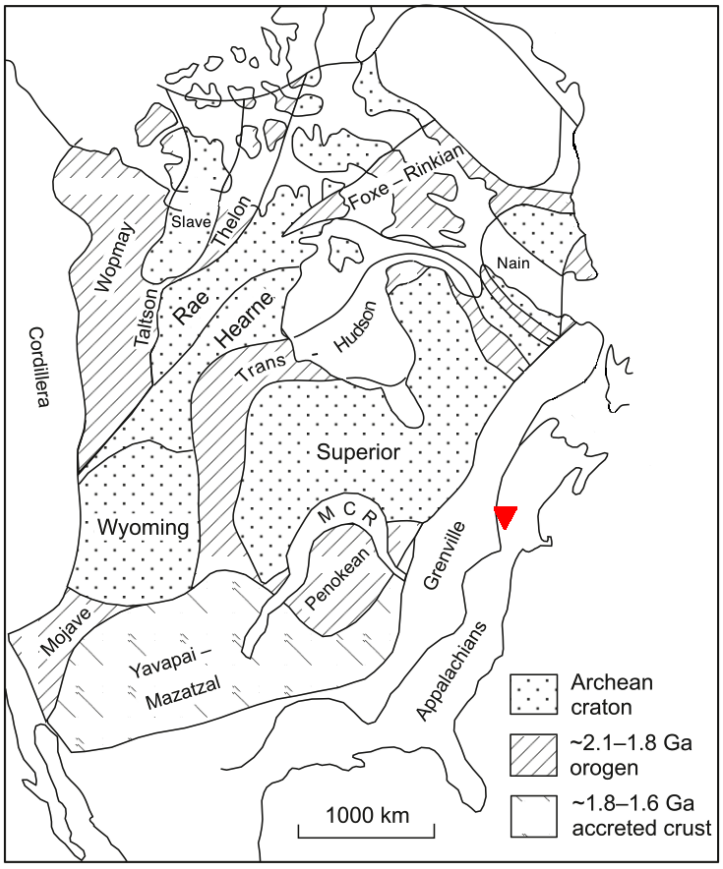

Figure 5.1: *The main provinces and orogens of North America, modified after Hoffman (1988) and Buchan et al. (2009). Red inverted triangle denotes the main study area in this thesis.*

Out of the seven provinces, the Superior province is the most relevant province study due to its proximity to the study area. The Superior province formed around 2.8-2.7 Ga (Hoffman, 1989), and still makes up 1.6 million km^2 of the exposed surface area in North America. The rocks in the Superior province are similar to those formed in younger subduction zones, indicating that Archean crust can have been formed by a succession of the Archean equivalent of island arc subductions. The differences between rocks in the Superior and younger subduction rocks can be attributed to the higher mantle temperatures in the Archean (Griffin et al., 2003). The Superior province contains sub-parallel belts of contrasting lithology, age, or metamorphic grade, which are all trending N/NE.

5.1.2 Proterozoic - Grenville

Later in the Precambrian, the Grenville orogen formed through collision between Laurentia and another continent, most likely Amazonia (Hynes and Rivers, 2010). The collision initiated around 1.1 Ga, and lasted over a million years. It is therefore called a large, hot, long-duration orogen (Hynes and Rivers, 2010). The orogen has an exposed width of 300-400km, but as samples of rocks from the orogen are found within the Appalachian chain, the extent is believed to have been much greater in earlier times (Hynes and Rivers, 2010). The collision between the two continents resulted in thrust faulting, with thrusting towards the inlands of Laurentia (NW), dipping towards SE. The age of thrusting folds gets progressively younger towards the south-eastern part of the orogen.

5.1.3 Paleozoic - Appalachian

The Appalachian chain has been formed through successive rifting and collisional events and terminated with the formation of Pangea (Rast, 1989). The Paleozoic history of eastern North America was initiated by the opening of the Iapetus ocean, which for the northern region of Appalachian dates back

to 590-550 Ma (Van Staal et al., 1998). Opening of the Iapetus ocean separated Laurentia from Amazonia and resulted in formation of oceanic basins (Van Staal et al., 1998). Island arcs formed within these basins and moved towards Laurentia, eventually leading to a collision. The collision of these island arcs with Laurentia is referred to as the Taconic arc collision and dates back to the end of the Ordovician (Bradley, 1989). The generally accepted tectonic setting is a collision between a passive margin facing east and an island arc, over a subduction zone dipping east (Bradley, 1983).

The next collisional event occurred in Devonian between Laurentia and a micro continent called Avalonia, a precambrian continental basement (Bradley, 1983). This event is referred to as the Acadian orogeny. The study area is situated on the border between a coastal volcanic arc and the Merrimack-Fredericton Trough (Figure 5.2), which is believed to be the remains of an oceanic plate which subducted on both sides during the Acadian orogeny (Figure 5.3) (Bradley, 1983).

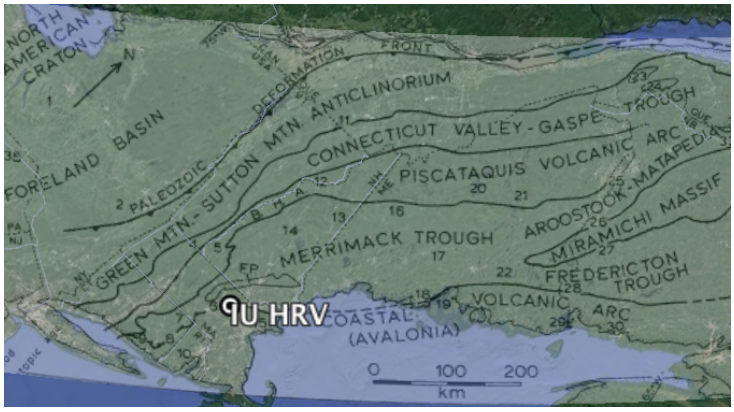

Figure 5.2: *Map of eastern North America overlaid by zones of large scale structures in late Ordovician to early Devonian from Bradley (1983). The study area is located on the border between the coastal volcanic arc and the Merrimack trough (Massachusetts, USA).*

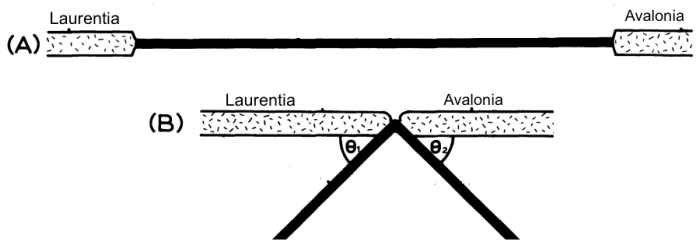

Figure 5.3: *Illustration of the Merrimack trough formation by double sided subduction of an oceanic plate. The study area is situated on the boarder between the Merrimack trough and the Avalonia plate. Modified from Bradley (1983).*

The final, and largest collisional event that formed the Appalachian chain was the collision between Laurentia and Gondwana, resulting in the supercontinent Pangea. This is known as the Alleghenian orogeny (Rast, 1984). Although the Alleghenian orogeny is part of a larger tectonic collision, this event is less dominant than the Acadian orgoeny in the study area (Rast, 1984). Rifts formed with the break-up of Pangea, and finally resulted in the opening of the Atlantic ocean.

5.2 Relevant findings in the study area

In this section I compile selected results from previous studies about the depth of lithospheric discontinuities and anisotropy in the study area.

5.2.1 Lithospheric structure

A receiver function study investigating intra-lithospheric variations beneath a permanent station (HRV) found signs of a velocity reduction of about 5% at depths too shallow to represent the LAB (Rychert et al., 2005). Results of the velocity/depth inversion can be found in Table 5.1, but I would like to highlight two results that will be particularly useful for this study: the

velocity reduction of $5.4 \pm 0.6\%$ at 60.9 ± 0.4 km, and the velocity reduction of $3.1 - 5.7\%$ mapped around the proposed LAB, occurring over less than 5 km.

Table 5.1: *Inversion results for station HRV from Rychert et al. (2005). The asterisk denotes parameters which have been inverted for.*

	Depth [km]	**Vs [km/s]**	**Vp/Vs**
Moho	30.2 ± 0.3*	3.79 ± 0.05*	1.69
Unknown	60.9 ± 0.4*	4.56	1.8
LAB	$96.6 - 96.8$*	4.31 ± 0.03*	1.8

The study of the LAB was expanded to a regional scale by Rychert et al. (2007), who investigated both Ps and Sp conversions to determine the velocity contrast across the LAB in eastern North America. They found that an abruptly velocity reduction (within less than 11km) of 3-11% occurs at depths in the range of 87-105km in eastern North America. The velocity reduction cannot be explained by a thermal gradient alone, and they suggest either a hydrated boundary coupled with a depleted boundary, or anisotropy (Rychert et al., 2007). They also investigated the contribution of anisotropy to the velocity drop, and attributed about 70% of the velocity reduction to a reduction of the isotropic component of mantle velocity.

At regional scale, Rondenay et al. (2000) noted a low velocity corridor striking NW-SE in the south eastern part of the Canadian shield, suggesting it could arise from passage of the continent over a fixed mantle plume (now forming the Great Meteor hotspot). The investigation was extended into the study area by Taylor and Fitzgerald (2011), who tracked the thermal conditions in the Adirondacks, New York (Figure 5.4). The NW-SE trend is persistent across the Grenville front and the Appalachians.

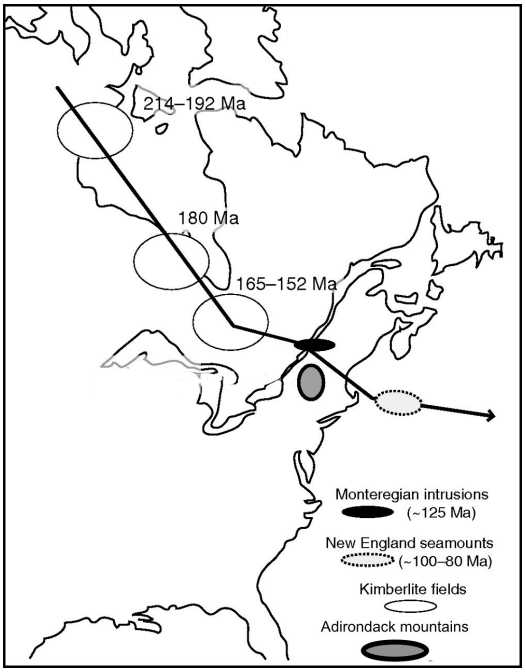

Figure 5.4: *Great Meteor hotspot track, modified from Taylor and Fitzgerald (2011). Study area is east of the Adirondack mountains.*

5.2.2 Anisotropic investigations

Multiple studies have investigated anisotropic features beneath the study area during the last 20 years. Both body waves and surface waves have been utilized in order to characterize the lithosphere and the asthenosphere. I briefly summarize results of some of these studies. The reader is referred to the individual publications for more details.

A shear wave splitting study by Fouch et al. (2000) provides splitting time close to 1s in the area, with indications of a complex anisotropic geometry. The study mapped no variations of splitting parameters with backazimuth, and concluded that anisotropy is present both in the lithosphere and the sub-lithospheric mantle. This study also investigated upper mantle anisotropy around lithospheric keels, and found that anisotropy in the sub-lithosphere is likely to vary with morphology of the lithospheric keel, deformation history, plate motion and rheology of the mantle (Fouch et al., 2000).

A surface wave study by Gaherty (2004) noted a Love-Rayleigh wave discrepancy in the study area, which was modeled with radial anisotropy. The S-wave anisotropy was found to increase rapidly to 4% beneath the Moho, and thereafter decreases evenly down to 110km, where anisotropy is further reduced.

Levin et al. (1999) modeled the anisotropic structure beneath the same station (station HRV) with shear wave splitting, and found three distinct changes in anisotropy (see Table 5.2 for a summary of obtained results). Layer 1 is an isotropic crust. They interpret layer 2 to be lithospheric anisotropy associated with the Appalachian orogen, and layer 3 to be the asthenosphere.

Table 5.2: *Anisotropic layering beneath station HRV, adapted from Levin et al. (1999). The % denotes the amount of anisotropy in the layer, for both P-and S-waves. Tilt (measured from the vertical) and strike correspond to directions of the fast axes.*

Layer	**Depth**	**Vp [km/s]**	**Vs [km/s]**	ρ $[g/cm^3]$	**%**	**Tilt**	**Strike**
1	0-35 km	6.0	3.0	2.5	0	-	-
2	35-135km	8.0	4.6	3.1	3	75	100
3	135-235km	8.0	4.7	3.1	4	130	50

5.2.3 Variations of azimuthal anisotropy with depth in North America

Yuan and Romanowicz (2010) mapped lithospheric anisotropy in North America, and found a change in azimuthal direction of the fast axis within the lithosphere. Azimuthal anisotropy the upper lithosphere is in the E/NE direction across the continent, and is attributed by Yuan and Romanowicz (2010) to large tectonic events such as the welding of Archean micro-continents and formation of the Appalachian chain. In the lower lithospheric layer, they find the fast axis consistently points towards the north, and attribute this to a thermal effect. They explain this lower anisotropy as a less depleted

layer, possibly because the upper layer acts as a chemically distinct lid which stops fluids from migrating further upwards. They also find that anisotropy beneath the LAB is in the direction of absolute plate motion, and attribute this to present day flow-induced anisotropy.

5.2.4 A low velocity lower crust in eastern North America

An investigation of crustal structures in eastern North America by Liang and Langston (2009) revealed the presence of several interesting intra-crustal low velocity layers. They first note a sedimentary layer with velocity of 2.0 km/s, varying in thickness from a few tens of meters to 5km across the study region, but very thin around the Appalachian chain. They also find that the velocity of the upper crust increases down to a mid-crustal boundary ranging from 10-25 km, where the S-velocity is reduced from 3.5 km/s to 3.25 km/s. This is called the low-velocity middle and lower crust. It should be noted that the study did not extend fully to the northern Appalachians, so the situation could be different there.

Chapter 6

Data

In this study we use data from broadband seismic stations compiled in a new database called GLImER. From the GLImER database, we have selected one particularly promising seismic station (HRV) for a thorough study of the lithosphere. Data from station HRV are supplemented with information from surrounding seismic stations, with the aim of expanding the study from a single depth profile to a regional study in eastern North America.

6.1 The GLImER database

Global Lithospheric Imaging using Earthquake Recordings (GLImER) is a new database containing receiver functions at permanent and temporary stations worldwide (Rondenay et al., 2017). The database contains land based stations with a minimum of 1.5 years recording time, resulting in 11456 seismic stations globally (downloaded December 2014) (Figure 6.1). Waveforms of seismic events with magnitude $m_b > 5.5$ and $m_b > 5.8$ were collected from temporary and permanent stations (respectively). Three component seismograms were collected from the Incorporated Research Institutions for Seismology (IRIS) web services, starting 30 seconds prior to the theoretical P-wave arrival, lasting for a total of 150 seconds. Due to the vast number

of waveforms, RFs in GLImER were generated automatically following the steps described in Chapter 3.3.

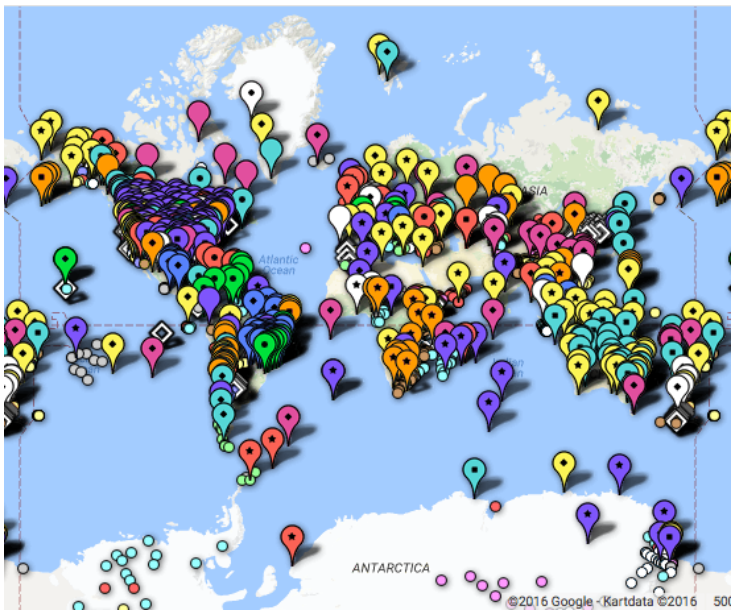

Figure 6.1: *Distribution of seismic stations in GLImER. Different networks are marked by different colors and symbols, so that they can easily be separated from each other. For example is the network IU, part of the Global Seismograpic Network (GSN), marked by yellow pins with a diamond. The station coverage is particularly high in North America, in large part due to the transportable array (TA) network.*

6.2 Station HRV

Station HRV was selected as a promising candidate for studies of the MLD due to its long operational time, and ideal location with respect to global seismicity. HRV is part of the Global Seismographic Network (GSN) under network code IU, in cooperation with IRIS, department of Earth and Planetary Sciences at Harvard University, and the U.S. National Science Foundation. The station has been running since 1988. It is located near Boston Massachusetts (USA), at 42.5064°N, 71.5583°W, and an altitude of 200m.

GLImER contains 486 seismic events above magnitude 5.8 recorded at station HRV between January 2, 1988 and December 26, 2014, which satisfy the GLImER criteria for signal to noise ratio and quality control (Rondenay et al., 2017). The resulting 486 RFs have ray parameters ranging from 30° to 90° and good backazimuthal coverage (Figure 6.2a). The ray parameter average is 0.063 s/km (Figure 6.2b). The only significant gaps in backazimuth are found around 100° and 150° backazimuth (Figure 6.2c)

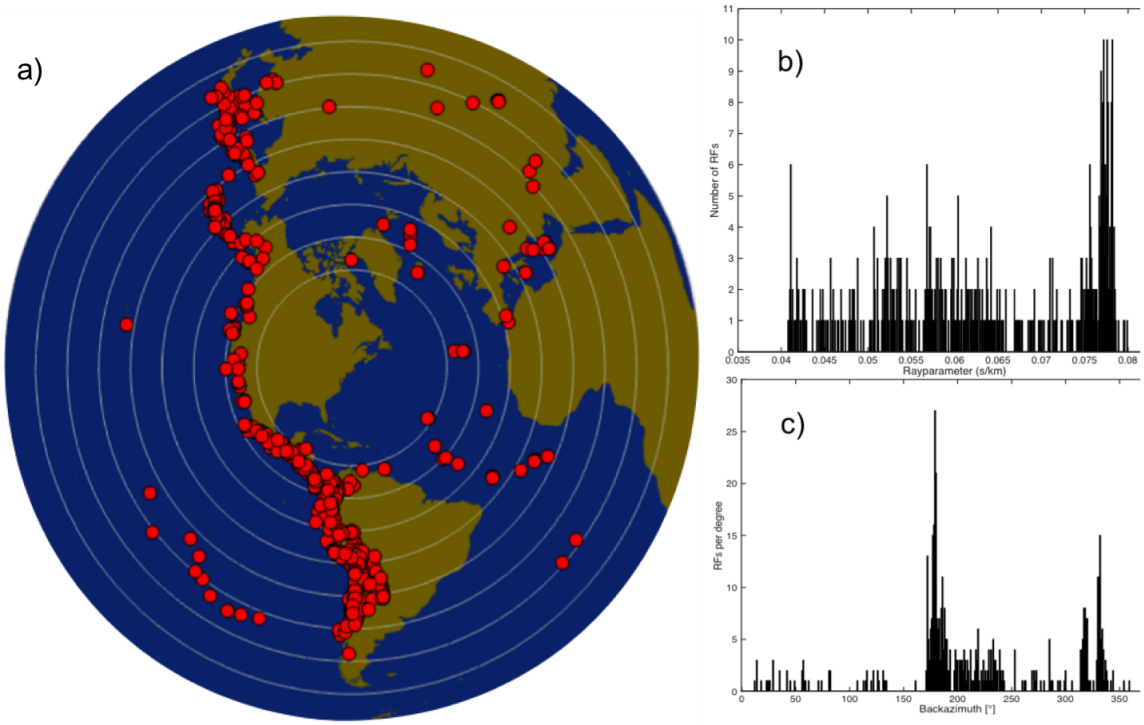

Figure 6.2: *a) Location of RFs with respect to station HRV. b) RFs distribution with ray parameter. c) RFs per degree backazimuth. The events causing the large peak in backazimuth at 180° are found to coincide events with ray parameters around 0.078 s/km*

6.3 Regional seismic station coverage

The region where HRV is located has a high coverage of seismic stations due to the presence of several seismic networks (Figure 6.3). Purple pins without any symbols represent the Lamont-Doherty Cooperative Seismographic Network (LD), a network set up to monitor earthquakes in eastern North America. The white pin is part of United States National Seismic Network (US), while the yellow pin is HRV.

Most of the stations in this area are part of the Earthscope transportable array (TA), a large network of transportable broadband seismometers deployed with aim to cover the whole mainland of USA. The array consists of 400 broadband seismometers that have been deployed on a systematic grid all across USA (*http : //usarray.org/researchers/obs/transportable*, November 2016). The seismometers are deployed with 70km spacing on a regular grid pattern, thus enhancing the potential of high resolution estimates of subsurface structures beneath North America. When deployed, each seismometer records for a period of 2-2.5 years, before it is moved to a new location. Stations within TA thereby meet the GLImER criteria for recording time.

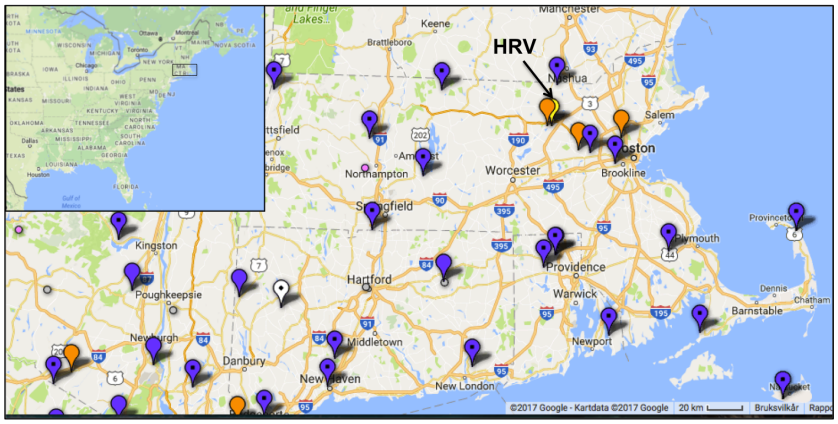

Figure 6.3: *Seismic station coverage in the study area. The yellow pin is station HRV, and purple pins with a square represent stations in the TA network.*

Chapter 7

Method

This chapter presents the modeling methods and the tools used to investigate a possible MLD beneath station HRV. In particular, the chapter provides an overview of the work flow, starting with synthetic tests and ending with the preferred model of the subsurface beneath station HRV. Finally, there is a discussion of some potential pitfalls associated with the work that is carried out.

7.1 Program and displays

This section provides a description of RAYSUM, the program used to generate synthetic sections of RFs. It also describes the displays created for extracting information about anisotropy and dip from real and synthetic data.

7.1.1 RAYSUM

Synthetic seismograms have been generated for a range of isotropic and anisotropic velocity models. Synthetic seismograms are generated from the

program RAYSUM, presented in the paper by Frederiksen and Bostock (2000)[1]. RAYSUM generates synthetic seismograms for planar waves traveling through a stratified medium (Frederiksen and Bostock, 2000). Travel times are calculated from a decomposition of the ray path between source and receiver into vertical and interface-parallel segments. Amplitudes are computed according to the method of Fryer and Frazer (1984) described in Chapter 3.2.3. The velocity model accepts both planar and dipping interfaces, and layers can be isotropic or anisotropic. However, the program does not allow for inclusion of 3D-heterogeneties.

The default values of RAYSUM have been altered to fit GLImER data for easier comparison to HRV data. This includes a sampling interval of 0.1s and a Gaussian source wavelet with a 0.5s pulse width. The ray parameter was fixed to 0.06 s/km, the reference value which was used to normalize the travel time of traces in GLImER, and the average ray parameter for RFs at HRV (Figure 6.2). One RF was generated per degree backazimuth for complete backazimuthal coverage, thus making it possible to observe the effect of changing individual parameters (Figure 7.1).

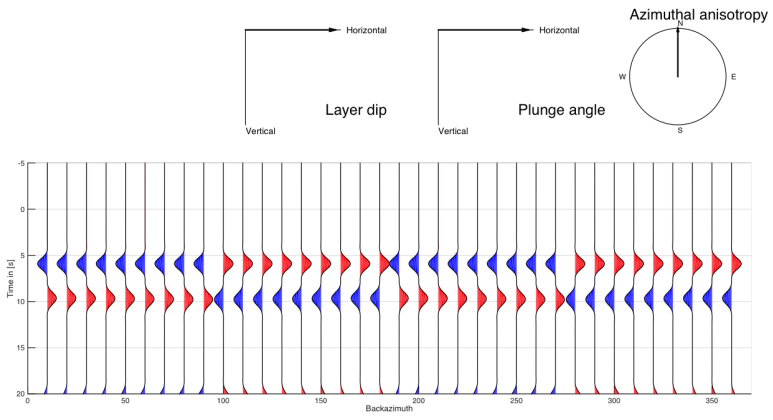

Figure 7.1: *Transverse component showing a simple synthetic model of one isotropic layer overlaying an anisotropic half-space. The half-space has a horizontal fast axis of anisotropy, towards the north.*

[1]The program is made publicly available on https://home.cc.umanitoba.ca/~frederik/

7.1.2 Displays

Two main display types have been generated for the investigation of synthetic RFs. The first display is based on Figure 4.1, with signals instead of colors for easier and more accurate interpretation. The second display is of the harmonic decomposition - both individual components and sums of components for the higher order harmonics.

Sections of receiver functions with backazimuth

The main display program generated in this project sorts, stacks and displays RFs with backazimuth as colored signals instead of the colored sections shown in Figure 4.1. Full signals are beneficial compared to colored sections because it is easier to locate the exact backazimuth of polarity reversal, and map amplitude variations.

RFs are first bandpass filtered with cut-off frequencies 0.01 Hz and 1.1 Hz. This minimizes loss of low frequency signal and removes signal arising from near surface features. The Nyquist frequency of GLImER data is 5 Hz.

RFs are binned and stacked by backazimuth, thus removing the dominant effect of high seismic corridors in the data. Bin widths from 1° to 40° were tested. The benefit of narrow bins is that less detail is lost in the stacking process, but an image with many bins can be rather messy to interpret. The synthetic sections in this thesis are mainly generated with 10° bins. An option of overlapping bins was added with the aim of reducing data gaps, but for the purpose of detecting sharp changes in polarity this was not a useful tool. Overlapping bins has therefore not been included in the forward modeling process.

The relative signal strength of the transverse component compared to the radial component is weak due to less SH energy than P and SV. In figures displaying both the radial and the transverse component, the signal strength of the transverse component becomes too weak to interpret. The transverse

component is therefore up scaled by 4.5 compared to the radial.

Harmonic decomposition displays

I generate two displays to investigate energy on the first three harmonics. The first display contains the individual components of the harmonic decomposition, displaying the amount and polarity of energy on the sines and cosines at all time intervals (Figure 7.2). The harmonic decomposition also includes a summed harmonic display, where the absolute value of the higher order harmonics are summed, both for the individual values of k, and for the sum of all higher order harmonics (k=1,2) (Figure 7.3). The summed harmonics is computed with Equation 7.1. This display highlights the time at which anisotropic/dip is strongest, regardless of type of anisotropy/dip and direction.

$$k = \sqrt{k_{1,NS}^2 + k_{1,EW}^2 + k2_{2,NS}^2 + k_{2,EW}^2} \tag{7.1}$$

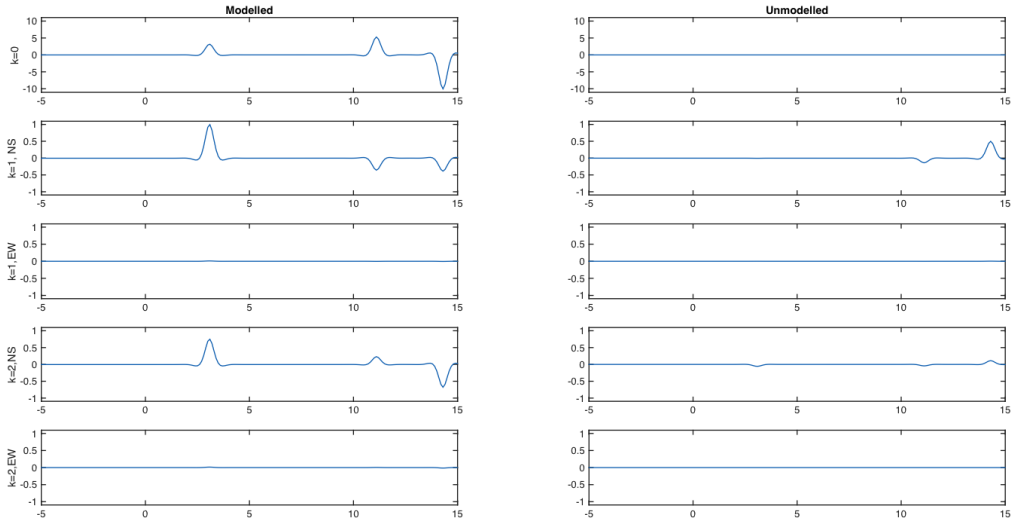

Figure 7.2: *Harmonic decomposition of a one layered model overlaying an anisotropic half-space with a plunging fast axis towards north, plunging at 45°. The pulse around 3s represent the boundary between the isotropic and the anisotropic layer, the two other pulses correspond to multiples.*

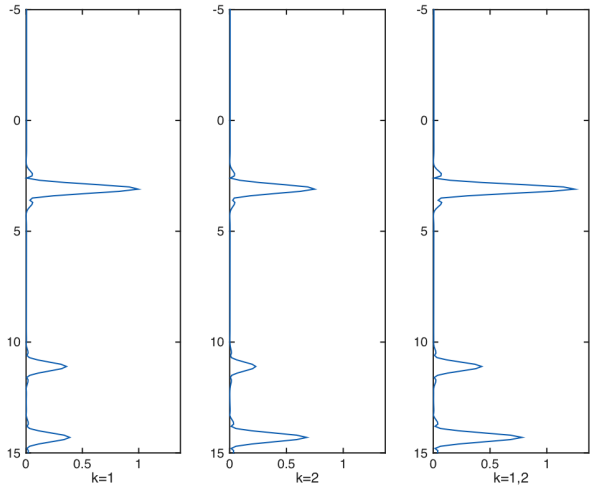

Figure 7.3: *Signal on the higher order harmonics (k=1 and k=2) shown in Figure 7.2, and the sum these (k=1,2). Y-axis represents time in seconds after direct P-wave arrival.*

7.2 Work flow

This section discusses the steps in the modeling process leading to a reliable model of lithospheric structures beneath station HRV. The first step is to get familiarized with how specific parameters such as anisotropy and dip cause energy to appear on the radial and transverse component, and how these features are displayed in the harmonic decomposition plots. The second step is an investigation of the recorded energy at station HRV, including a visual interpretation of the individual components and the harmonic decomposition. The third and final step is to use information obtained from the synthetics to create a model that represents lithospheric structures beneath HRV. This is achieved by fitting synthetic data to observed data from station HRV through forward modeling, where a solution should match both the individual components and the resulting harmonic decomposition.

7.2.1 Synthetic modeling

Synthetic receiver functions are generated to study how energy appears on the harmonic decomposition and radial/transverse components for a range of end-member cases of anisotropy and dip. As several parameters influence the modeling results, their effects are isolated by varying only one parameter in each iteration. The structural model is a simple one layer model overlaying a half-space, with fixed velocities and densities. Isotropic properties of the model have been selected in such way that the boundary represent the approximate Moho depth beneath station HRV (Figure 7.4). Depth and velocities/ densities are from Rondenay et al. (2017) and Rychert et al. (2005) respectively.

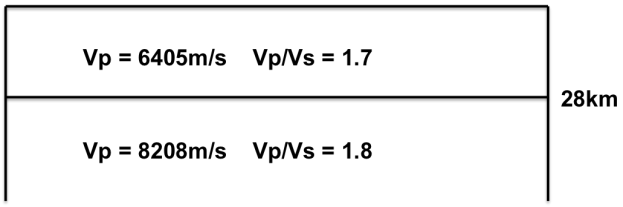

Figure 7.4: *The simple one layer model overlying a half-space used to generate synthetic sections of RFs. Velocities and depth of the interface correspond to the Moho beneath station HRV as reported by Rychert et al. (2005); Rondenay et al. (2017).*

Properties of Table 7.1 are added to the simple velocity model, and synthetic RFs are generated with RAYSUM. The fast axis is plunging towards the north for the plunge models, and the top layer (representing the crust) is isotropic in all models. Anisotropy of the half-space is fixed to 5.5% for both P and S-waves, and only hexagonal anisotropy is considered (see Chapter 2). Although the most anisotropic rocks have larger magnitude shear wave anisotropy than compressional wave anisotropy (Babuska and Cara, 1991), the assumption about equal anisotropy for P- and S-waves has been adapted to reduce the number of modeling parameters.

An example of the synthetic sections generated can be seen in Figure B.1,

where the half-space has a fast axis of anisotropy trending north. Only the "modeled" harmonics (corresponding to anisotropy or dip) is included, as values of the "unmodeled" harmonics correspond to scatterers and heterogeneties, which are not present in the synthetic models.

Table 7.1: *The range of synthetic models investigated in order to map the appearance of energy on the transverse component and the resulting harmonic decompositions.*

Dip [°]	1	2	5	10	15	20	30	40	50
FA direction [°]	0	45	90	135	180	225	270	315	
FA plunge [°]	1	5	10	15	20	25	30	35	40
			...	45	50	55	60	70	80

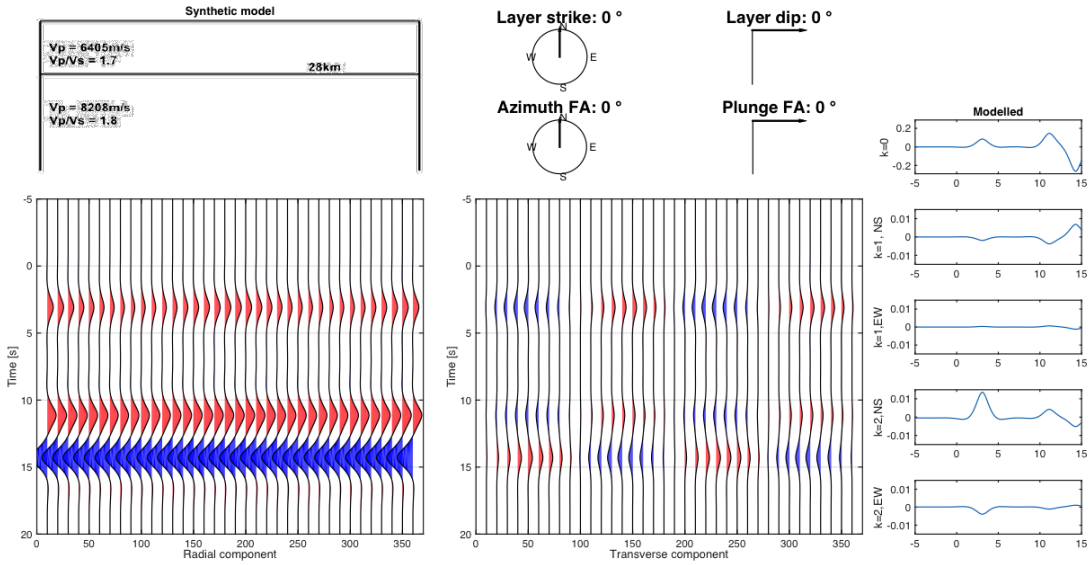

Figure 7.5: *Example of display for simple synthetic models, containing both information about the anisotropy and lack of dip, and the resulting harmonic decomposition. Note that the transverse component is up-scaled by a factor of 4.5 compared to the radial.*

Multiples are not included in the forward modeling process for two reasons. First, synthetic modeling of the approximated Moho beneath station HRV generates multiples arriving too late to influence intra-lithospheric discontinuities (Figure B.1). As Rychert et al. (2005) found that the MLD beneath HRV is unlikely to correspond to a multiple, this should not influence the forward modeling results. Secondly, due to the fact that synthetic receiver functions are generated with a fixed ray parameter, the multiples from all directions sum up constructively, making multiples the dominating signals in the synthetic sections (see Figure B.1, at 11s and 14s).

7.2.2 Investigating station HRV

RFs were downloaded from GLImER September 14, 2017. The main discontinuities (Moho, MLD and LAB) were mapped on the sum of all radial RFs prior to sorting and stacking. This was done to avoid weighting of traces depending on the number of elements within each stack. Polarity reversals were determined by extracting amplitudes along the backazimuthal range on the transverse component, for the time picked from the summed radial. As the MLD is the main focus of this study, data is displayed from -5s to 15s. The low-cut frequency was altered to see if energy arising from shallow multiples contribute to the signal. High-cut was altered to see if the MLD appears more clearly for some frequency bands.

7.2.3 Generating a model for station HRV

As seen in previous chapters, the wave propagation through an any solid material depends on several parameters, such as seismic velocity, density and anisotropy. In order to limit the extent of this thesis, some parameters are constrained ahead of the forward modeling process. These constraints are based on previous findings in the study area and some simplifications. For anisotropic properties I assume hexagonal anisotropy, and equal anisotropic magnitude for P and S-waves. Estimates of Vp, Vs, density, dip, strike, and

anisotropic properties of each layer are then obtained through a systematic grid search. The flow chart in Figure 7.6 describes how parameters were estimated in an individual layer. As the number of layers is also unknown, I utilize previous findings for station HRV to construct an initial synthetic model containing three main boundaries beneath HRV (Figure 7.7). Although Yuan and Romanowicz (2010) map the LAB to be a gradual transitional boundary, it is modeled with a sharp interface here as RAYSUM does not include an option for gradually transitioning interfaces[2]. As the main focus of this study is to map features around the MLD, this simplification should not affect the forward modeling of an MLD.

The fitting of a synthetic model to the real data is based on the least deviation between the real and a synthetic model for a time window spanning the MLD, primarily based on visual interpretations and measurements of maximum peak. As many different models can provide similar results, I seek the best fit for the simplest model possible, following Occam's Razor principle (Blumer et al., 1987). I propose to conduct my test by following the flow chart depicted in Figure 7.6, which will allow me to address a set of scenarios: 1) Isotropy and a horizontal boundary; 2) Isotropy and a dipping boundary; 3) Horizontal anisotropy and a horizontal boundary; 4) Plunging anisotropy and a horizontal boundary; 5) Horizontal anisotropy and a dipping boundary; and 6) Plunging anisotropy and a dipping boundary. The crust remains a simple isotropic layer, according to the findings of Levin et al. (1999), and the LAB mark a transition to a half-space (layer D in Figure 7.7) with horizontal anisotropy parallel to the absolute plate motion (APM) (Yuan and Romanowicz, 2010). By gradually changing the parameters of this model I seek a solution that fits reasonably well both the radial component and the harmonic decomposition, and follows the polarity reversal pattern of the transverse component.

[2]This could be simulated using several thin layers with gradually changing properties, but as this introduces additional computation time it has not been included.

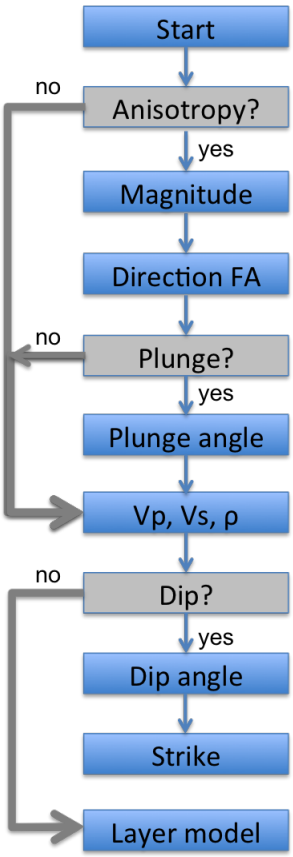

Figure 7.6: *Flow chart summarizing the forward modeling process for a single layer in this thesis.*

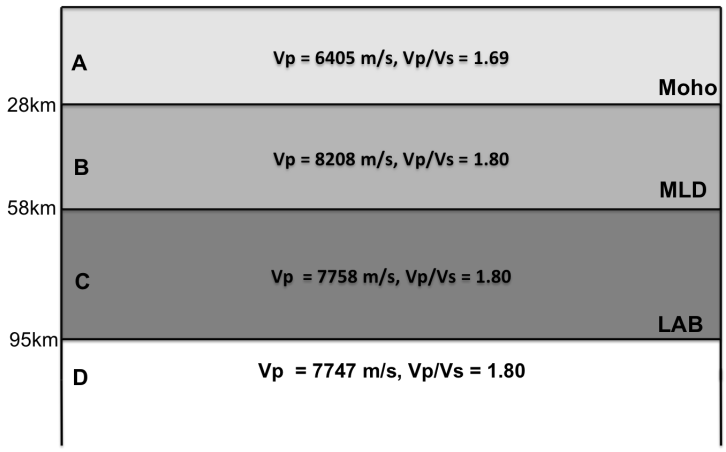

Figure 7.7: *Initial model of the subsurface beneath station HRV. Velocities from Rychert et al. (2005) and depths from Rondenay et al. (2017).*

7.2.4 Expanding the study to surrounding stations

By comparing the receiver functions and harmonic decompositions at other stations in the study area, I have a quick way to check whether features beneath HRV are purely local or can be expanded to surrounding stations. I generate plots of stacked radial components and the sum of k=1 and k=2 for each station. I then compare them along a line through the area, where the line is approximated from a least squares approximation between the locations of relevant stations.

7.3 Potential pitfalls and limitations to the method

As always, there are a number of choices made through a project that will add uncertainties to the obtained results.

The main consideration that must be made with respect to interpretation is that this forward modeling process is a problem with many potential solutions, and more than one model could be a good match. Evaluation of synthetic models is mainly based on visual interpretation, adding uncertainties to the results. As I aim for the simplest possible model to fit the HRV data, the robustness of the manual forward modeling method itself must be considered before implications of the results are discussed.

The following sections address specifically the potential issues associated with the influence of fixed modeling parameters and uncertainties from simplifications.

7.3.1 Uncertainties related to choice of fixed modeling parameters

The real data contains a range of ray parameters (p), while the synthetics are modeled with a fixed ray parameter of 0.06 s/km. I therefore carry out an investigation of how the ray parameter influences the resulting synthetics, to see how much this choice must be accounted for in the interpretation. I do this by comparing single values of ray parameters for all backazimuths with each other, and with random distributions of ray parameters between 0.04 s/km and 0.08 s/km, the dominant ray parameter range for HRV (Figure 6.2). Increasing p causes the signal to appear at a later time, which can be explained by the longer ray path through the medium. For a random distribution of p, the signal is recorded at a time corresponding to the average ray parameter. The synthetic data is generated with $p = 0.06$ s/km, and the average p for HRV is 0.063 s/km. Traces within GLImER have also been normalized with $p = 0.06$ s/km, so I conclude that the choice of $p = 0.06$ s/km is appropriate for synthetic modeling.

The choice of pulse width determines the level of accuracy that can be mapped, but for realistic forward modeling the pulse width must coincide with the real data. The width depends on the Gaussian pulse input in RAYSUM, but also on the filtering, as removal of high frequencies causes the pulse to appear wider. Several Gaussians were therefore tested against the radial stack of HRV, resulting in a best fit for the Moho pulse width when the Gaussian pulse is 0.5s, for a frequency band of 0.01-1.1 Hz.

7.3.2 Uncertainties due to simplifications

The stratified Earth model beneath HRV is highly simplified, and does not include features within the crust. Even though the main lithospheric boundaries do not produce multiples interfering with the time interval of interest, shallow structures could cause multiples appearing there. Even though Rychert et al. (2005) found that neither the MLD nor the LAB are related to

multiples, the potential interference of shallow signals has not been included in the forward modeling process, which could add inaccuracies.

As previously described, the stacking may cause a weighted average which could introduce errors in the dataset if seen as a single RF. This has been avoided in the regional profiles by summing non-binned RFs. This results in equal weighting of each trace. Although the resulting summed RF avoids the initial weighting issue, the new challenge is that receiver functions with strong impulses are more dominating in the sum.

In the synthetic modeling process, there is no option to generate smoothly varying transitions from one layer to another, without adding several thin layers (as previously discussed). Property changes are not expected to occur so abruptly in the deep crust /upper mantle (E-supplement Rychert et al. (2005)), so these sharp transitions between different anisotropic material is introducing extra energy in the synthetic RFs.

Chapter 8

Synthetic modeling of upper mantle structure

This chapter presents the influence of varying parameters, such as anisotropy and dip, on synthetic modeling. The parameter influence will be of great importance in the interpretation and forward modeling of station HRV. A few examples will be provided for each type of model, and the reader is referred to Appendix B for the full range of models.

8.1 Azimuthal variations to a horizontal fast axis

A horizontal fast axis exhibits π symmetry and no curvature of the signal in the RF section display (Figure 8.1). For a fast axis with azimuth 0°(north), the reversals occur at 0°, 90°, 180° and 270° backazimuth. The reversals shift with 45° for every 45° rotation of the fast axis. The signal strength decreases evenly towards each polarity reversal, and the backazimuth where polarity changes from positive to negative represents the direction of the fast axis (Appendix B).

Harmonic decomposition of signals arising from a layer with horizontal anisotropy primarily results in energy on the k=2 component for all azimuthal directions (Figure B.1 and Appendix B). At k=1 there is some negative energy on the NS component, regardless of azimuthal direction of the fast axis. At k=2, the energy on each component (NS or EW) is related to the azimuth of the fast axis. k=2_{NS} has the largest amplitudes when the fast axis is directly north, east, south or west (0°, 90°, 180°, and 270°), and the strongest signal on k=2_{EW} is recorded at azimuths between these (45°, 135°, 225° and 315°). The k=2_{NS} component is positive for a fast axis trending N-S, and negative for fast axis trending E-W. The k=2_{EW} component is positive along the NE-SW axis (45°/225°), and negative along the NW-SE axis (135°/315°), and thereby follows the pattern of the NS component by a phase shift of $\pi/4$.

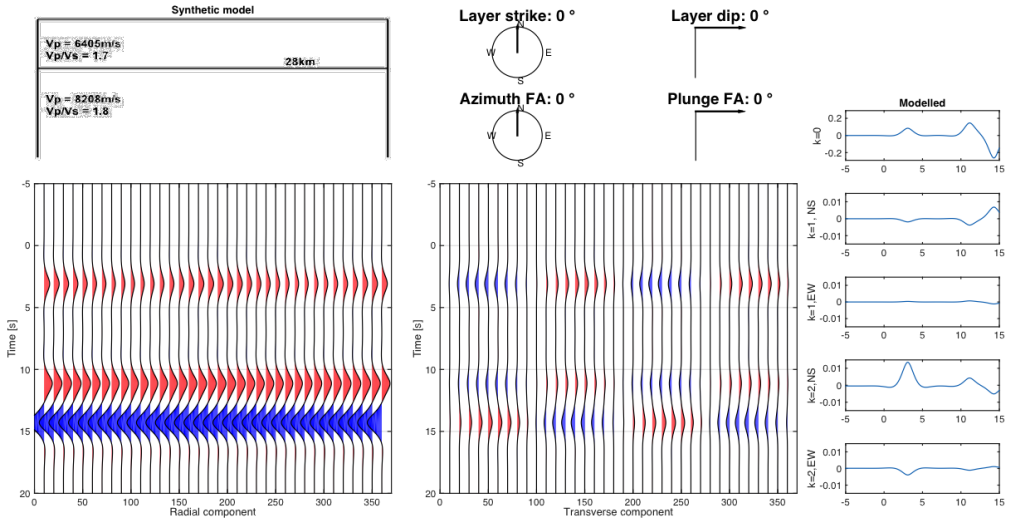

Figure 8.1: *Resulting radial and transverse component for a simple synthetic model with horizontal axis of anisotropy with azimuth 0 °. Left: radial component, center: transverse component, and right: a harmonic decomposition of the radial and transverse component (only the modeled harmonics (Q+iT)).*

Through the modeling process it became evident that the anisotropic signal is different at the top of a layer compared the bottom of the layer, and that the polarity of these signals depends on the velocity contrast across

the interface. The upper boundary is simply characterized by a change of polarity from positive to negative corresponding to the fast axis. However, signals arising from the lower boundary of an anisotropic layer have a polarity change which depends on the velocity in the layer below. Determination of the fast axis based on the lower boundary signal can therefore not be carried out without robust estimates of the velocity change across the boundary. For a fast to slow interface with increasing depth, the fast axis is given by the change from negative to positive polarity (Figure 8.2). For a slow to fast interface with increasing depth, the fast axis is given by the change from positive to negative polarity (Figure 8.3). When there is no velocity change with depth, the fast axis is indicated by a polarity change from negative to positive at the lower boundary (Figure 8.4). This means that if several anisotropic layers are present, it is essential to know if the signal we interpret arises from anisotropy in the layer above or below the interface.

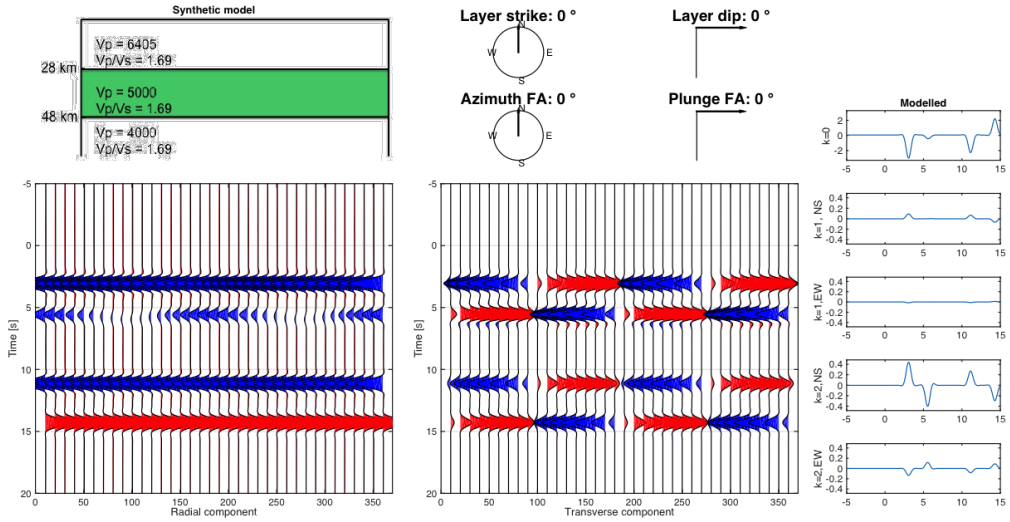

Figure 8.2: *Two layers overlaying a half-space with a velocity reduction with depth. Model in the upper left corner gives velocities and depths. Density is 2600 kg/m^3. The green color indicate the anisotropic layer, and the anisotropic parameters are indicated at the top (right/middle). Bottom figures shows R and T as function of backazimuth.*

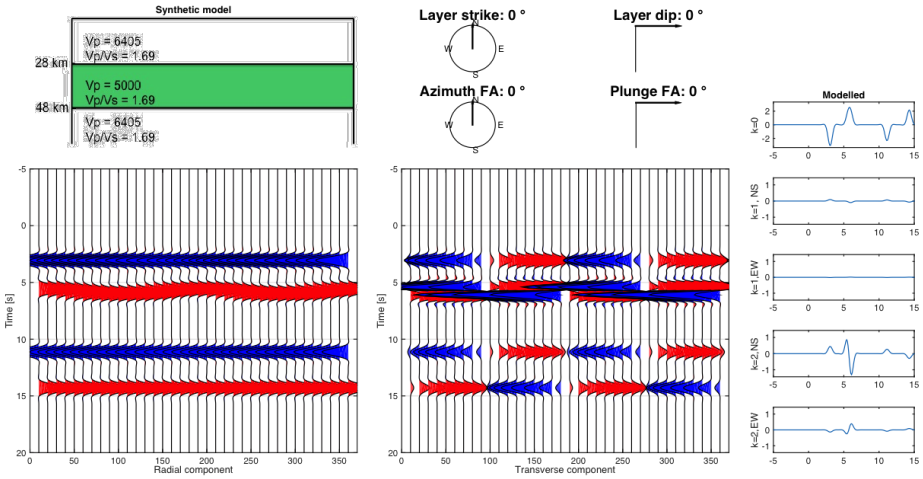

Figure 8.3: *Two layers overlaying a half-space with a low velocity layer between higher velocity at top and bottom. Model in the upper left corner gives velocities and depths. Density is 2600 kg/m^3. The green color indicate the anisotropic layer, and the anisotropic parameters are indicated at the top (right/middle). Bottom figures show R and T as function of backazimuth.*

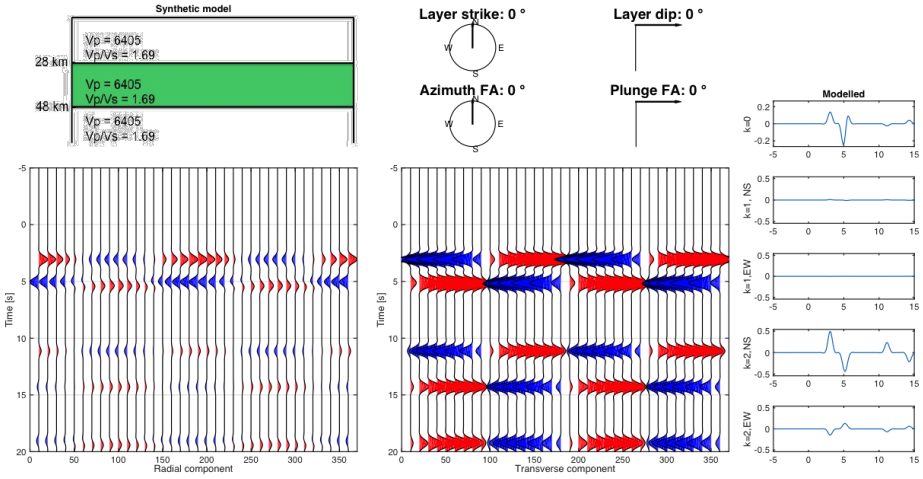

Figure 8.4: *Two layers overlaying a half-space, the velocity increases with depth. Model in the upper left corner gives velocities and depths. Density is 2600 kg/m^3. The green color indicate the anisotropic layer, and the anisotropic parameters are indicated at the top (right/middle). Bottom figures show R and T as function of backazimuth.*

8.2 A plunging fast axis of anisotropy

A plunging fast axis exhibits a visual π symmetry on the RF display up to 45° plunge, changing to 2π symmetry when the plunge of the fast axis exceeds 50°. The maximum amplitude of the signal increases with plunging angle up to 60°, without travel time variations with backazimuth. Polarity reversals follow those of horizontal anisotropy, with the direction of fast axis following the polarity reversal from positive to negative (Figure 8.5).

Investigation of the harmonic decomposition for plunging fast axis models provide better constraint on the change from π to 2π symmetry. Energy on the k=1 component gradually increases with increasing plunge angle, reaching its maximum strength at 30° plunge. At 30° plunge the energy is equal on k=1 and k=2, and when the plunge angle exceed 30 °, the energy on the k=2 component is gradually reduced. This is in contrast to the individual component display, where energy of the middle two polarity bands is a lot weaker and narrower than the two outermost polarity bands (Figure 8.5). The offset between individual components and harmonic decomposition can be explained by the difference between a visual interpretation of amplitude (R and T) and the harmonic decomposition which consider only polarities.

For increasing plunge angle the total signal strength on the transverse component is reduced. This is expected, as the amount of SH energy is reduced with a fast axis oriented closer to the vertical (Babuska and Cara, 1991).

The strongest signal on the harmonic decomposition is found for a plunging axis at 45°. The combined signal of k=1 and k=2 increases up to 45 degrees, and then start to decline (Appendix B, Figure B.44). This is as expected, as the decline arises due to the reduction of energy on the transverse component when the fast axis approaches the vertical (Babuska and Cara, 1991).

The main finding of this test is that the polarity of k=1 changes depending on azimuth of the fast axis. Appendix B contains the full range of harmonic decompositions for different plunging angles and directions. Table 8.1 summarizes the pattern of polarity changes from these figures, for the two k=1 components.

Table 8.1: *Polarity of $k1_{NS}$ and $k1_{EW}$ for a fast axis plunging with 60°. Numbers indicate the azimuthal direction of the fast axis, and +, - , 0 indicate positive polarity, negative polarity and no amplitude (respectively).*

	0°	45°	90°	135°	180°	225°	270°	315°
NS	+	+	0	-	-	-	0	+
EW	0	+	+	+	0	-	-	-

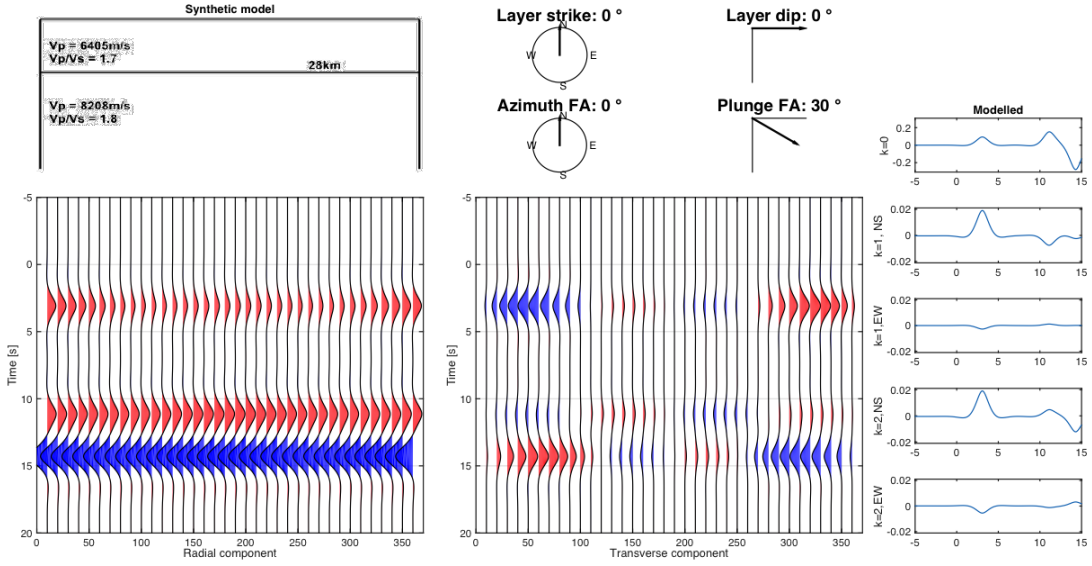

Figure 8.5: *Transverse component for the simple synthetic model, when the half-space has a plunging axis of anisotropy, plunging at 30° towards north. Note that around 3s, the amplitudes are equal on the k=1 and k=2 components.*

8.3 A dipping interface

The signal strength on the transverse component arising from a dipping interface increases with increasing dip of the layer. The signal is recorded at the same time regardless of backazimuth, but the multiples have variations in travel time along the backazimuthal range. The signal strength along the backazimuthal range increases and decreases twice before the polarity reversal occurs (Figure 8.6)

One of the most striking features of the dipping layer investigation is the energy arriving at time zero. This happens as energy rotation of the direct P-wave is not perfect, causing direct P-wave energy to appear in the radial and transverse component when dip has not been accounted for. This change of polarity at time zero in the radial component can be used to indicate the presence of a dipping layer (Frederiksen and Bostock, 2000). The exact location of this dipping boundary can however not be determined based on this information alone.

The harmonic decomposition of a synthetic dipping interface results in energy primarily on k=1. k=1_{NS} only contain energy while the layer is dipping towards north (Figure 8.6). There is also some energy around 3s for k=2, likely to arise from the amplitude variations within the signal. The energy around 3s is the only part of the signal representing a physical boundary, all the other energy is caused by multiples and imperfect energy rotation.

The relative strength of the k=2 to k=1 decreases as dip is increasing, and the total energy on the harmonics increases with increasing dip angle. This can also be seen on the total energy plot for all dips, where each increase in dip is causing an increase in the total anisotropic/dip energy (Appendix B, Figure B.45). As the dip increases, multiples appear earlier in the signal.

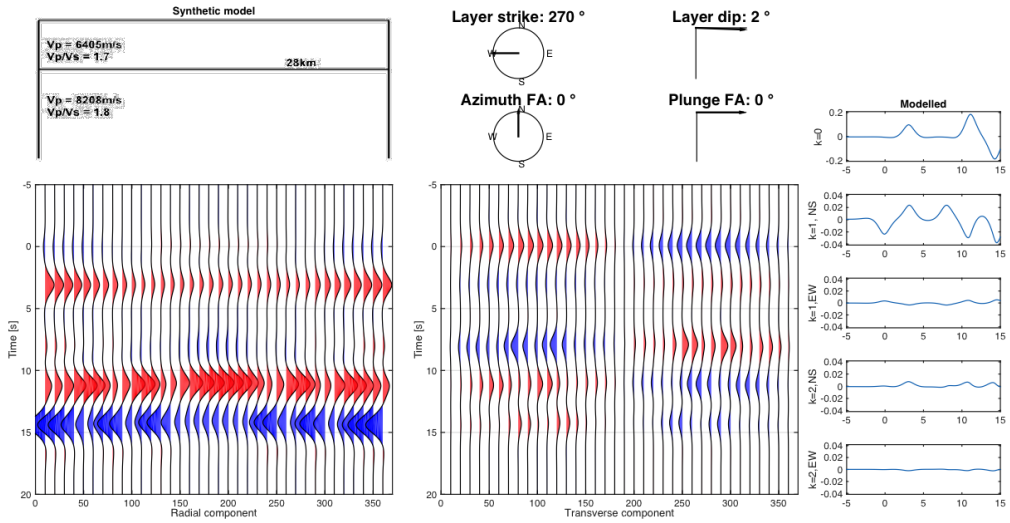

Figure 8.6: *Interface dipping at 2° towards north, producing energy at time zero, around 3s (from the interface), and a set of multiples.*

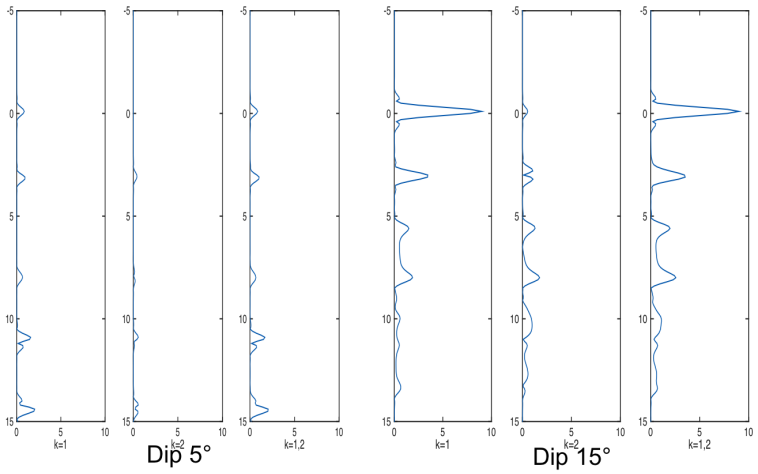

Figure 8.7: *Comparing the total energy of two simple models, an interface dipping at 5° (left) and an interface dipping at 15° (right). The total energy increases with larger dip, and is particularly evident around time zero.*

8.4 Combining dip and anisotropy

The final investigation of synthetic data combines azimuthal anisotropy (horizontal or plunging FA) with a dipping layer. For a model with horizontal anisotropy and a dipping boundary, the signals shape and polarity depends on the strike direction of the boundary relative to the azimuth of the fast axis (Figure 8.8 and 8.9). When the strike of the layer is changed by 180°, the polarity pattern of the transverse component is reversed at the time corresponding to the interface, while the polarity pattern of energy at time zero depends on strike direction. When strike is in the same direction as the fast axis, the multiples are concave upwards. When the strike is in the opposite direction as the the fast axis, the multiples are convex upwards. The multiples thereby hold useful information if both anisotropy and dip is present.

As these examples represent a rather special scenario, (parallel strike and dip), Appendix B.3 contains a few examples where the fast axis azimuths are perpendicular and oblique (30°) to the strike. Although less apparent, the same trends arises in these examples.

The azimuth of a plunging axis with respect to the dip of the layer determines the width of each polarity band in the signal corresponding to the interface (Figure 8.10 and 8.11). If the FA plunge is in the same direction as the layer strike, the width of the middle polarity band is increased. When they are in opposite directions, the width of the middle band decreases. An example is seen in Figure 8.11, where positive impulses dominate the interface at Moho depths.

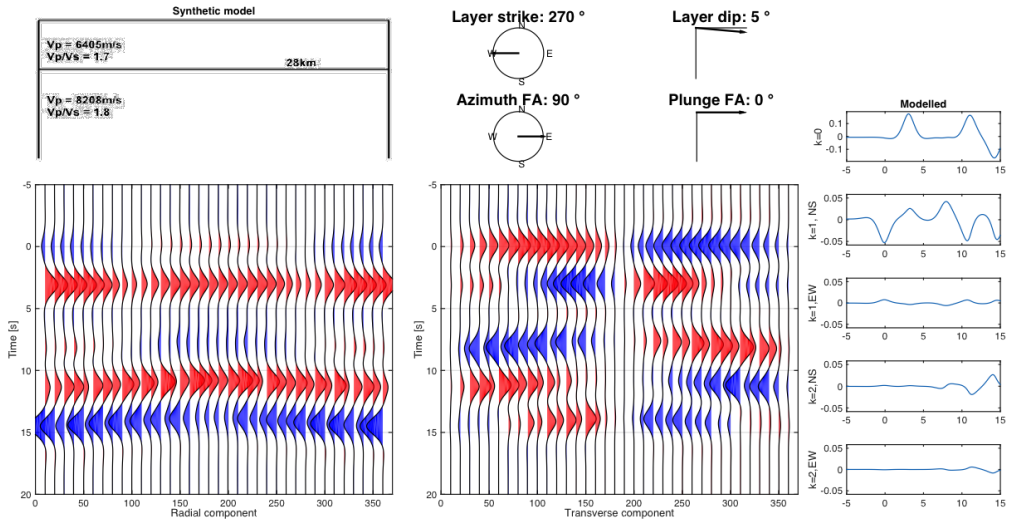

Figure 8.8: *Synthetic seismogram of RFs for a horizontal axis of anisotropy in a dipping layer. The fast axis is towards east, and the layer is dipping towards north.*

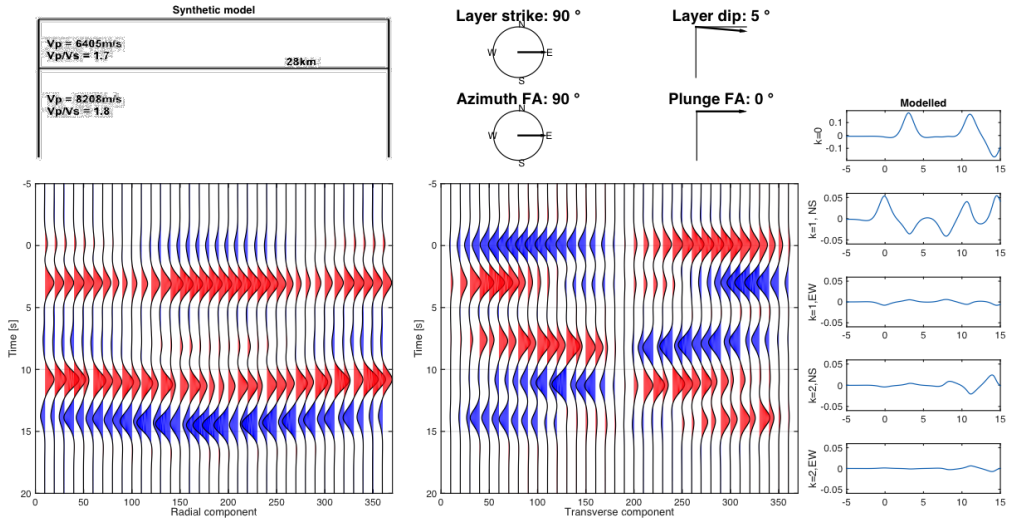

Figure 8.9: *Synthetic seismogram of RFs for a horizontal axis of anisotropy in a dipping layer. The fast axis is towards east, and the layer is dipping towards south.*

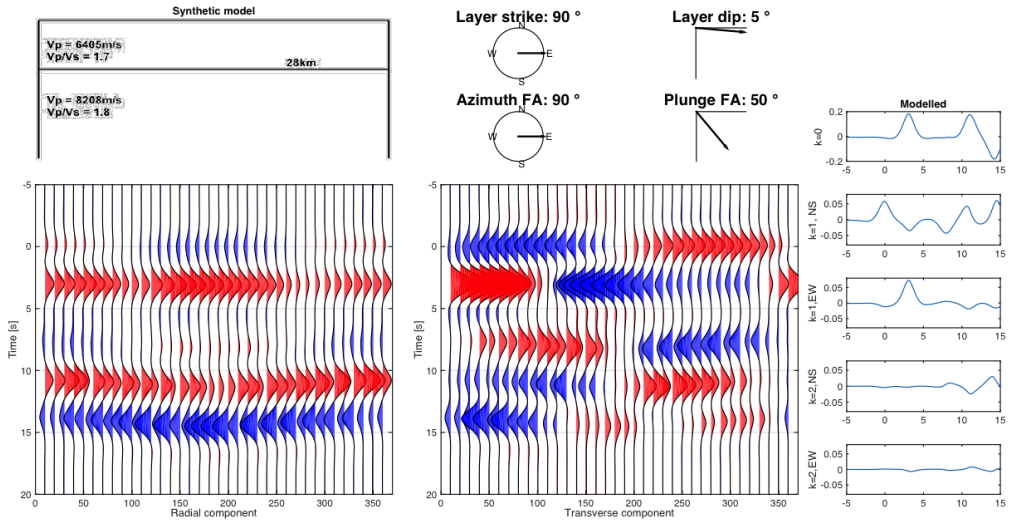

Figure 8.10: *Synthetic seismogram of RFs for a dipping interface, with a plunging axis of anisotropy. The fast axis is plunging towards east, and the layer is dipping towards south (axis of anisotropy in the strike direction)*

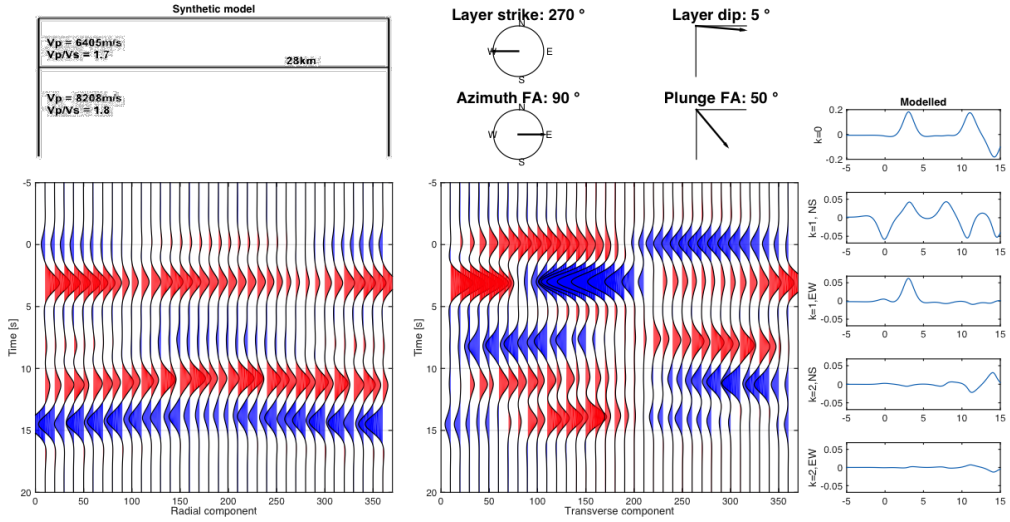

Figure 8.11: *Synthetic seismogram of RFs for a simple one-layer dipping interface, with a plunging axis of anisotropy. The fast axis is plunging towards east, and the layer is dipping towards north (axis of anisotropy opposite of the strike direction)*

Chapter 9

Results

This chapter presents the analysis of HRV data, and the main result of this thesis: a proposed lithospheric model beneath station HRV. This result is accompanied by regional profiles of radial RFs and summed harmonic decompositions crossing through the Appalachians into the Archean craton.

9.1 Analysis of HRV data

9.1.1 Radial stack

Three main discontinuities are picked from the sum of all radial receiver functions (Figure 9.1). The Moho is picked at 3.32s, the MLD at 6.50s, and the LAB at 10.40s, based on times of maximum peak/troughs within a time window corresponding to previously reported depths (see e.g. Rondenay et al. (2017); Yuan and Levin (2014)).

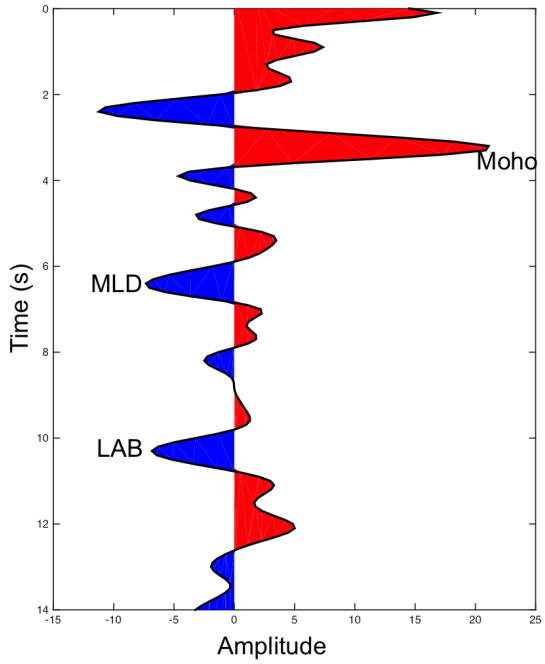

Figure 9.1: *Stack of all 486 radial RFs generated for station HRV. Time zero indicates the arrival of the direct P-wave. Three boundaries have been identified within 15 seconds after the primary arrival; the Moho (3.32s), the MLD (6.50s), and the LAB (10.40s).*

9.1.2 Harmonic decomposition

A harmonic decomposition of the signal is carried out to determine the contribution of 2π symmetry (dip or a steeply plunging fast axis) and π symmetry (azimuthal anisotropy) (Figure 9.3). At 6.5s there is hardly any contribution of either 2π or π symmetry. However, there are peaks on both sides of the picked MLD on the higher order harmonics. At 4.5s, there is a signal with a dominant positive pulse for $k{=}2_{EW}$ (π symmetry), and at 7.3s there is another positive signal, which exhibits a dominant 2π symmetry for $k{=}1_{EW}$. The unmodeled part of the signal resulting from 3D-complexities is not strong between 6s and 8s, with the exception of a weak signal at 6.5s (Figure 9.3).

The observation that the anisotropic signal resides deeper than 6.5s is supported by an investigation of the individual components (Figure 9.2). The offset between the constant backazimuthal harmonic and higher order harmonics was first considered to be a result of incomplete backazimuthal coverage of RFs, as 216 backazimuths are not represented when the RFs are binned in 1°bins. By increasing the bin width to 10° there are only five empty bins, but the time difference between peaks in the harmonic decomposition remains unchanged.

For k=1, the dominant sum of the NS and EW components around assumed MLD depths reside at 7.3s, with a dominant negative peak in k=1_{NS}. The dominant peak for k=2 is mapped at 7.1 s, primarily dominated by a positive peak on the EW component. The amplitude ratio k=1/k=2 is 0.63.

The peak at 4.5s is quite strong in the summed harmonics (Figure 9.2), but as it is not particularly strong on k=0 or the radial stack, and too deep to be an interface which would cause a reverberation at MLD depths (see electronic supplement in Rychert et al. (2005)). The peak at 4.5s will therefore not be considered an important feature in this thesis.

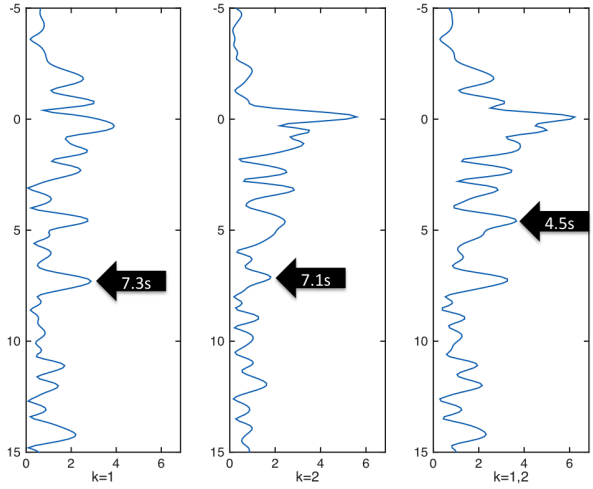

Figure 9.2: *Absolute sum of k=1, k=2, and the total of these (k=1,2) highlights the time at which energy arising from dip or anisotropy is strongest beneath HRV. Black arrows indicate features which are discussed in the text.*

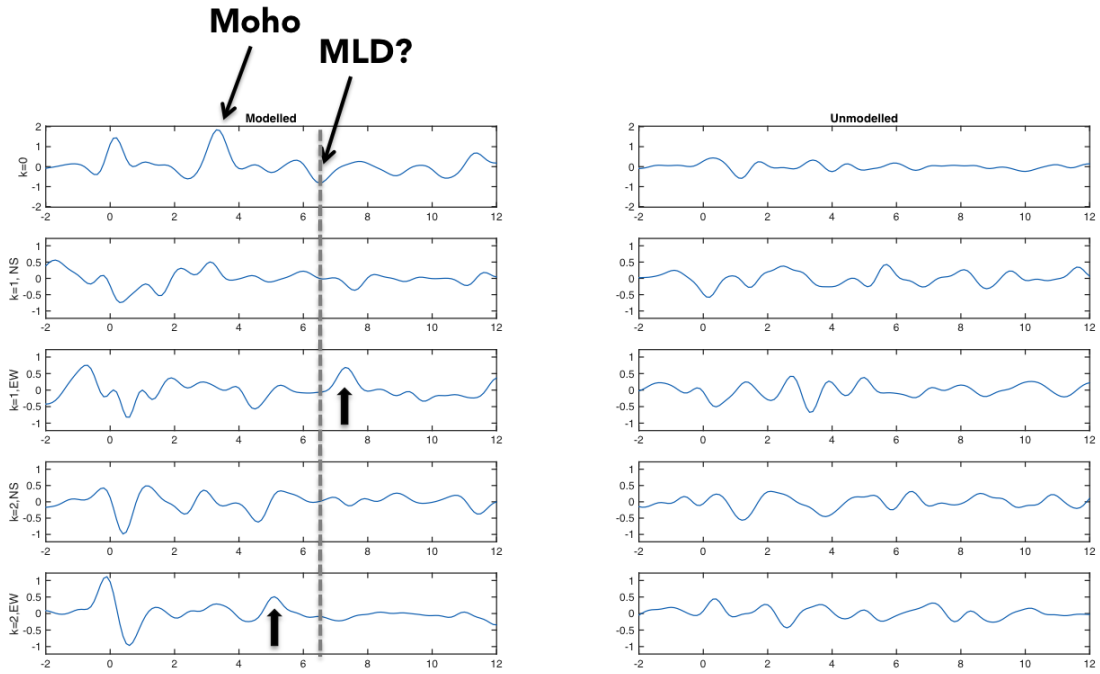

Figure 9.3: *Harmonic decomposition of RFs for station HRV. The dashed line indicates the time where the MLD was picked on the radial stack (6.5s), and black arrows point to signals on the higher order harmonics on both sides of the proposed MLD.*

9.1.3 Transverse component

The amplitudes at 7.3s are extracted from the transverse component to map the backazimuths of polarity reversals. The clearest reversal is found at 265° backazimuth, where the polarity changes from negative to positive (Figure 9.4). The polarity also changes somewhere between 85° and 160° backazimuth. As this range coincides with the gaps in backazimuthal coverage, the exact point of reversal between 85° and 160° can not be determined based on the transverse component.

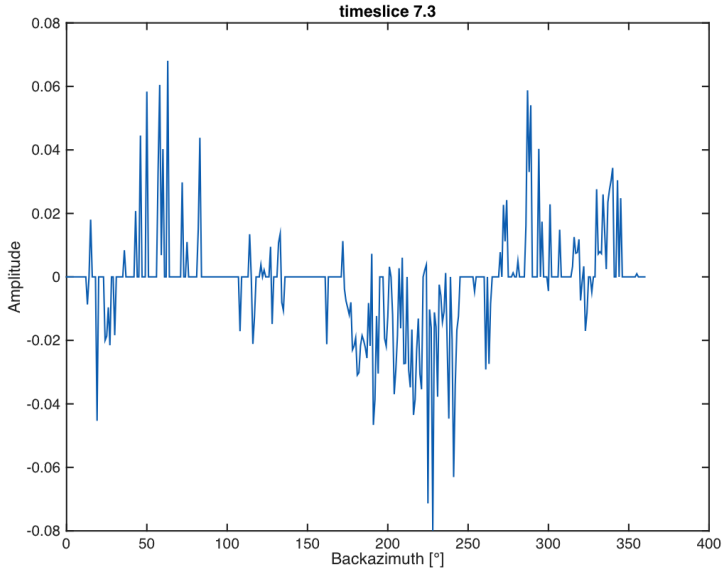

Figure 9.4: *Amplitudes along the backazimuthal range for the transverse component (station HRV) at 7.3s, binned in 1° bins, and bandpass filtered at 0.01-1.1 Hz. The dominant change in polarity follows a 2π symmetry.*

9.2 Fitting synthetic data to HRV

Assuming that the signal around 6.5s in the radial stack represents a property change with depth, I generate the simplest model that can reproduce the data from HRV through a systematic grid search of parameters investigated in Chapter 8. The number of models tested in this process exceeds what would be appropriate for an appendix, so Appendix C only contains the best results for the different tests described.

9.2.1 Isotropy

I first generate an isotropic velocity model based on the results of Rychert et al. (2005). The preferred isotropic model is obtained by fitting the radial component through gradual alterations of V_P, V_S and density. Starting

with a crustal Vp of 6405 m/s and V_P/V_S ratio of 1.69, the velocities are altered to match times and amplitudes of peaks/troughs on the radial stack. Vp/Vs ratios ranging from 1.70 to 2.2 are tested for the layers beneath the Moho, through a gradual increase of 0.1 in each iteration. Densities were varied between 3100 kg/m^3 and 3300 kg/m^3, but these changes in density did not significantly alter the results. This was also noted by Rychert et al. (2005). A purely isotropic model with horizontal layering does not generate any signal on the transverse component or the modeled harmonics, requiring the presence of anisotropy or dip beneath HRV. By a simultaneous fitting of the radial stack and the summed harmonics, I find that the HRV data cannot be reproduced with an isotropic velocity model with a dipping MLD, as dip alone does not provide sufficient energy on the k=2 component (See Appendix B.1.3).

As no satisfactory isotropic solution is obtained, I add anisotropic properties to the model in order to generate a more fitting lithospheric model.

9.2.2 Anisotropy

Horizontal fast axis

I start by investigating the simplest anisotropic model, that of horizontal anisotropy, before increasing the complexity. When testing for anisotropic layers I focus on the MLD signal. Due to the coarse layering, the introduction of anisotropy above and below the MLD may cause strong anisotropic signals at the Moho and LAB, which are not observed in the data. These strong signals will be disregarded for the time being, but their implications will be discussed in the next chapter.

From an investigation of the subsurface model proposed by Yuan and Romanowicz (2010), I find that changes in azimuthal anisotropy alone cannot explain the observed signal at MLD depths at HRV (Figure 9.5). Azimuths of fast axes were systematically tested through a grid search of 45°, but models

containing only azimuthal anisotropy produce very limited signal on k=1.

The strongest signal in the harmonic decomposition at HRV is found on k=1, which arises from the presence of dip or a plunging fast axis. I therefore seek a lithospheric model where the fast axis is either plunging with more than 45°, or one where horizontal anisotropy is accompanied by a dipping interface. As the exact backazimuth of reversal between 85° and 160° is not known, I initially assume that the polarity bands are equal. This means that I investigate two main possibilities: 1) A plunging fast axis of anisotropy with no dipping boundary and 2) Horizontal anisotropy accompanied by a dipping boundary. If this does not provide a satisfactory model, I will investigate models containing both a plunging fast axis and a dipping boundary.

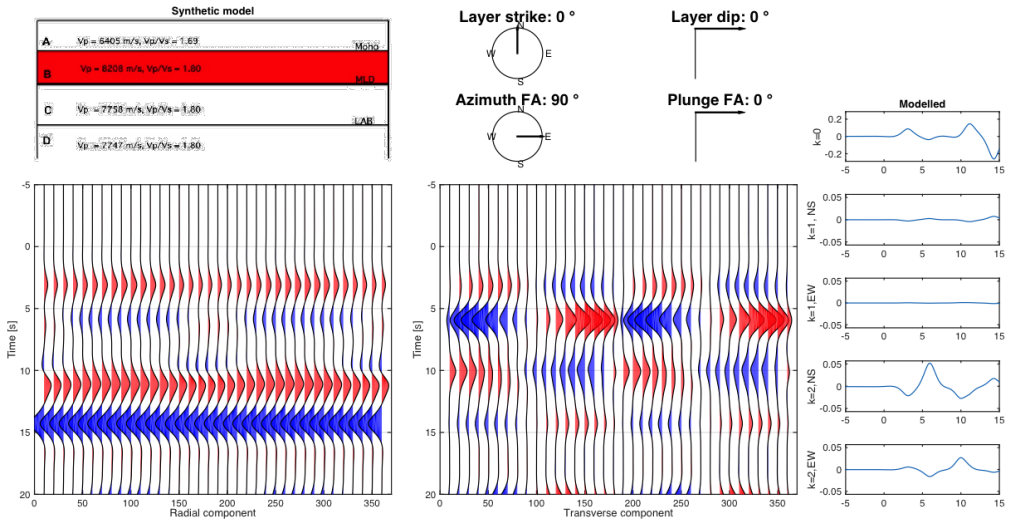

Figure 9.5: *Radial and transverse RFs for a synthetic model based on the findings of azimuthal anisotropy from Yuan and Romanowicz (2010). Properties of the red layer in the model are indicated. The third layer has azimuthal anisotropy with a fast axis towards the north, while the half-space has azimuthal anisotropy with a fast axis of 45°.*

Horizontal anisotropy and dip

The dip of a boundary at MLD depths is modeled ranging from 1° to 15° (Table 9.1). At 5° dip, the synthetic radial stack fits the radial stack from HRV quite well (Figure 9.6, left). However, a dip of 5° does not produce sufficient energy on the k=1 component (Figure 9.7). The 5° dip introduces a 0.3s time shift between k=0 and higher order harmonics, which is insufficient to explain the delay at HRV. Increasing the dip to 15° increases the signal on k=1, but not enough to explain k=1 at HRV. The increased dip does not increase the time shift, and provides a poorer fit to the radial. Dip angles exceeding 15° are therefore not investigated for this scenario.

Table 9.1: *Model properties of horizontal anisotropy and dip tests. Y/N indicates the presence of anisotropy in the layer.*

Thickness (m)	ρ (kg/m^3)	α (m/s)	β (m/s)	iso	%P	%S	Azimuth (°)	Plunge (°)	Strike (°)	Dip (°)
29500	2600	6405	3790	N	-	-	-	-	-	-
36500	3200	8208	4557	Y	8.0	8.0	45	0	-	-
33000	3200	8202	4557	Y	3.0	3.0	135	0	0	1-15
0	3200	7747	4303	Y	3.0	3.0	45	0	-	-

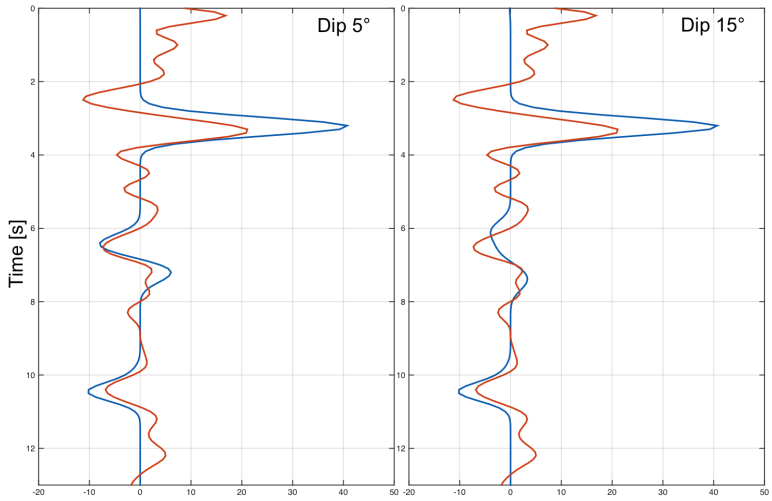

Figure 9.6: *Radial stack of horizontal anisotropic models with a dipping MLD. Table 9.1 contains the details of the models, shown in the figure as blue lines. The red lines represents the stacked radial of HRV from Figure 9.1.*

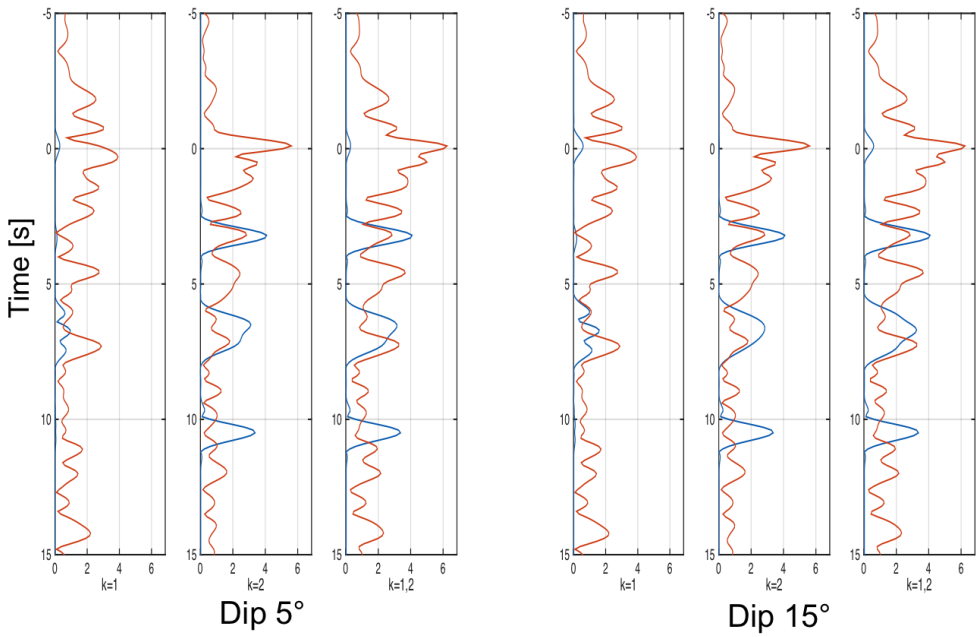

Figure 9.7: *Summed higher order harmonics for horizontal anisotropic models with a dipping MLD. Table 9.1 contains the model details. The synthetic models are indicated in blue, and the HRV data in red.*

Plunging fast axis

By adding a plunging axis of anisotropy to the model in Figure 9.5, I note a possible explanation for the delay between k=0 and higher order harmonics that does not depend on insufficient backazimuthal coverage. The offset can arise when a layer of horizontal anisotropy is underlaid by a layer with a plunging fast axis of anisotropy. Figure 9.8 shows a section of radial RFs and the resulting stack of RFs for a three layer model overlying a half-space (see Table 9.2 for details). Travel time varies with backazimuth with the introduction of anisotropic layers, and anisotropy introduces a phase shift in the radial component which causes the total anisotropic signal at the lower boundary of the upper layer to be weak. Due to these effects, the radial stack displays mainly one negative pulse, masking the deeper signal.

In Figure 9.8, the main negative peak is at 6.6 s, while the positive peak

below is at 7.1 s. The dashed line in the plot marks 7.3 s, the dominant k=1 peak at HRV. This would also explain the two peaks slightly offset in Figure 9.2, as they represent two different signals arising from materials with different anisotropic properties. For this reason, I aim to match the peak in the radial component at 6.5 s to the peaks in the harmonic decomposition at 7.1 s and 7.3 s, assuming that the shift between the two displays arises from this phenomenon.

Table 9.2: *Simple model of the lithosphere beneath HRV utilizing depths from Rondenay et al. (2017), velocities and densities from Rychert et al. (2005), and anisotropic trends from the regional study by Yuan and Romanowicz (2010). The magnitude of anisotropy is chosen arbitrary within estimates suggested by Selway et al. (2015).*

Layer	**Thickness [m]**	**Vp [m/s]**	**Vs [m/s]**	ρ $[kg/m^3]$	**%**	**Trend**[°]	**Plunge**[°]
1	28000	6405	3790	2600	0	-	-
2	38000	8208	4557	3300	5.5	90	0
3	29000	7758	4310	3200	5.5	0	50
4	-	7747	4303	3200	5.5	45	0

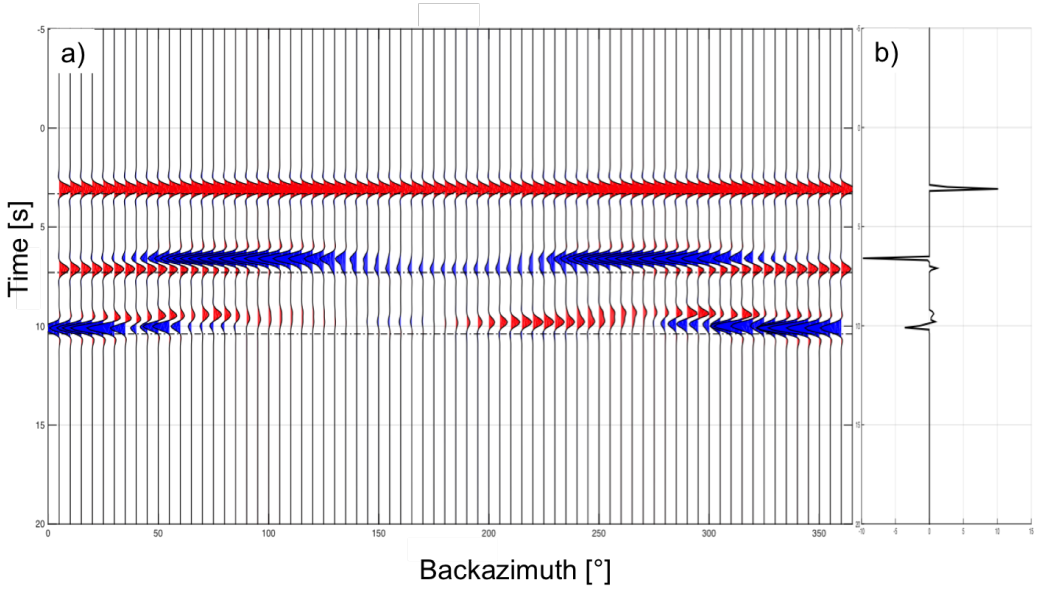

Figure 9.8: *a) Full backazimuthal range of the radial component, for an anisotropic model of the lithosphere beneath HRV. b) Stack of the individual radial RFs. This figure illustrates a possible explanation to the offset between the MLD signal for k=0 and higher order harmonics. The curved signal on the radial component masks the deeper signal, providing mainly one negative pulse in the stacked radial, similar to what is observed in Figure 9.1. See Table 9.2 for details about the model.*

In the process of mapping the time shift which arises from two layers with different types of anisotropy across a boundary, I noted that in order to have such a shift, the layer of horizontal anisotropy must be shallower than the layer of plunging anisotropy (Appendix C.2). This also matches the observation that the k=1 signal is slightly deeper than the k=2 signal at HRV. If the layers are reversed (the plunging anisotropy is overlaying horizontal anisotropy), k=1 becomes the shallower signal.

Based on these findings, I seek the simplest possible model containing anisotropy (horizontal overlaying plunging) that can reproduce the radial and transverse sections of RFs, along with a harmonic decomposition of the synthetic signal similar to what is observed at HRV. I first recreate the observed data without adding a dipping boundary, as this adds increased complexity to the model.

Final model

The radial stack is easy to reproduce with a velocity reduction across the MLD, but to simultaneously obtain good results for the time offset between k=0 and higher order harmonics proved difficult. The three best models with velocity reduction across the MLD are found in Appendix C.1[1].

Once anisotropy is introduced, I find that it is easier to match the radial component with a constant reference velocity across the MLD, with varying anisotropic properties on either side. By removing the velocity reduction at MLD depths, the amplitude of the radial stack can be fitted through a gradual alteration of anisotropic magnitude. The magnitude of anisotropy also determines the offset between k=0 and higher order harmonics. A regular grid search from 1% to 10% anisotropic magnitude result in best fit for the radial stack and offset between k=0 and higher order harmonics if the anisotropy is 8% in the upper layer, and 3% in the lower layer. Anisotropic magnitude of the half-space representing the asthenosphere is set to 3%, but the resulting peak here is too strong and should be investigated further.

Anisotropic trend in the upper layer was determined through a systematic grid search of 45° azimuth, resulting in the best fit for a fast axis trending towards NE (45°). The grid was then reduced to a search of 5° azimuth, still resulting in the best match for a 45° fast axis[2]. Due to symmetry of a horizontal fast axis, the fast direction is along the NE-SW axis, meaning that the fast axis of 45° could also have been indicated as 225°.

From Table 8.1 I find that polarities of the k=1 signal (negative k=1_{NS} and positive k=1_{EW}) correspond to a fast axis azimuth of 135°, in case of an anisotropic half-space overlaid by an isotropic layer. Through systematic comparison with other azimuths (45° grid search) I find that an azimuth of 135° is a good fit to the real data, regardless of the FA azimuth in the layer above.

[1] I initially aimed to fit the stacked radial and the summed harmonics, so these models have not been fitted for fast axis azimuth.

[2] Variations around 45° can be found in Appendix C.3

The degree of plunge was modeled using the relative amplitude strength between k=1 and k=2 in the summed harmonic stack. Through a gradual increase of 5° of the plunge angle (starting at 45°), I find a good fit between k=1 and k=2 for a fast axis plunging at 60°.

In order to determine whether these two parameters are well constrained, I do a 1/2° grid search around 60° plunge and 135° azimuth of the fast axis (respectively), according to the method described in Das and Nolet (1995).

The radial stack is investigated by a comparison of the maximum amplitude between 6s and 7s for real data and synthetic models, as the main pulse on the radial component is picked to 6.5s. There is no differences in time of maximum peak for any of the models, all test models are off by 0.1s compared to HRV. The difference in amplitude is best constrained by the plunge angle, with closest result to HRV for a plunge angle of 63° for the values tested (Figure 9.9). However, a minimum cannot be determined based on this grid search alone, as the values could decrease further with increasing plunge angle. I therefore check the harmonic decomposition to see if the same trend appears there, and if so - increase the grid.

When all individual components of the harmonic decompositions are considered, the test models show little variation with plunge or azimuth. Variations in the full harmonic decompositions for different azimuths of the FA, with a 60° plunge are displayed in Appendix C.4. The sum of higher order harmonics is therefore used for comparison between HRV data and test models. The amplitude difference between summed higher order harmonics and real HRV data (with a maximum peak between 6.9s and 7.5s) is displayed in Figure 9.10. The range is different than for Figure 9.9 as the maximum signals are located at 7.1/7.3s in the summed harmonic decomposition for HRV (Figure 9.2). Though the trend in Figure 9.10 is less clear than for the radial display, the main constraint on the harmonic sum also seem to be the plunging angle. For the harmonic decomposition, the smallest difference in amplitude between real and synthetic data is found for a plunge angle of 57°.

As the two grids in figures 9.9 and 9.10 point to different optimal models, these results cannot be used to constrain the exact plunge angle and azimuth in the lower layer. If such plots were generated for all the individual components they would be more useful, but as the summed harmonic does not take into account the signal on individual components it is not an ideal estimate of the best fit. Full range amplitude grids for all components is beyond the scope of this thesis, and the values selected are therefore constrained by observations from HRV. From visual interpretation I found that the best fit for synthetic models is obtained around 60° plunge (better at 60° than 55° and 65°), and 135° azimuth. I therefore use the middle values (60° plunge and 135° azimuth) in the final lithospheric model beneath HRV.

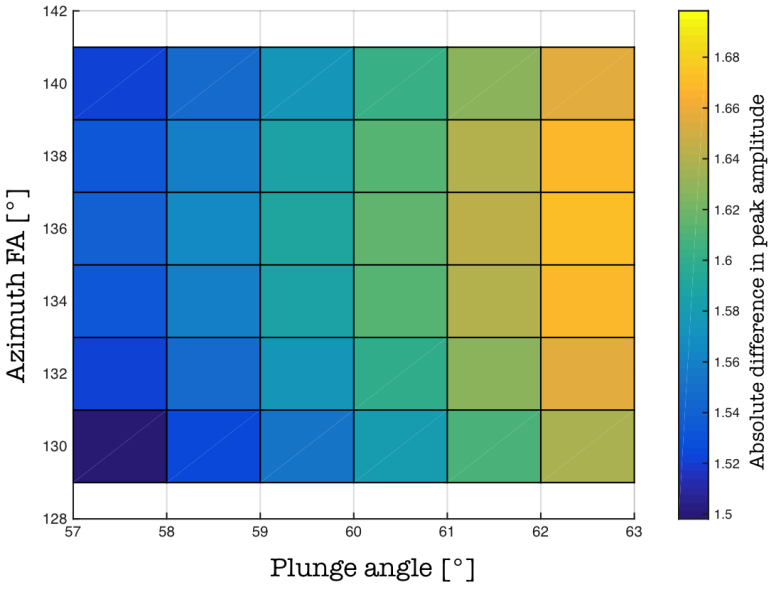

Figure 9.9: *Amplitude difference (in absolute terms) between maximum peak of synthetic model and HRV for the radial component in a time window of 6.0s to 7.0s.*

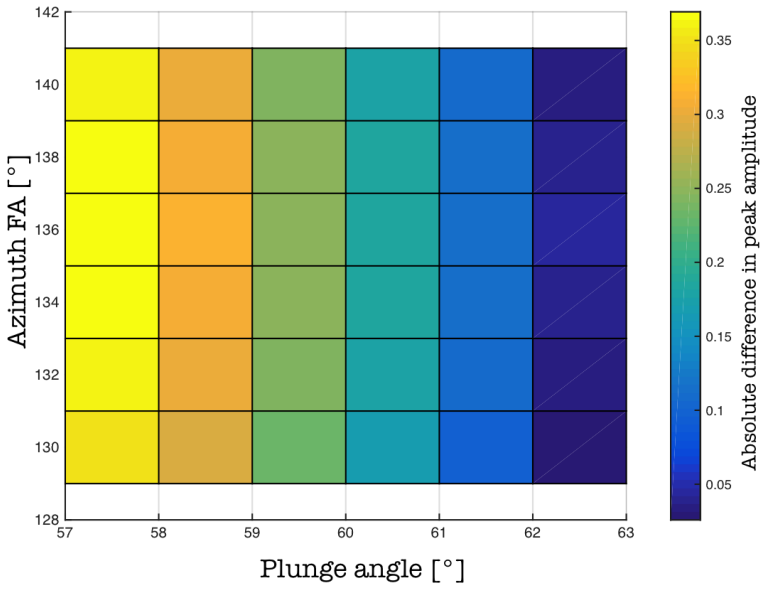

Figure 9.10: *Amplitude difference (in absolute terms) between maximum peak of synthetic model and HRV for k=1,2 in a time window of 6.9s to 7.5s.*

The final model is displayed by a radial stack (Figure 9.11), harmonic decomposition (Figure 9.12), summed harmonic decomposition (Figure 9.13) and transverse component (full backazimuthal range in Figure 9.14 and amplitudes along the dashed line in Figure 9.15). The Moho is modeled to be at 29.5km depth, the MLD at 66km, and the LAB at 99km. A summary of properties of the final model can be found in Table 9.3.

Table 9.3: *Properties of the final model representing the lithosphere beneath HRV. Mag denotes the percentage anisotropy (difference between maximum and minimum seismic velocity).*

Layer	**Thickness** [m]	**Vp** [m/s]	**Vs** [m/s]	ρ [kg/m^3]	**Mag** [%]	**Trend** [°]	**Plunge** [°]
1	29500	6405	3790	2600	0	-	-
2	36500	8208	4557	3200	8.0	45/225	0
3	33000	8208	4557	3200	3.0	135	60
4	-	7747	4303	3200	3.0	45/225	0

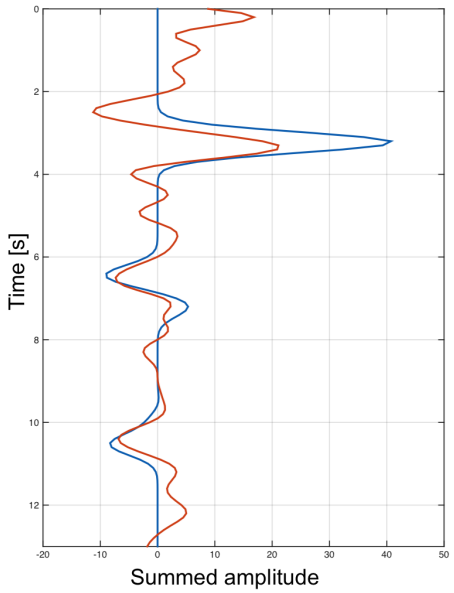

Figure 9.11: *Comparison between synthetic and HRV stacked radial. The final synthetic model is indicated with a blue line, and HRV data by the red line (From Figure 9.1).*

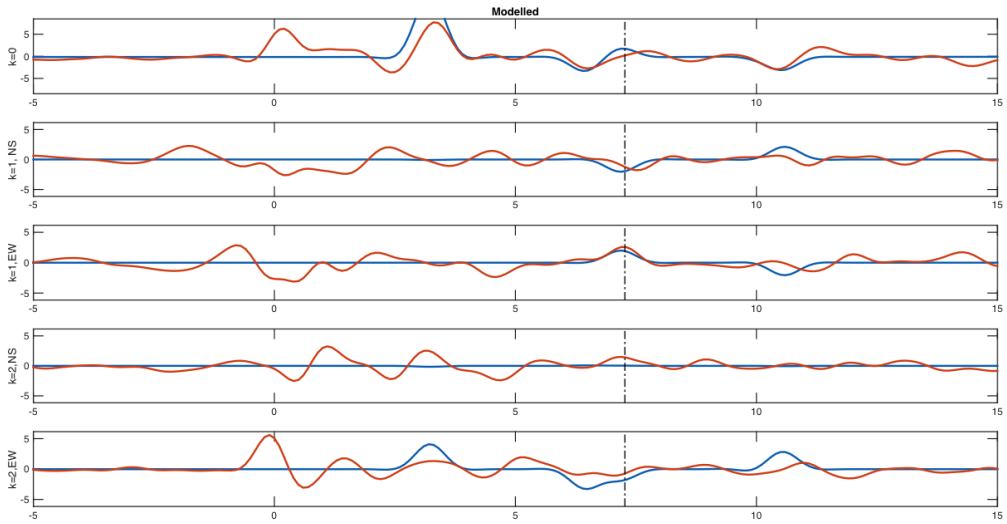

Figure 9.12: *Individual components of the harmonic decomposition for the final synthetic model (blue) compared to HRV (red). Dashed line indicates 7.3s, corresponding to the strong signal in the k=1$_{EW}$ component in Figure 9.3.*

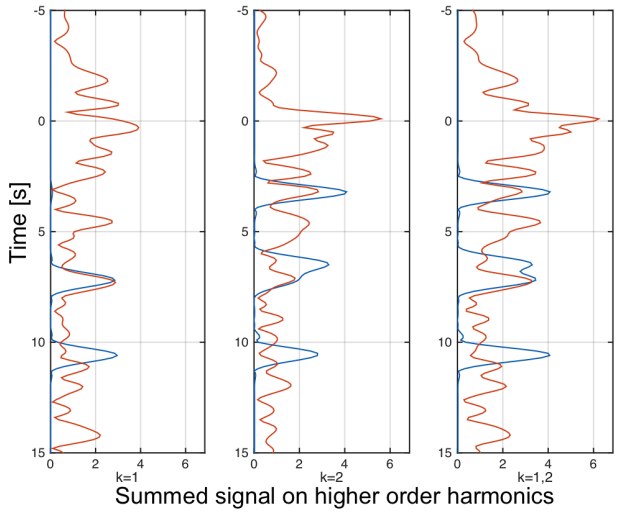

Figure 9.13: *The summed harmonic decomposition of the final synthetic model (blue) compared to HRV (red). Note that the synthetic signals at 6.5s and around LAB depths are too strong compared to HRV.*

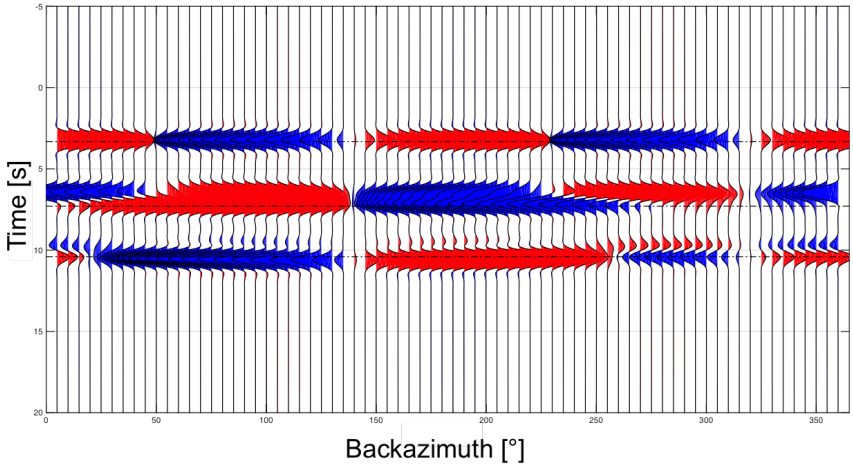

Figure 9.14: *Transverse component of the final synthetic model, displaying the change from π to 2π symmetry occuring over the MLD. Dashed lines indicates (from top to bottom) the picked Moho, MLD, and LAB. Due to simple layering, the Moho and the LAB also exhibit strong anisotropic signals.*

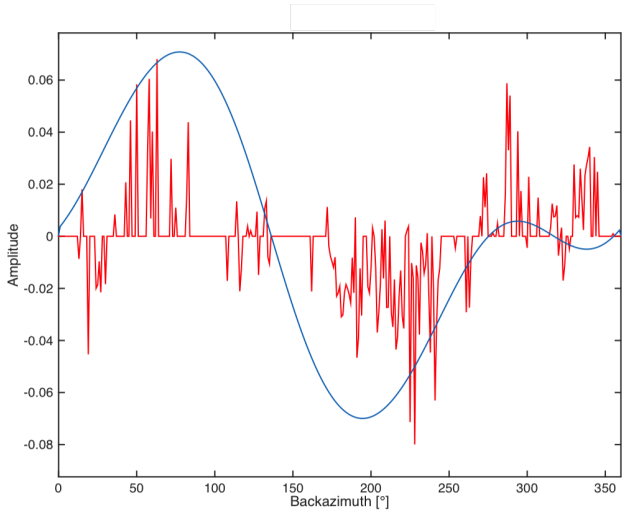

Figure 9.15: *Amplitude display of the transverse component for HRV (red) and the final synthetic model (blue) at time 7.3s. Both signals exhibit mainly 2π symmetry, and the synthetic model is matching HRV data quite well with exception of the backazimuthal range of 325-350°.*

9.3 Regional profiles

Radial RFs and the summed harmonic decomposition for k=1,2 are shown in Figure 9.16 for a NW-SE trending profile. The Moho increases in depth from the SE towards the NW (indicated by blue line in Figure 9.16). The interpretation is made on the radial RFs, and added to the harmonic decomposition at the same times. The signal observed around 6.5s for HRV is hard to trace with any certainty in either direction on the stacked radial RFs, but some possible interpretations are added with different dashed green lines. The signal at 7.3s on the harmonic decomposition can be traced to the two surrounding stations, gradually decreasing in signal strength towards NW. Two interpretations are indicated with dashed green lines in the harmonic sum plot. One thing to keep in mind is that there are large variations in backazimuthal coverage between stations which can affect, in particular, the harmonic decomposition (Figure 9.17).

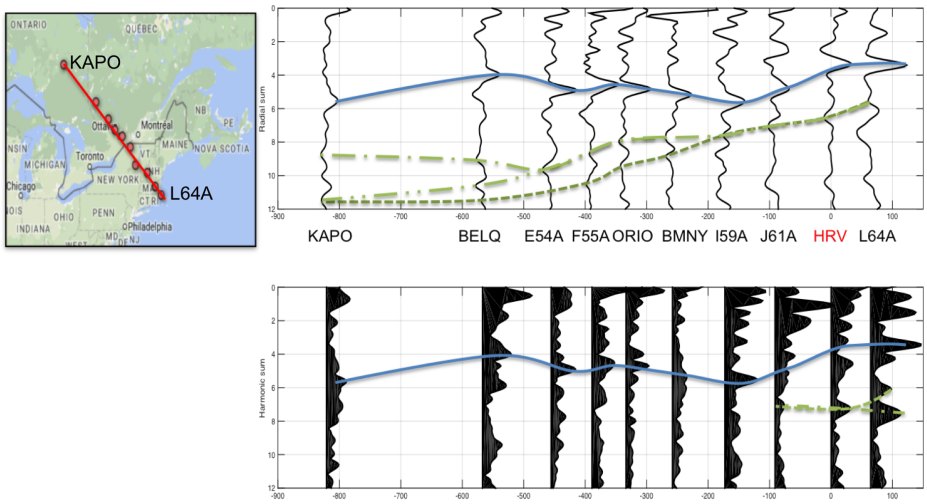

Figure 9.16: *Radial stack and summed harmonic decomposition for 10 stations in eastern North America. From NW to SE: CN KAPO, PO BELQ, TA E54A, TA F55A, PO ORIO, LD BMNY, TA I59A, TA J61A, IU HRV, and TA L64A. The blue line indicate the interpreted Moho, and dashed green lines indicates different interpretations of an MLD signal.*

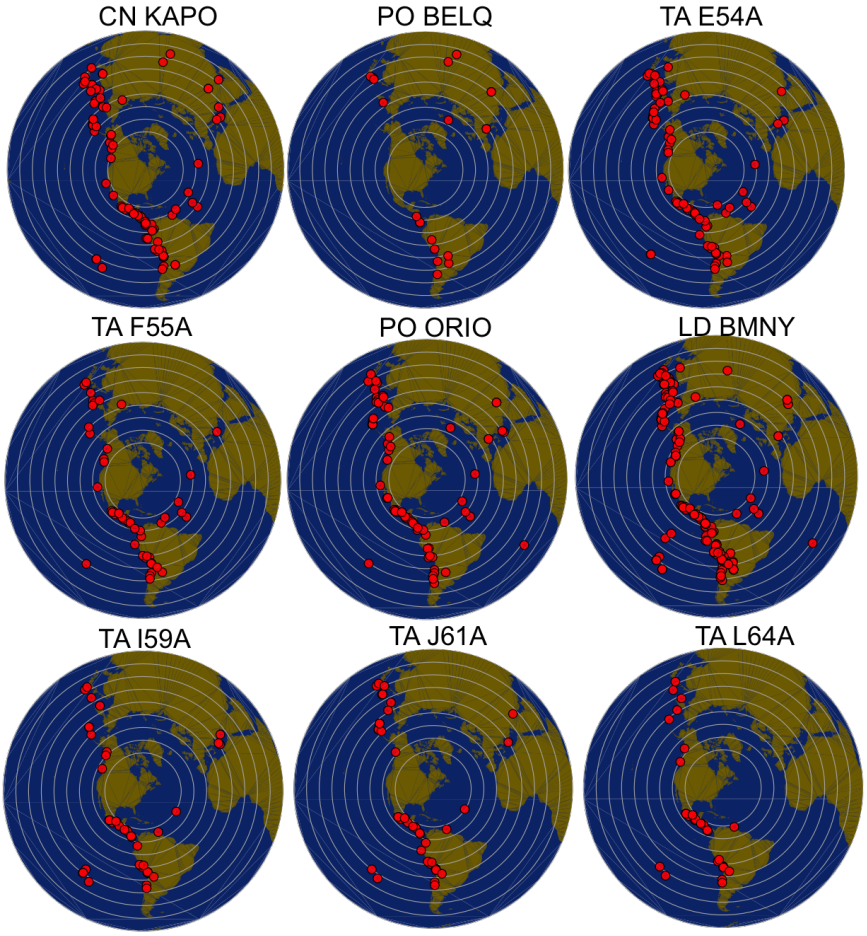

Figure 9.17: *Distribution of RFs for the 9 stations (not including HRV) in the regional profile. Network and station names are indicated above each plot.*

For a profile following approximately the low velocity corridor noted in Rondenay et al. (2000), the proposed MLD signal can be traced on the harmonic decomposition (Figure 9.18). When the interpretation is added to the radial stack, the interpreted line intersect the radial RFs at peaks with both negative and positive polarities. The time of maximum signal strength in Figure 9.18 varies from 9.5s in the N(W) to 7.3s in the S(E).

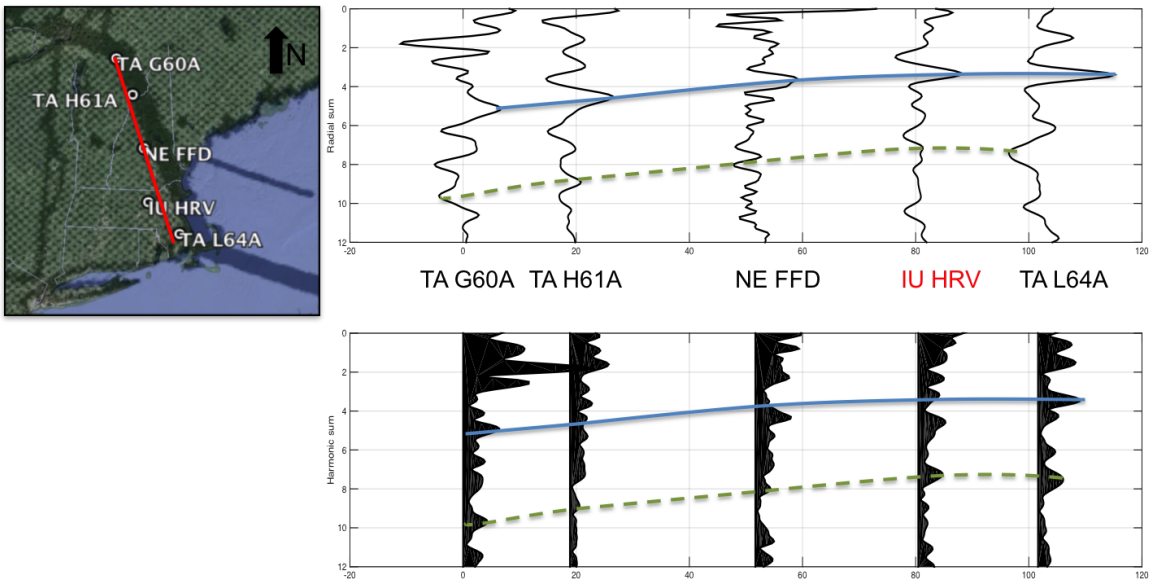

Figure 9.18: *Radial stack and summed harmonic decomposition for 5 stations in eastern North America. The blue line indicates the interpreted Moho, and the green line is the interpreted MLD from summed higher order harmonics at HRV. The black solid line in the map represents the low velocity corridor from Rondenay et al. (2000).*

Chapter 10

Discussion

This chapter discusses the lithospheric model generated for HRV and observations from regional profiles. An interpretation of the obtained model parameters is provided, along with future proposed research projects for continued investigation of lithospheric discontinuities in eastern North America.

10.1 Seismological evaluation of the results

10.1.1 The MLD

The sum of the synthetic radial RFs is a sufficiently good match for the real data around the MLD. The synthetic MLD has a local minimum 0.7s prior to the HRV data, with 20% stronger amplitude. The positive peak at 7.2 s in the radial is 58% stronger in the synthetic model than for HRV data, suggesting that the magnitude of anisotropy is too strong in the layer beneath the MLD. Times picked for the Moho, MLD and LAB correspond well to the findings of Yuan and Levin (2014). The modeled MLD depth is off by ~ 5 km compared to the findings of Rychert et al. (2005), which I attribute to their inclusion of a velocity reduction across the MLD.

The harmonic decomposition shows a good match for all components except

k=2_{NS} (Figure 9.12). The misfit in the k=2_{NS} component arises from the selected FA direction in the layer above the MLD (See Appendix C). A fast axis of 45° azimuth was selected, as it represents the best fit for both components k=$1_{NS,EW}$. The k=2_{NS} component is better matched with a 30° azimuth FA, but by using a 30° azimuth I introduce a peak at 6.5s which is not present in the real data. To avoid the introduction of additional energy in the harmonic decomposition I therefore generate the synthetic model with a 45°azimuth fast axis.

The summed harmonic decomposition provides a good match with the proposed MLD pulse, but compared to HRV data its signal strength at 6.5s is too strong (Figure 9.13). As the peaks at 7.1s and 7.3s fit the real data well, I attribute the large amplitude at 6.5s in part to the sharp change in anisotropy introduced by the assumption that properties change instantly across the boundary (no boundary thickness). The signal could also be enhanced by the abrupt change from horizontal to plunging anisotropy in the synthetic model. A change in the fast axis from semi-horizontal to plunging around the MLD was reported by Wirth and Long (2014), so the possibility that the upper layer has some degree of plunge should therefore be investigated further, to test its effect on signal at 6.5s.

Polarity reversals extracted from the transverse component at 7.3s occur at 140° and 280° in the final synthetic model (Figure 9.14). This matches the HRV data, with the exception of the backazimuthal range from 325° to 350°. As this is a comparison between idealized synthetic data and noisy real data, I suggest that the difference in the backazimuthal range of 325° to 350° arise from noise.

10.1.2 Other boundaries

There is a negative pulse just above the Moho in the summed radial RF at HRV. This negative signal is reduced with different deconvolution schemes, so it can be a processing artifact (E-supplement Rondenay et al. (2017)).

However, the feature can be reproduced through fitting of the summed radial by introducing a velocity reduction of 3.7% at a depth of 23km (Appendix C.1). Such a velocity reduction coincides well with the low velocity feature mapped by Liang and Langston (2009) in North America. Even though this boundary might exist, a low velocity layer at 23km depth produces multiples below the MLD (see Appendix C, and supplement from Rychert et al. (2005)), making the discussion about its existence beyond the scope of this thesis.

The amplitude of the synthetic RF is too strong at the Moho (Figure 9.11). The Moho is not seen as a strongly anisotropic boundary in the harmonic decomposition, but as this simplified model only contains one layer between the Moho and the MLD, these two boundaries effectively have the same anisotropic properties. As this adds extra energy on the radial component, I suggest that the amplitude difference at the Moho is introduced by the single layer simplification. To test this, I generate a model containing a boundary at 4.5s, and reduce the anisotropy in the layer beneath the Moho to 2% (Appendix C). The introduction of an extra boundary results in a synthetic model which better matches the amplitude of the HRV Moho. However, including an extra boundary in the final model requires a more thorough study of its existence and potential anisotropic properties. The boundary at 4.5s is therefore not included in the final model.

The signal representing the LAB is too strong in the summed harmonic stack, and has an insufficient time delay between k=0 and higher order harmonics. The anisotropic fast axis beneath the LAB was kept horizontal with azimuth 45°/225°, as inferred from APM (Yuan and Romanowicz, 2010). However, this simplification might not be valid for the study area as it is situated on the continental edge, where the mantle flow pattern may deviate from the direction of APM, and the angle of the fast axis might not be horizontal (Fouch et al., 2000). This is supported by Yuan and Levin (2014), who find that the polarity reversals on the transverse component has a 2π symmetry, interpreted as a plunging fast axis in the asthenosphere beneath HRV.

The presence of 3D-complexity/heterogeneity was noted at 6.5s in the k=2_{NS} component in the harmonic decomposition. It is therefore a possibility that lateral variations contribute to the signal. However, boundaries beneath HRV have been inferred as anisotropic by both receiver function investigations and shear wave splitting studies. The signal is therefore not expected to arise solely from 3-D complexities. The contribution of heterogeneties should be investigated further using surface waves with higher lateral resolution, or through thorough investigations of unmodeled harmonics for seismic stations in proximity of HRV.

10.1.3 HRV - summary

Overall, the model seem to match the observed data rather well. The observed splitting times of $\sim$ 1s at HRV (Yuan and Levin, 2014; Fouch et al., 2000) is by rule of thumb interpreted as 100 km of anisotropic material with anisotropic magnitude of $\sim$ 4% (Silver, 1996). Here the lithospheric thickness is estimated to be 99 km, with an isotropic crust of 29.5 km. The overall contribution from a strongly anisotropic upper lithospheric layer (8%) and a less anisotropic lower layer (3%), along with an anisotropic sub-lithospheric mantle (>3%), provides an acceptable average anisotropy compared to the observed splitting time at HRV.

The fast axis at station HRV was investigated through shear wave splitting by Yuan and Levin (2014). They find that the dominant FA direction is 89°, but also note a smaller mode around 130°. When modeling two layers of anisotropy, their best model suggests a FA with azimuth in the range 120-145° above the LAB, and $\sim$ 50° below the LAB. This sub-lithospheric anisotropy is found to have a fast axis plunging with approximately 30°. The lithospheric anisotropy layer is approximated to have a gentle plunge angle. Their inversion does not test the possibility of 3 anisotropic layers, so I explain the differences between my findings and their results by the one-layer anisotropy assumption within the lithosphere.

10.1.4 Regional findings

The depth of the Moho changes along the profile in Figure 9.16, with a maximum depth around station TA I59A. Station I59A is located in the Adirondack mountains, part of the Grenville province (Wiener et al., 1984). The Grenville province is found to be the province in eastern North America with the thickest crust, supporting the interpretations of the deepening Moho in Figure 9.16 (Rondenay et al., 2017; Levin et al., 2017).

In Figure 9.16, the peak at 7.3s can be traced to HRV's two nearest stations with a gradually weaker signal toward the NW. There are two proposed interpretations for the signal here, marked by dashed green lines. There is a possibility that the decrease in signal strength towards NW is a data artifact, arising from differences in backazimuthal coverage for the various stations. From Figure 9.17 it is found that the backazimuthal coverage of events is lowest at station PO BELQ, TA I59A, TA J61A and TA L64A. As the stations with strongest MLD signals around HRV are J61A and L64A, we must consider the possibility that these signals arise from incomplete backazimuthal coverage. However, it could also imply that the boundary has a less abrupt change in anisotropic properties towards the craton interior. To test this I generate a shorter profile which does not cross into the craton (Figure 9.18).

In the second profile (Figure 9.18), the proposed MLD signal can be traced from the harmonic decomposition in both directions away from HRV. When the interpretation from the harmonic decomposition is added to the radial RFs, the time of maximum peak in the harmonic decomposition does not correspond to a specific polarity on the radial component. This could indicate that there is an offset between k=0 and higher order harmonics, as is proposed for station HRV, or that anisotropy is causing the polarity of the summed radial RFs to depend on location/ backazimuthal coverage.

10.2 Tectonic interpretation

As the main goal of this thesis is to match the signal across the MLD, the nature of the crust and the sub-lithospheric mantle is not discussed in the tectonic interpretation. The crust is assumed to be isotropic, as reported by Levin et al. (1999). Beneath the LAB, the anisotropic fast axis is assumed to follow APM, resulting from drag induced fabric in the mantle from the lithosphere-asthenosphere coupling (e.g Yuan and Romanowicz (2010)). As the signal strength of the modeled LAB is too strong, the anisotropy in the asthenosphere might be less than 3%, indicating a weaker coupling.

The interpretations of anisotropic origin in the upper and lower lithospheric layers (Figure 10.1) are discussed separately in the following sections.

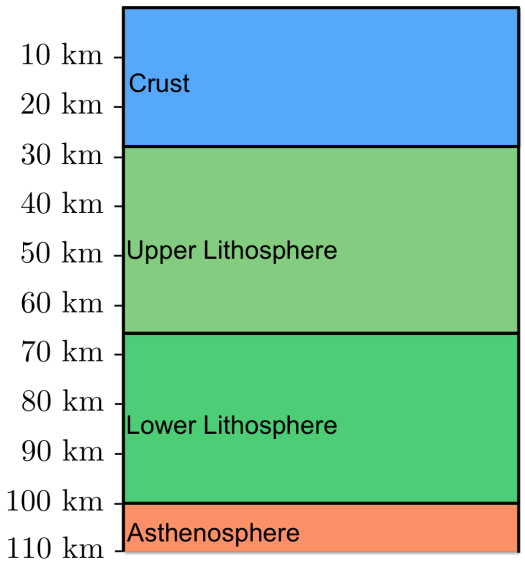

Figure 10.1: *Lithospheric model beneath station HRV.The two green layers represent two distinct types of anisotropy in a medium with constant base parameters.*

10.2.1 Upper lithosphere

The horizontal anisotropic pattern in the upper lithosphere follows the trend of the Appalachian orogen. Studies of anisotropy in present day compressional regions produce a fast axis sub-parallel to the orogen, inflicted upon the mantle lithosphere from flow related to transcurrent motion between the collisional plates [1] (Park and Levin, 2002). Anisotropy in the upper lithospheric layer could thereby be attributed to the formation of the Appalachians. This interpretation is supported by results from e.g. Levin et al. (1999) and Long et al. (2016).

Yuan and Romanowicz (2010) also suggest that the upper anisotropy follows surface geology, but propose that it could also result from welding of Archean continents. When considering only HRV it is difficult to make a conclusive interpretation about the origin of anisotropic fabric in the upper lithosphere, but as it follows surface geological trends I attribute it to "frozen-in" anisotropy from a large tectonic event. The comparable direction of the fast axis between upper lithosphere and asthenosphere was also noted by Yuan and Romanowicz (2010).

10.2.2 Lower lithosphere

Explaining the orientation of the lower lithospheric fabric proved more challenging. In a craton-wide study of North America by Yuan and Romanowicz (2010) the fast axis was found to be consistently towards the north, containing only shorter wavelength variations within. For a horizontal axis of anisotropy this deviation from N-S to a SE azimuth might not be too different, but when a plunging axis of anisotropy is introduced there are differences between a SE and NW fast axis which cause the fast axis found in this thesis to deviate from the result in Yuan and Romanowicz (2010) by 135°. Such

[1] It should be noted that there are some discussions about the origin of "frozen in" fabric (see e.g. Nicolas (1993)), but in most studies of SKS splitting the fast axis is assumed to be (sub) parallel to the orogen (Levin et al., 1999).

a difference could imply that the lower lithospheric signal observed at HRV coincides with one of these shorter wavelength variations, that the signal is affected by continental edge effects, or that the signal at HRV is of a different origin.

The implications of this last suggestion are twofold: either a localized process altered the lower lithospheric anisotropic fabric beneath HRV to deviate from the craton-wide observation, or the lower lithospheric layer does not extend outside the craton. To investigate these possibilities I return to the regional profiles, to see if they hold any clues. From Figure 9.16 it seems that the MLD signal disappears towards the craton, with decreasing signal strength in the radial and harmonic decomposition. In Figure 9.18 the signal strength of the MLD is more consistent, which could support the hypothesis that the specific MLD signal at HRV does not continue into the craton.

Without placing further constraints on whether the MLD beneath HRV is the same MLD as observed in the North American craton, I seek a process which could produce a change from horizontal "frozen in" anisotropy to a plunging axis of anisotropy at a rather consistent depth. An important question here is whether the anisotropic fabric in the lower layer is older or younger than that in the upper layer[2].

For upper layer anisotropic fabric arising from the Appalachian chain formation, I assume that the lower layer fabric is newer. This assumption is based on the fact that formation of the Appalachian orogen represents a poly-orogenic event with successive rifting and collisions, affecting the whole vertical extent of the lithosphere (Bradley, 1983, 1989). If the anisotropic fabric in the lower lithosphere were to arise from a previous compressional event, such as the Grenville formation, it would be difficult to explain how the Appalachian chain formation only affected the lithosphere down to a very consistent depth (the MLD) in the area. I thereby rule out the idea of an earlier tectonic event causing a "first frozen-in" fabric in the entire lithosphere, which was later overruled by the Appalachian formation down

[2]A third option, simultaneous formation of upper and lower layer anisotropy, is considered unlikely and therefore not investigated in this thesis

to MLD depths[3]. Based on these lines of thought I propose that the lower lithospheric fabric arises from a different mechanism than what produced fabric in the upper lithospheric layer.

A purely thermal solution of partial melt does not explain the orientation of the fast axis in the lower lithosphere. However, the problem could be linked to heating, as the fast axis direction in the lower layer coincides with the direction of the Great Meteor hotspot track through the study area (Figure 5.4) (Taylor and Fitzgerald, 2011).

The study area's passage over the hotspot postdates the Appalachian chain formation, implying that a hotspot induced fabric is newer than the fabric in the upper lithosphere. The proposed explanation of the abrupt change in anisotropy across the MLD is then that the fast axis in the entire subcrustal lithosphere was first oriented in the direction of the Appalachians by orogen parallel mantle flow, before the lower lithospheric fabric was reworked by a hot plume impinging on the base of the lithosphere. The idea is that hot mantle material reworked or partially melted the lower lithosphere without reaching the surface, thus conserving the anisotropic pattern in the upper lithospheric layer (Chu et al., 2013). This is illustrated in Figure 10.2, where gray circles/ellipses represent strain ellipses. The circles in the upper lithospheric layer represent cross section views of elongated ellipses in the horizontal plane. Such lithospheric plume deformations have been modeled by Yang and Leng (2014), and modeling results indicate that increased heat can, for even a relatively short period, rework the lower lithospheric material (Yang and Leng, 2014; Druken et al., 2013).

The vertical extent of reoriented fabric depends on the material's thermal conductivity (composition) and the amount of heat supplied from the plume (Davies, 1994). The mantle is assumed to be constituted in large part of olivine, but the influence of pyroxene strongly affects the anisotropic properties (Christensen, 1984). Only olivine orientation is considered in this thesis, but the contribution of other minerals should ideally be included for a more

[3]For the assumption that lithospheric fabric in the upper layer arise from the Appalachian chain formation

comprehensive study of mantle anisotropy. The heat supply is controlled by the excess temperature delivered by the plume, and the duration of heating (Yang and Leng, 2014; Davies, 1994). In case of an upwelling plume $\sim$ 100°C hotter than the surrounding material, a continental lithosphere is expected to thin substantially within 5-20 Myr (Davies, 1994). The base of the lithosphere in eastern North America is estimated to have been in contact with a potential plume for $\sim$5 Myr, which would be sufficiently short for the plume to affect only the lower part of the lithosphere, without reaching the surface (Rondenay et al., 2000; Yang and Leng, 2014). Assuming that the lower part of the lithosphere has undergone plastic deformation enabled by extra heating, the MLD could then represent the thermal boundary where olivine minerals could freely be reoriented by shear from coupling between the moving lithosphere and the asthenosphere[4].

According to the hotspot track indicated by a black solid line in Figure 5.4, the North American continent moved over the hotspot with direction towards NW. This would orient the strain ellipse in the NW-SE direction (the direction of flow), and from coupling between the lithosphere and the asthenosphere the strain ellipse would be plunging towards the SE (Figure 10.2). The exact plunging angle would be more challenging to obtain, but could be approximated from estimates of coupling, geotherms and plate velocity.

Figure 9.18 suggests that the MLD is dipping towards the craton, which is unexpected for a thermal solution to the MLD origin, as the assumption about equal material properties and a constant plate velocity should imply a constant thickness of this lower layer. However, Rychert et al. (2007) found that the LAB gets deeper towards the NW in the region, providing an explanation for the increased depth of the MLD.

[4]This could represent either reworked material or thermo-mechanical erosion and replacement of mantle material (Davies, 1994).

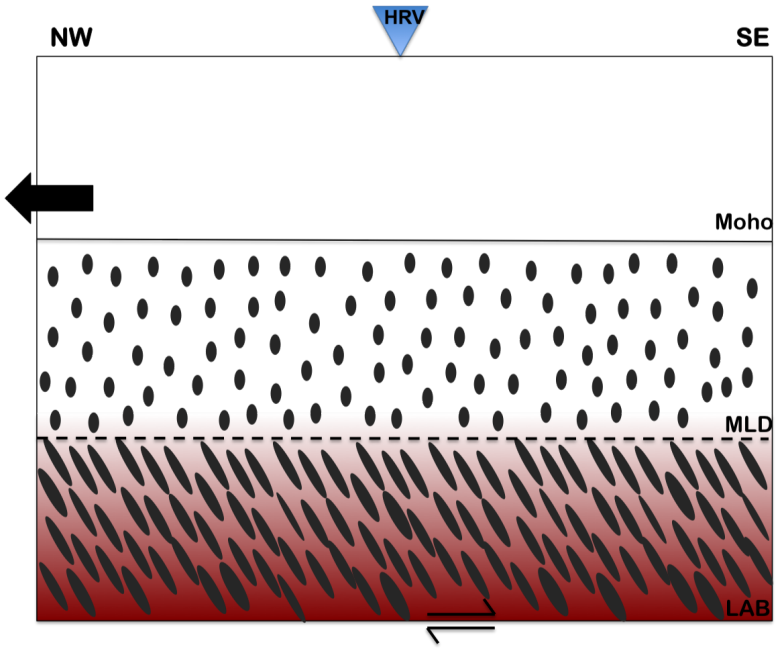

Figure 10.2: *Illustration of strain induced alignment of the olivine fast axis across the MLD, enabled by heating from a mantle plume. The fabric arising from long axis alignment in the direction of maximum strain induced by plate motion and lithosphere-asthenosphere coupling. The black arrow indicate a NW direction of plate motion inferred from the Great Meteor hotspot track (Figure 5.4), which causes the fast axis to plunge towards SE.*

The main challenge with this plume induced anisotropy interpretation is to connect the interpretation with the MLD observed beneath the North American craton. If the plume caused the change of anisotropy leading to an observed MLD beneath HRV, this means that the origin of the craton wide MLD is different from the MLD observed at HRV. Given that HRV is situated outside the craton, it could be that the lower lithospheric layer observed in other places in North America has not developed outside the craton, and that the base of the lithosphere beneath HRV represents the MLD observed throughout the craton.

If, on the other hand, the results of Yuan and Romanowicz (2010) are based on resolutions too coarse to map anisotropic features within specific regions, such as beneath the Appalachian orogen, the anisotropic fabric in the study

area could hold clues to lithospheric thickening after orogenesis. This is supported through the results of a surface wave study by Deschamps et al. (2008), where three distinct layers of anisotropy have been mapped in the Grenville and Appalachian provinces. The fast axes of these layers coincide well with the findings in this thesis: the top layer has a fast axis in the direction of the Appalachian orogen, and the lower layer (representing the asthenosphere) has a fast axis following present day plate motion. The middle layer is mapped to have a fast axis in the N-NW direction, which for a horizontal axis of anisotropy would coincide with the SE fast axis direction noted in this thesis. Deschamps et al. (2008) attribute the lower lithospheric fabric to the paleo plate motion in the NW direction, with a resulting drag-induced fabric in the lithospheric base, eventually cooling and causing a new "frozen in" pattern of anisotropy.

This last hypothesis would effectively imply the same origin of anisotropic fabric as the first hypothesis, but with a different process leading up to the formation of fabric. In a craton wide study, it would be interesting to see if the shorter wavelength variations to the northern FA in Yuan and Romanowicz (2010) coincide with the hotspot trail, or if it follows other orogens than Grenville and the Appalachians.

10.3 Outlook

As the scope of this thesis is too limited to cover all potential research associated with the lithospheric modeling, I have gathered a series of proposed research projects that would help achieve a more comprehensive study of the MLD in eastern North America.

First, it is important to keep in mind that the forward modeling process is a comparison of idealized synthetic data to real data which contain noise. For this reason amplitudes of real and synthetic data are expected to deviate, and exact matching of amplitudes does not necessarily provide an ideal indication of the anisotropic properties present. An interesting approach would be to

include noise from the real data prior to the direct P-wave arrival, to see how this background noise influences the synthetic model.

The energy at time zero could be an indication of the presence of dip, but as it is hard to locate this exact energy in the harmonic decomposition, this has been assumed to be a near surface effect. Intra-crustal boundaries could cause multiples to appear within the time window of this study, and their presence should therefore be explored further.

Another interesting aspect of this thesis is the sign of other interfaces apparent in the radial and transverse component, as well as the harmonic decomposition. Signals that should be subject of further modeling and interpretation include a potential low velocity layer above the Moho, and the peak at 4.5s. The 4.5s peak is particularly strong in the harmonic decomposition, and it would be interesting to resolve the origin and potentially anisotropic properties of this boundary, to see if the signal can be seen in other places in North America. As several recent papers point towards multiple MLDs, it would be interesting to compare the anisotropic signature of this pulse to those in other places where multiple potential MLDs have been mapped (see e.g. Wirth and Long (2014); Long et al. (2016)).

From studies of the transverse component in Chapter 8 it is clearly important to determine if the interpreted signal arises from the top or bottom boundary of an anisotropic layer. The discrepancies between studies of changing azimuthal anisotropy across the MLD discussed in Wirth and Long (2014) could potentially arise from this, that some people investigate a signal arising from the bottom of the anisotropic layer above the interface, while others interpret the signal arising from the top of the anisotropic layer below the interface. Depending on the velocity contrast across this interface, these signals could yield a different fast axes. An attempt to revisit previous studies with this particular phenomenon in mind would be an interesting approach to potentially link different observations of MLD(s).

Finally, I would expand this to a full regional study of eastern North America, determining anisotropic parameters at all nearby stations through inversion

in order to generate surface maps of the MLD based on anisotropic signature. By obtaining the best fit between synthetic data and a station for a wide range of models through singular parameter inversion, the error between all three displays (radial sum, harmonic decomposition, and summed harmonics) could be minimized simultaneously. Using an automatic approach compared to the manual forward modeling would thereby enable the investigation of a much greater range of models. A promising approach to handle this large dataset more effectively is the semi-automated inversion method described in Licciardi and Agostinetti (2016). In their approach, the presence and depth of anisotropic layers is constrained by an algorithm, thus reducing the potential errors introduced by trial and error through forward modeling.

By tracking the MLD signal throughout a greater part of eastern North America, it would be interesting to see if the anisotropic signature of the MLD follows the proposed plume track. Combining studies of the vertical extent of the lower layer with estimates of plate velocity over the hotspot, in combination with estimates of thermal conductive heat-flow in the lower lithosphere, would also provide an indication of the robustness of this interpretation. Ideally such results should also be verified with other imaging techniques, for example by combining body waves and surface waves as suggested in Calò et al. (2016), or inclusion of ray tracing (Ĉervenŷ, 2001).

Chapter 11

Conclusion

Through forward modeling I found that the best synthetic model to reproduce RFs recorded at MLD depths at HRV contains a change of anisotropic properties, without changes in reference velocity. The anisotropic fast axis changes from horizontal towards the NE above the MLD, to a plunging fast axis towards the SE beneath the MLD, plunging at 60°. I attribute this rapid transition between anisotropic fabrics to an abrupt transition from a "frozen in" anisotropic pattern from a large tectonic event, such as the formation of the Appalachians, to a lower lithospheric fabric reworked or replaced through heating of the lithospheric base, e.g. by a mantle plume. The anisotropic pattern in the upper lithosphere coincides well with results of other studies, but the plume-included anisotropic fabric in the lower lithosphere has not yet been proposed to explain the occurrence of the MLD. A similar explanation has however been put forward based on gradual cooling of the lithospheric base beneath orogens, with fast axes corresponding to past and present day plate motion. As the proposed solution deviates from the craton-wide lower lithospheric layer presented in Yuan and Romanowicz (2010), the results of this thesis can not be used to investigate the origin of the lower lithospheric layer in the North American craton. As HRV is situated outside the craton, a possible implication of this result is that the lower layer does not extend beyond the border of the craton, indicating that the craton-wide MLD could

have a different origin than the MLD signal observed at HRV. It is however difficult to know if there was another anisotropic fabric in place prior to the proposed heating event. In that case, the lower layer could previously have extended outside the craton.

As the result is obtained through forward modeling, an effort to solve this using inversion should also be made for greater robustness of the results. By implementing a semi-automated process, more stations could be included in the investigation.

Bibliography

Babuska, V. and Cara, M. (1991). *Seismic anisotropy in the Earth*, volume 10. Springer Science & Business Media.

Bianchi, I., Park, J., Piana Agostinetti, N., and Levin, V. (2010). Mapping seismic anisotropy using harmonic decomposition of receiver functions: An application to northern apennines, italy. *Journal of Geophysical Research: Solid Earth*, 115(B12).

Bleeker, W. and Davis, B. W. (2004). What is a craton? How many are there? How do they relate? And how did they form? *AGU Spring Meeting Abstracts*.

Blumer, A., Ehrenfeucht, A., Haussler, D., and Warmuth, M. K. (1987). Occam's razor. *Information processing letters*, 24(6):377–380.

Bradley, D. (1989). Taconic plate kinematics as revealed by foredeep stratigraphy, appalachian orogen. *Tectonics*, 8(5):1037–1049.

Bradley, D. C. (1983). Tectonics of the acadian orogeny in new england and adjacent canada. *The Journal of Geology*, 91(4):381–400.

Buchan, K. L., LeCheminant, A. N., and van Breemen, O. (2009). Paleomagnetism and u–pb geochronology of the lac de gras diabase dyke swarm, slave province, canada: implications for relative drift of slave and superior provinces in the paleoproterozoic geological survey of canada contribution 20080350. *Canadian Journal of Earth Sciences*, 46(5):361–379.

Calò, M., Bodin, T., and Romanowicz, B. (2016). Layered structure in the upper mantle across north america from joint inversion of long and short period seismic data. *Earth and Planetary Science Letters*, 449:164–175.

Ĉervenŷ, V. (2001). *Seismic ray theory*. Cambridge University Press, Cambridge, UK.

Christensen, N. I. (1984). The magnitude, symmetry and origin of upper mantle anisotropy based on fabric analyses of ultramafic tectonites. *Geophysical Journal International*, 76(1):89–111.

Chu, R., Leng, W., Helmberger, D. V., and Gurnis, M. (2013). Hidden hotspot track beneath the eastern united states. *Nature Geoscience*, 6(11):963–966.

Connolly, P. (1999). Elastic impedance. *The Leading Edge*, 18(4):438–452.

Das, T. and Nolet, G. (1995). Crustal thickness estimation using high frequency rayleigh waves. *Geophysical research letters*, 22(5):539–542.

Davies, G. F. (1994). Thermomechanical erosion of the lithosphere by mantle plumes. *Journal of Geophysical Research: Solid Earth*, 99(B8):15709–15722.

Deschamps, F., Lebedev, S., Meier, T., and Trampert, J. (2008). Stratified seismic anisotropy reveals past and present deformation beneath the east-central united states. *Earth and Planetary Science Letters*, 274(3):489–498.

Druken, K., Kincaid, C., and Griffiths, R. (2013). Directions of seismic anisotropy in laboratory models of mantle plumes. *Geophysical Research Letters*, 40(14):3544–3549.

Ekström, G., Tromp, J., and Larson, E. W. (1997). Measurements and global models of surface wave propagation. *Journal of Geophysical Research: Solid Earth*, 102(B4):8137–8157.

Fischer, K. M., Ford, H. A., Abt, D. L., and Rychert, C. A. (2010). The lithosphere-asthenosphere boundary. *Annual Review of Earth and Planetary Sciences*, 38:551–575.

Fouch, M. J., Fischer, K. M., Parmentier, E., Wysession, M. E., and Clarke, T. J. (2000). Shear wave splitting, continental keels, and patterns of mantle flow. *Journal of Geophysical Research: Solid Earth*, 105(B3):6255–6275.

Fouch, M. J. and Rondenay, S. (2006). Seismic anisotropy beneath stable continental interiors. *Physics of the Earth and Planetary Interiors*, 158(2):292–320.

Frederiksen, A. and Bostock, M. (2000). Modelling teleseismic waves in dipping anisotropic structures. *Geophysical Journal International*, 141(2):401–412.

Fryer, G. J. and Frazer, L. N. (1984). Seismic waves in stratified anisotropic media. *Geophysical Journal International*, 78(3):691–710.

Fuchs, K. (1977). Seismic anisotropy of the subcrustal lithosphere as evidence for dynamical processes in the upper mantle. *Geophysical Journal International*, 49(1):167–179.

Gaherty, J. B. (2004). A surface wave analysis of seismic anisotropy beneath eastern north america. *Geophysical Journal International*, 158(3):1053–1066.

Griffin, W., O'Reilly, S., Abe, N., Aulbach, S., Davies, R., Pearson, N., Doyle, B., and Kivi, K. (2003). The origin and evolution of archean lithospheric mantle. *Precambrian Research*, 127(1):19–41.

Hansen, S. M., Dueker, K., and Schmandt, B. (2015). Thermal classification of lithospheric discontinuities beneath usarray. *Earth and Planetary Science Letters*, 431:36–47.

Havskov, J. and Ottemoller, L. (2010). *Routine Data Processing in Earthquake Seismology: With Sample Data, Exercises and Software*. Springer Science & Business Media.

Hoffman, P. F. (1988). United plates of america, the birth of a craton: Early proterozoic assembly and growth of laurentia. *Annual Review of Earth and Planetary Sciences*, 16(1):543–603.

Hoffman, P. F. (1989). Precambrian geology and tectonic history of north america. *The Geology of North America*, pages 447–512.

Holtzman, B., Kohlstedt, D., Zimmerman, M., Heidelbach, F., Hiraga, T., and Hustoft, J. (2003). Melt segregation and strain partitioning: implications for seismic anisotropy and mantle flow. *Science*, 301(5637):1227–1230.

Hynes, A. and Rivers, T. (2010). Protracted continental collision—evidence from the grenville orogen. *Canadian Journal of Earth Sciences*, 47(5):591–620.

Karato, S.-i., Olugboji, T., and Park, J. (2015). Mechanisms and geologic significance of the mid-lithosphere discontinuity in the continents. *Nature Geoscience*, 8(7):509–514.

Kearey, P., Brooks, M., and Hill, I. (2013). *An introduction to geophysical exploration*. John Wiley & Sons.

Kosarian, M., Davis, P. M., Tanimoto, T., and Clayton, R. W. (2011). The relationship between upper mantle anisotropic structures beneath california, transpression, and absolute plate motions. *Journal of Geophysical Research: Solid Earth*, 116(B8).

Langston, C. A. (1977). The effect of planar dipping structure on source and receiver responses for constant ray parameter. *Bulletin of the Seismological Society of America*, 67(4):1029–1050.

Langston, C. A. (1979). Structure under mount rainier, washington, inferred from teleseismic body waves. *Journal of Geophysical Research: Solid Earth*, 84(B9):4749–4762.

Lay, T. and Wallace, T. C. (1995). *Modern global seismology*, volume 58. Academic press.

Levin, V., Menke, W., and Park, J. (1999). Shear wave splitting in the appalachians and the urals- a case for multilayered anisotropy. *Journal of Geophysical Research*, 104(17):975–17.

Levin, V., Servali, A., VanTongeren, J., Menke, W., and Darbyshire, F. (2017). Crust-mantle boundary in eastern north america, from the (oldest) craton to the (youngest) rift. *Geological Society of America Special Papers*, 526:SPE526–06.

Liang, C. and Langston, C. A. (2009). Three-dimensional crustal structure of eastern north america extracted from ambient noise. *Journal of Geophysical Research: Solid Earth*, 114(B3).

Licciardi, A. and Agostinetti, N. P. (2016). A semi-automated method for the detection of seismic anisotropy at depth via receiver function analysis. *Geophysical Journal International*, 205(3):1589–1612.

Lin, J. and Parmentier, E. (1989). Mechanisms of lithospheric extension at mid-ocean ridges. *Geophysical Journal International*, 96(1):1–22.

Long, M. D., Jackson, K. G., and McNamara, J. F. (2016). Sks splitting beneath transportable array stations in eastern north america and the signature of past lithospheric deformation. *Geochemistry, Geophysics, Geosystems*, 17(1):2–15.

Lovering, J. (1958). The nature of the mohorovicic discontinuity. *Transactions, American Geophysical Union*, 39(5):947–955.

Mainprice, D. and Nicolas, A. (1989). Development of shape and lattice preferred orientations: application to the seismic anisotropy of the lower crust. *Journal of Structural Geology*, 11(1-2):175–189.

Maupin, V. and Park, J. (2007). Theory and observations—wave propagation in anisotropic media. *Treatise on geophysics*, 1:289–321.

Nicolas, A. (1993). Why fast polarization directions of sks seismic waves are parallel to mountain belts. *Physics of the earth and planetary interiors*, 78(3-4):337–342.

Park, J. and Levin, V. (2002). Seismic anisotropy: tracing plate dynamics in the mantle. *Science*, 296(5567):485–489.

Prodehl, C., Kennett, B., Artemieva, I. M., and Thybo, H. (2013). 100years of seismic research on the moho. *Tectonophysics*, 609:9–44.

Rast, N. (1984). The alleghenian orogeny in eastern north america. *Geological Society, London, Special Publications*, 14(1):197–217.

Rast, N. (1989). The evolution of the appalachian chain. In *The geology of North America—An overview*, volume A, pages 323–348. Geological Society of America, Boulder, Colo.

Reguzzoni, M. and Sampietro, D. (2015). Gemma: An earth crustal model based on goce satellite data. *International Journal of Applied Earth Observation and Geoinformation*, 35:31–43.

Rohrer, G. S. (2001). *Structure and bonding in crystalline materials*. Cambridge University Press.

Romanowicz, B. (2011). Surface waves. In *Encyclopedia of Solid Earth Geophysics*, pages 1406–1419. Springer.

Rondenay, S. (2009). Upper mantle imaging with array recordings of converted and scattered teleseismic waves. *Surveys in geophysics*, 30(4-5):377–405.

Rondenay, S., Bostock, M. G., Hearn, T. M., White, D. J., and Ellis, R. M. (2000). Lithospheric assembly and modification of the se canadian shield: Abitibi-grenville teleseismic experiment. *Journal of Geophysical Research: Solid Earth*, 105(B6):13735–13754.

Rondenay, S., Spieker, K., Sawade, L., Halpaap, F., and Farestveit, M. (2017). Glimer: A new global database of teleseismic receiver functions for imaging earth structure. *Seismological Research Letters*, 88(1):39–48.

Rychert, C. A., Fischer, K. M., and Rondenay, S. (2005). A sharp lithosphere–asthenosphere boundary imaged beneath eastern north america. *Nature*, 436(7050):542–545.

Rychert, C. A., Rondenay, S., and Fischer, K. M. (2007). P-to-s and s-to-p imaging of a sharp lithosphere-asthenosphere boundary beneath eastern north america. *Journal of Geophysical Research: Solid Earth*, 112(B8).

Savage, M. (1999). Seismic anisotropy and mantle deformation: what have we learned from shear wave splitting? *Reviews of Geophysics*, 37(1):65–106.

Selway, K., Ford, H., and Kelemen, P. (2015). The seismic mid-lithosphere discontinuity. *Earth and Planetary Science Letters*, 414:45–57.

Silver, P. G. (1996). Seismic anisotropy beneath the continents: Probing the depths of geology. *Annual review of earth and planetary sciences*, 24(1):385–432.

Stein, S. and Wysession, M. (2009). *An introduction to seismology, earthquakes, and earth structure*. John Wiley & Sons.

Svenningsen, L. and Jacobsen, B. H. (2004). Comment on "improved inversion for seismic structure using transformed, s-wavevector receiver functions: Removing the effect of the free surface" by anya reading, brian kennett, and malcolm sambridge. *Geophysical research letters*, 31(24).

Taylor, J. P. and Fitzgerald, P. G. (2011). Low-temperature thermal history and landscape development of the eastern adirondack mountains, new york: Constraints from apatite fission-track thermochronology and apatite (u-th)/he dating. *Geological Society of America Bulletin*, 123(3-4):412–426.

Van Staal, C., Dewey, J., Mac Niocaill, C., and McKerrow, W. (1998). The cambrian-silurian tectonic evolution of the northern appalachians and british caledonides: history of a complex, west and southwest pacific-type segment of iapetus. *Geological Society, London, Special Publications*, 143(1):197–242.

Wiener, R. W., McLelland, J. M., Isachsen, Y. W., and Hall, L. M. (1984). Stratigraphy and structural geology of the adirondack mountains, new york: Review and synthesis. *Geological Society of America Special Papers*, 194:1–56.

Wirth, E. A. and Long, M. D. (2014). A contrast in anisotropy across mid-lithospheric discontinuities beneath the central united states—a relic of craton formation. *Geology*, 42(10):851–854.

Yang, T. and Leng, W. (2014). Dynamics of hidden hotspot tracks beneath the continental lithosphere. *Earth and Planetary Science Letters*, 401:294–300.

Yuan, H. and Levin, V. (2014). Stratified seismic anisotropy and the lithosphere-asthenosphere boundary beneath eastern north america. *Journal of Geophysical Research: Solid Earth*, 119(4):3096–3114.

Yuan, H. and Romanowicz, B. (2010). Lithospheric layering in the north american craton. *Nature*, 466(7310):1063–1068.

Appendix A

Test overview

Table A.1: *Summary of tests and their main results. Figure references indicating figures in Appendices B and C.*

Test	What was tested?	Figure(s)
1	Azimuthal variations in anisotropy (Slow to fast interface)	B.1- B.8
2	Azimuthal variations in anisotropy (Fast to slow interface)	B.12-B.4
3	Difference in dip angle	B.13-B.19
4	Plunge angles of the fast axis	B.20-B.34
5	Azimuthal variation to the plunging axis	B.35-B.42
6	Total energy of the harmonic decomposition	B.43-B.45
7	Time difference between k=0 and higher order harmonics	C.11-C.13
8	Azimuthal variations to layer B in the final model	C.14-C.20
9	4.5s boundary added	C.27-C.30

Main findings from tests;
1: Change of polarity follow the fast axis
2: No difference with velocity change across the interface.
3: Increasing dip angle increase energy on the transverse component
4: Change from π to 2π symmetry after 45°plunge angle
5: Energy on k=1 NS/EW follow the direction of the fast axis
6: The summed harmonic decomposition depends on azimuth of the fast axis
7: Horizontal axis of anisotropy overlaying a plunging anisotropy produce the greatest time difference
8: 45°azimuth of the FA in layer B produce the best fit for the harmonic decomposition
9: The 4.5s boundary fits well, but requires further modeling to be included.

Appendix B

Results of synthetic modeling

This chapter contains the full set of synthetic models with variations in fast axis (horizontal and plunging) and dip for a simple model of one layer overlying a half-space as described in Chapter 7. Anisotropy resides in the half-space in all models, and velocity increases with depth across the boundary.

B.1 Radial, transverse and harmonic decomposition

B.1.1 Azimuthal variations to the fast axis

Radial and transverse component for a 45° parameter search of fast axis azimuth. The modeled harmonic is included, to see how the signal changes from between the individual components.

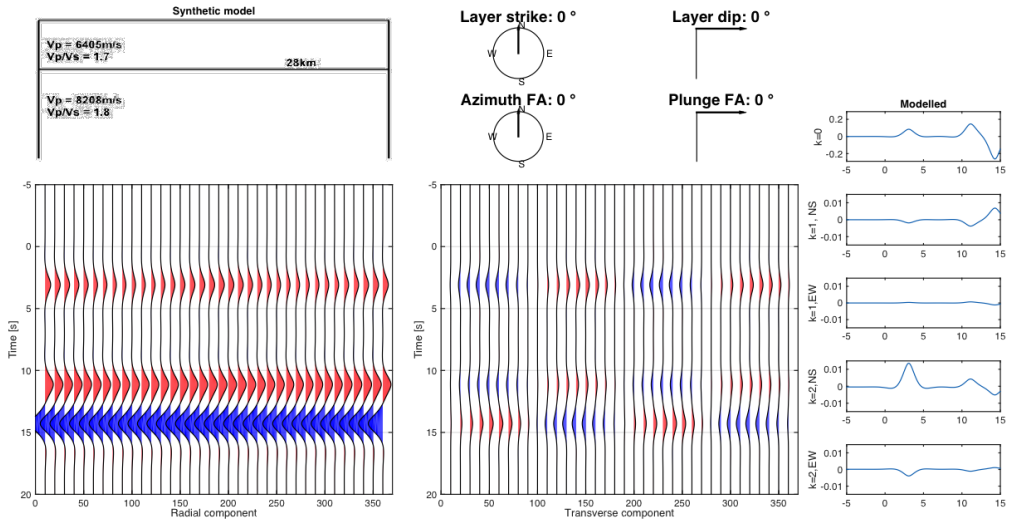

Figure B.1

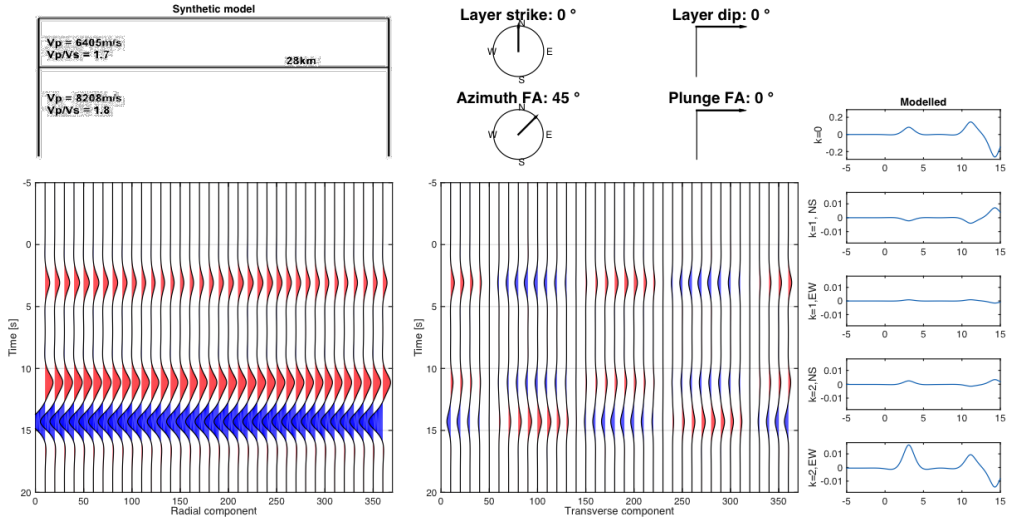

Figure B.2

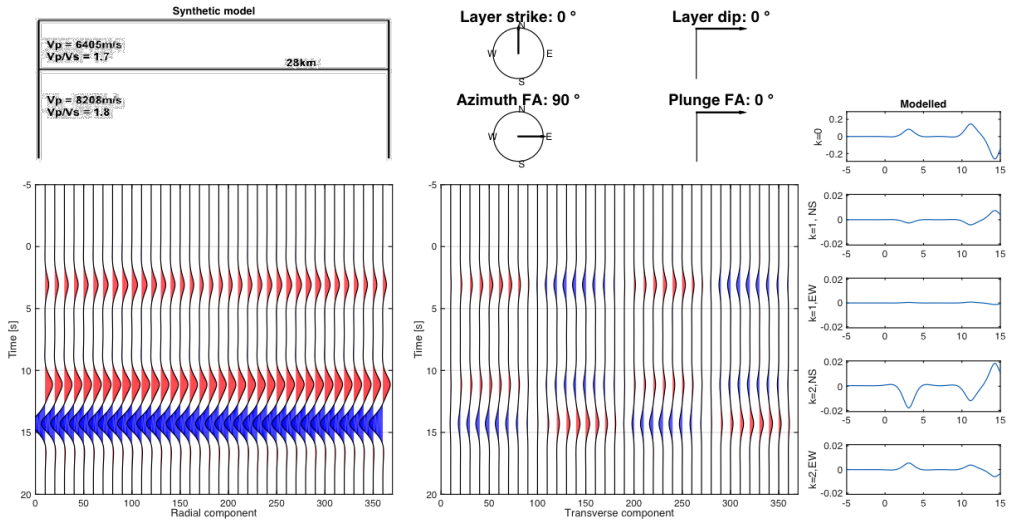

Figure B.3

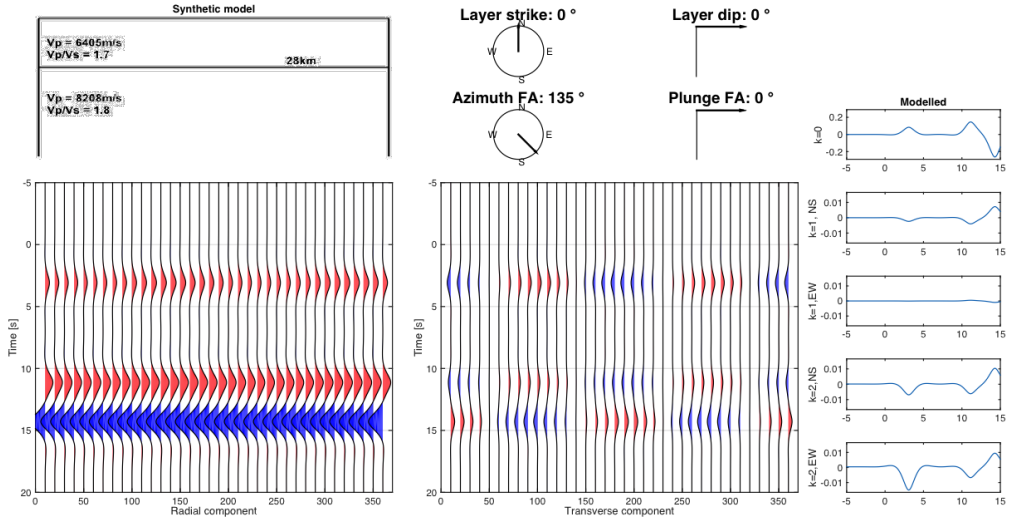

Figure B.4

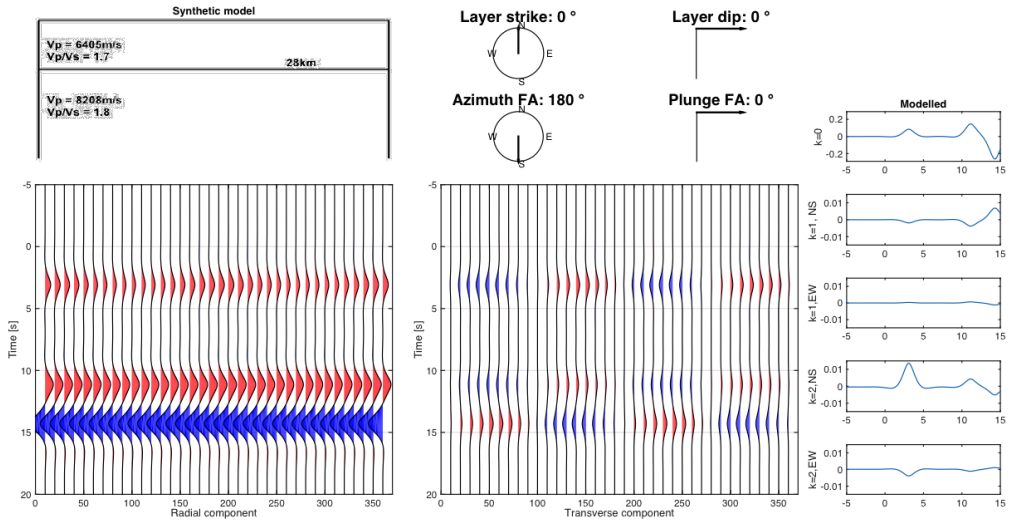

Figure B.5

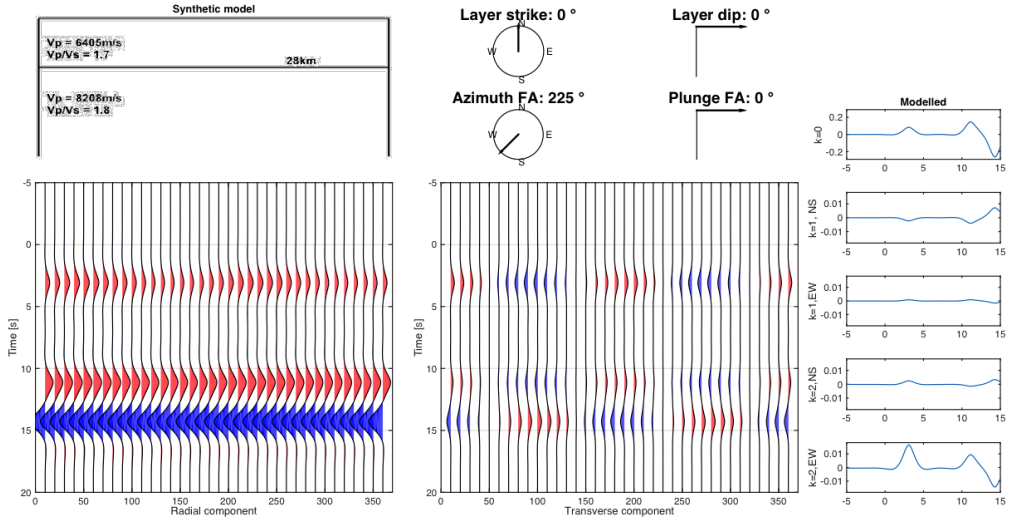

Figure B.6

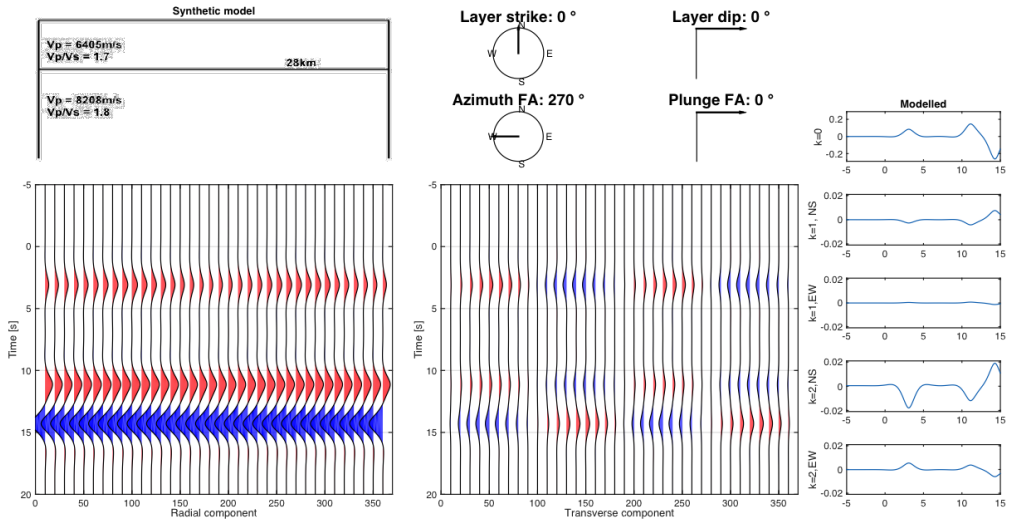

Figure B.7

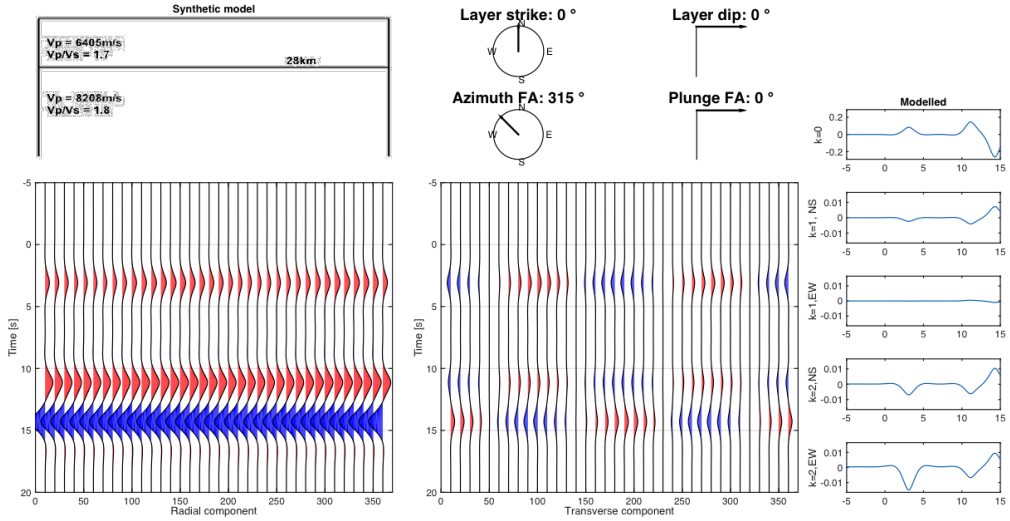

Figure B.8

B.1.2 Azimuthal anisotropy, velocity reduction with depth

This section shows the anisotropic signature in case of horizontal anisotropy and a velocity reduction with depth. Due to the π periodicity of horizontal anisotropy, only the first 4 models are shown for a comparison to the horizontal anisotropic signature with a velocity increase with depth (from the previous section).

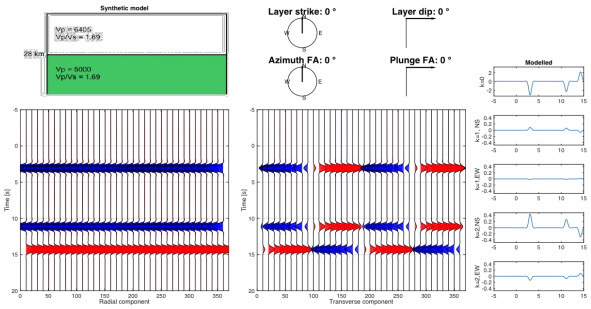

Figure B.9

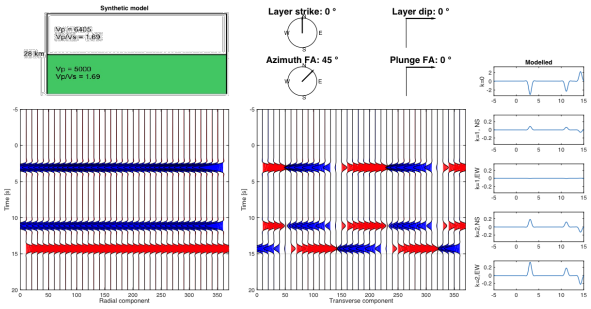

Figure B.10

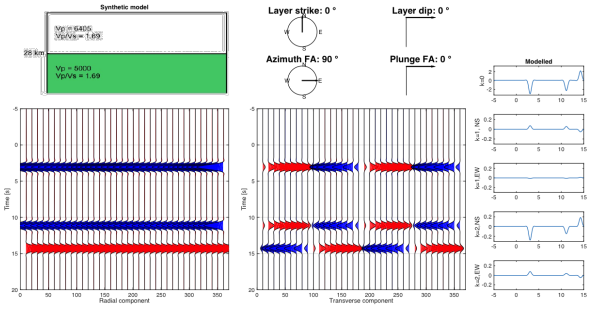

Figure B.11

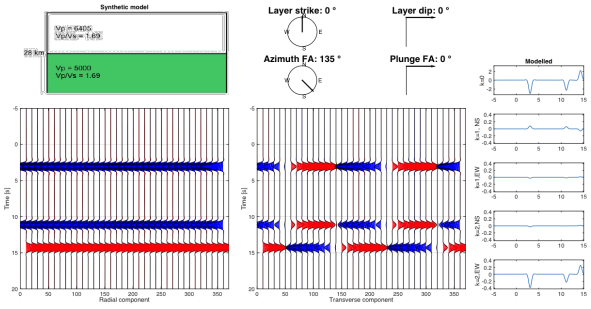

Figure B.12

B.1.3 Dip angles

This section displays the radial and transverse components for an isotropic simple model, where the boundary between the layer and the half-space is dipping. In this section, all models have dip towards the north. To investigate the signature of end members, a dip angle up to 30° has been investigated, despite being an unlikely large angle at such depths.

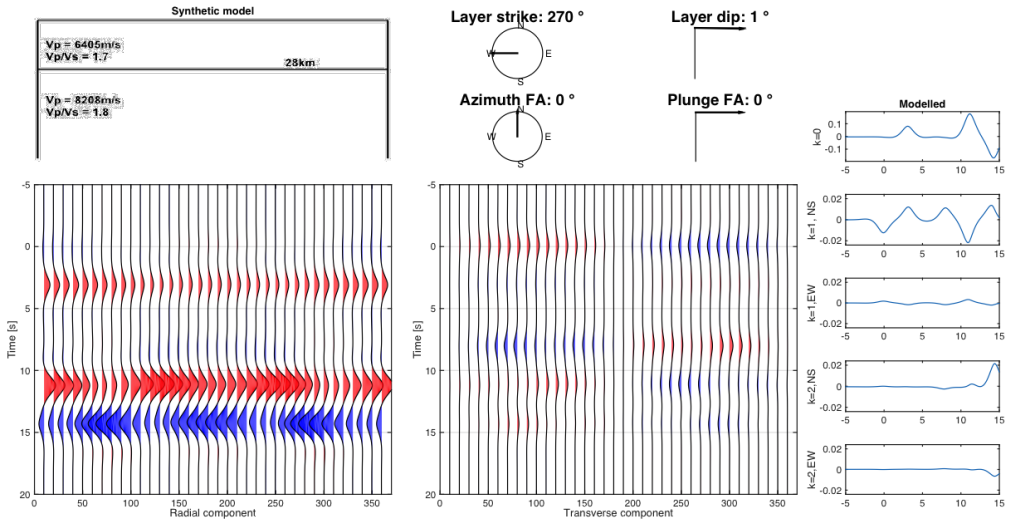

Figure B.13

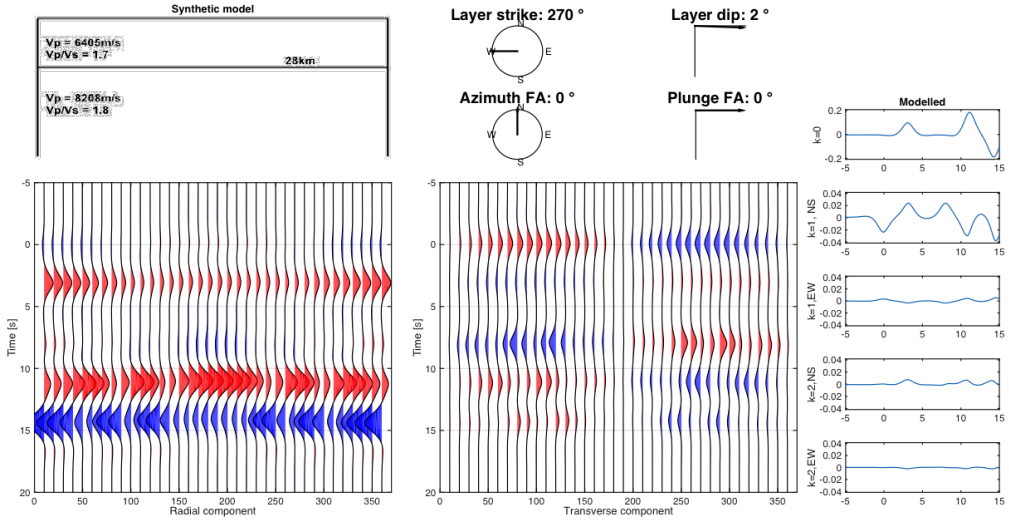

Figure B.14

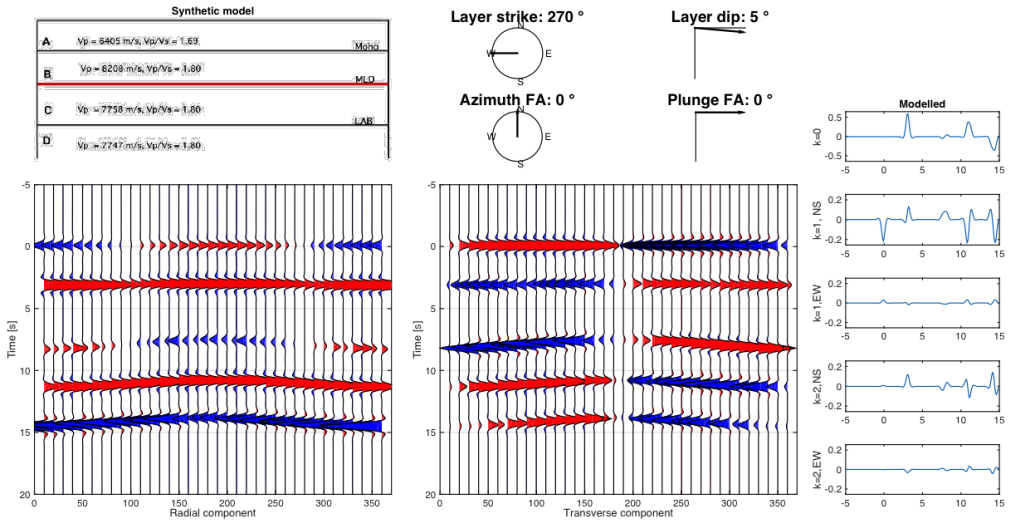

Figure B.15

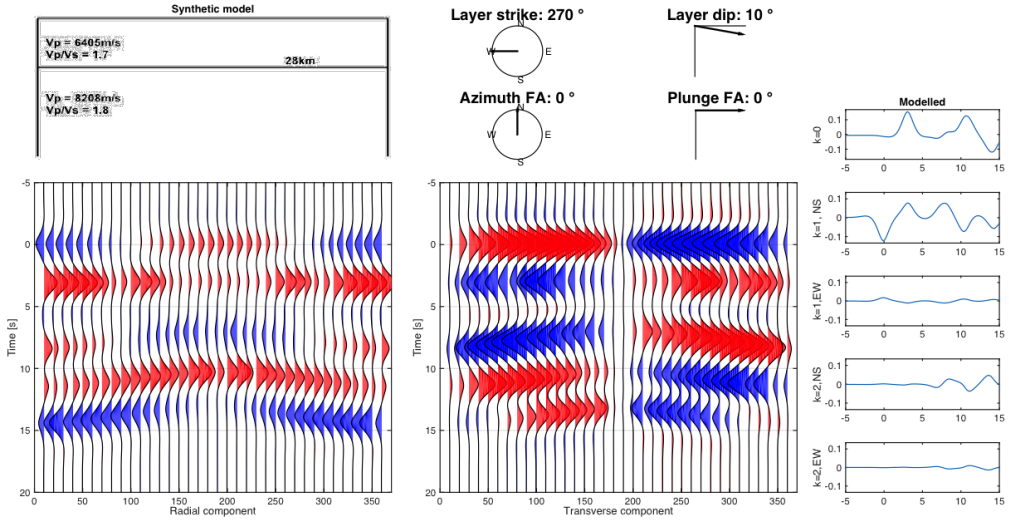

Figure B.16

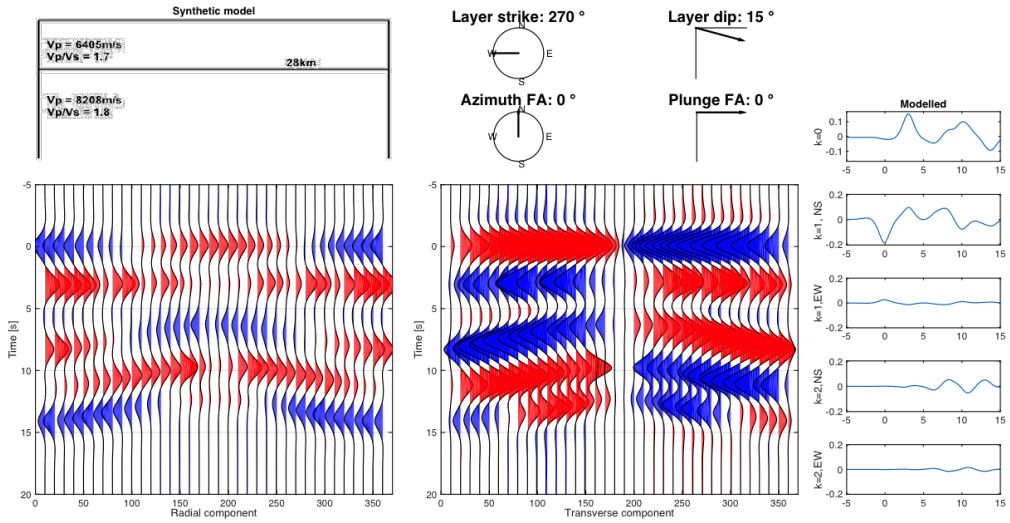

Figure B.17

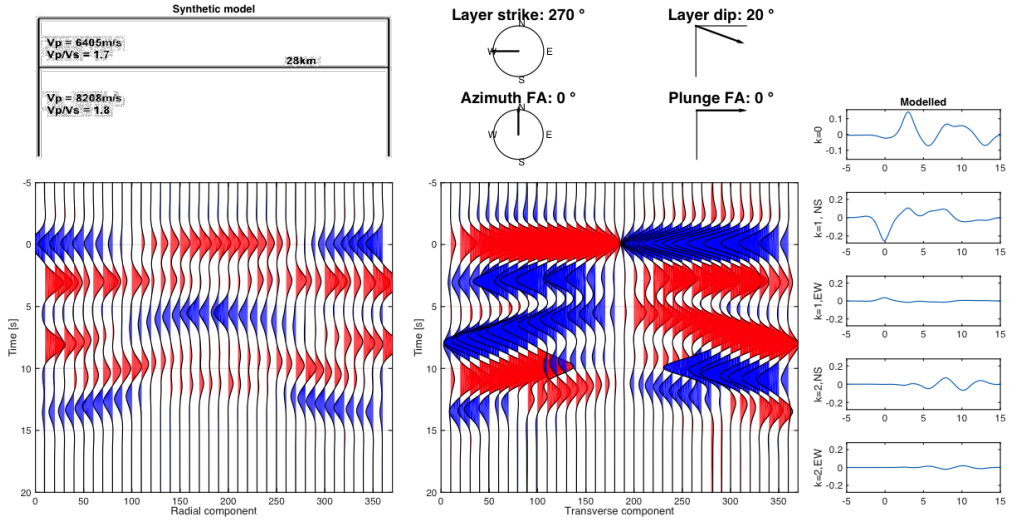

Figure B.18

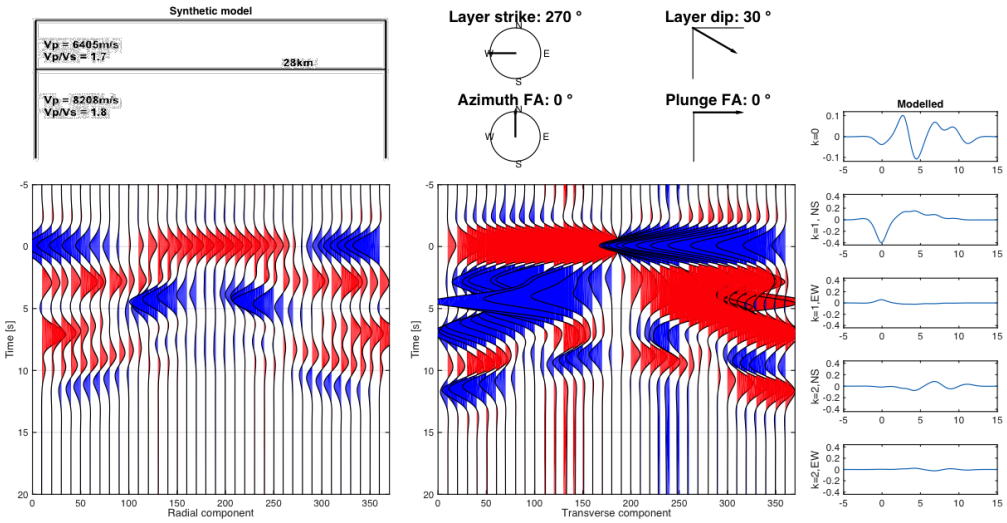

Figure B.19

B.1.4 Various angles of plunging anisotropy

Radial and transverse component for a parameter search of fast axis plunge. The modeled harmonic is included, to see how the signal changes from between the individual components, and the main signal changing from k=2 to k=1. All models have a fast axis trending north.

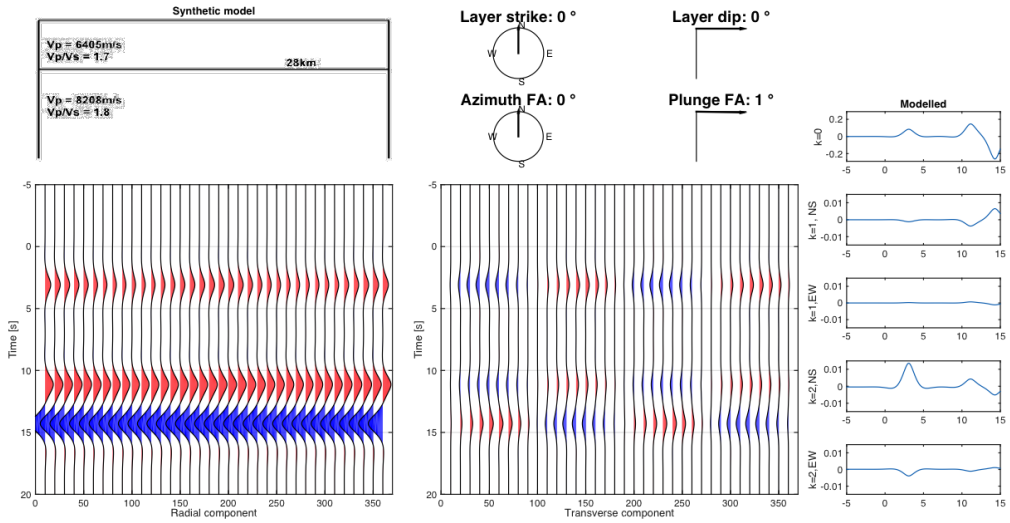

Figure B.20

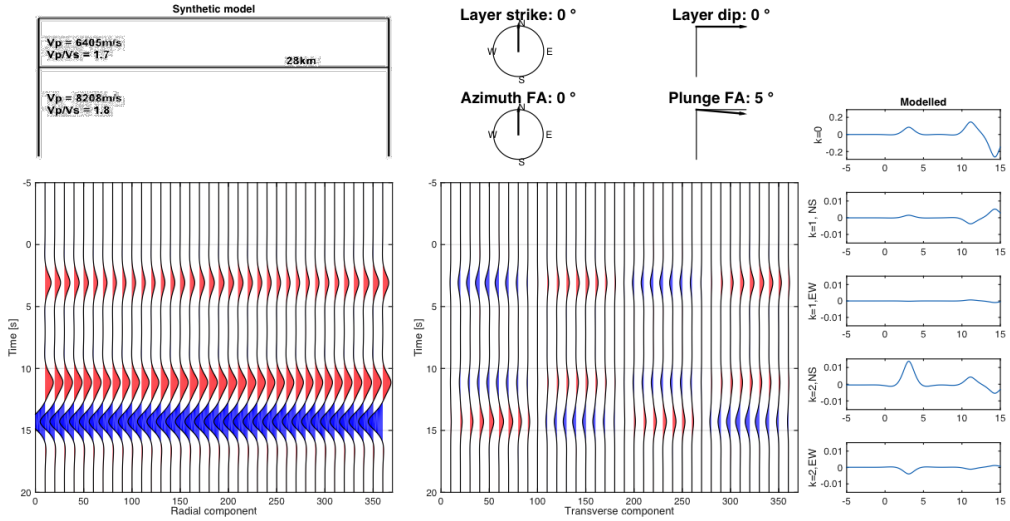

Figure B.21

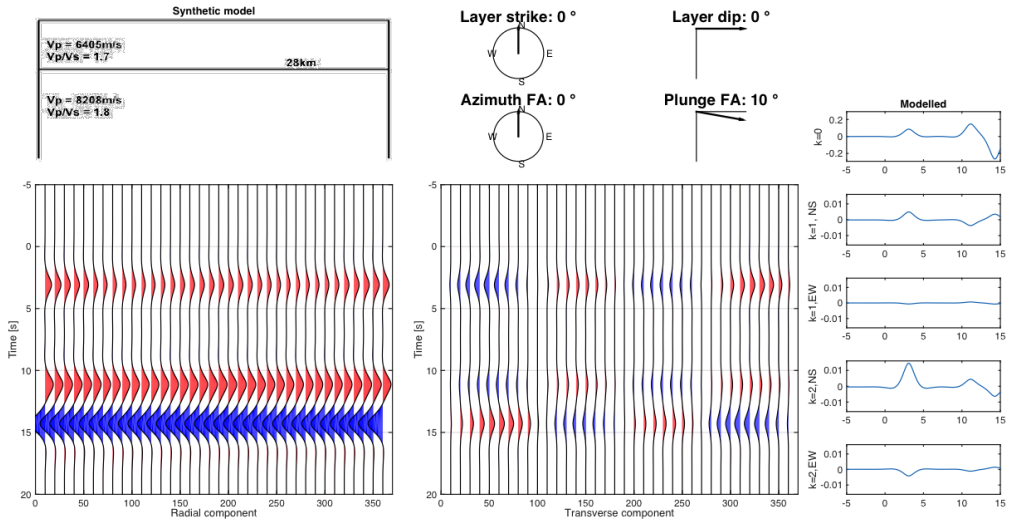

Figure B.22

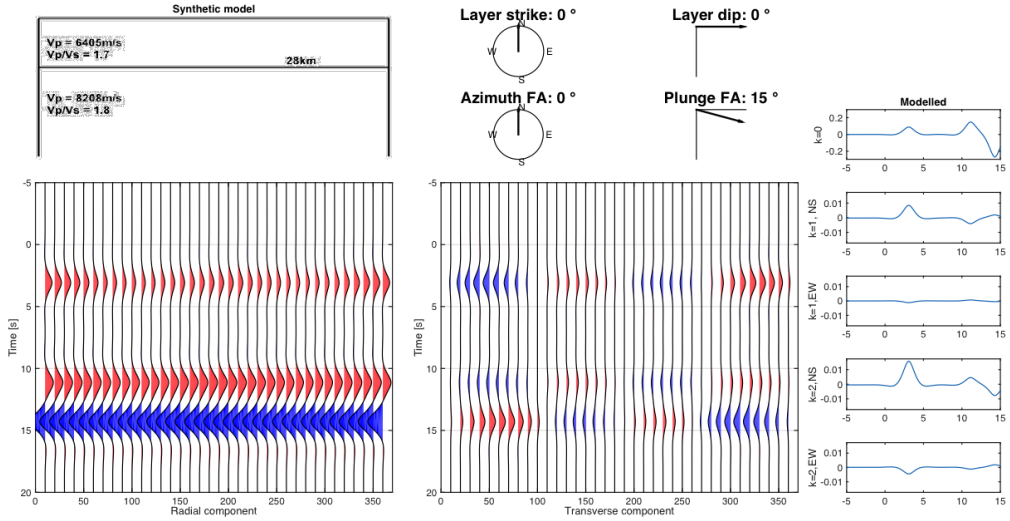

Figure B.23

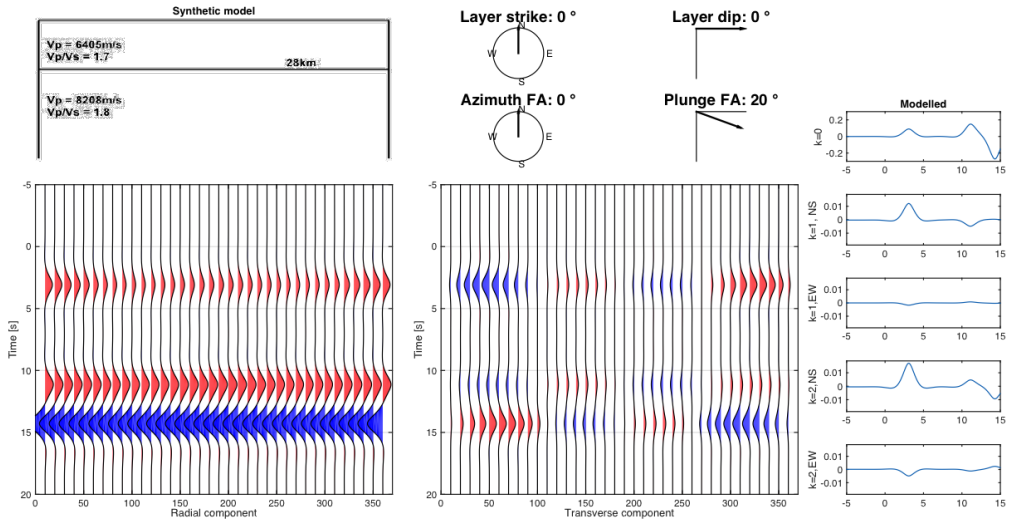

Figure B.24

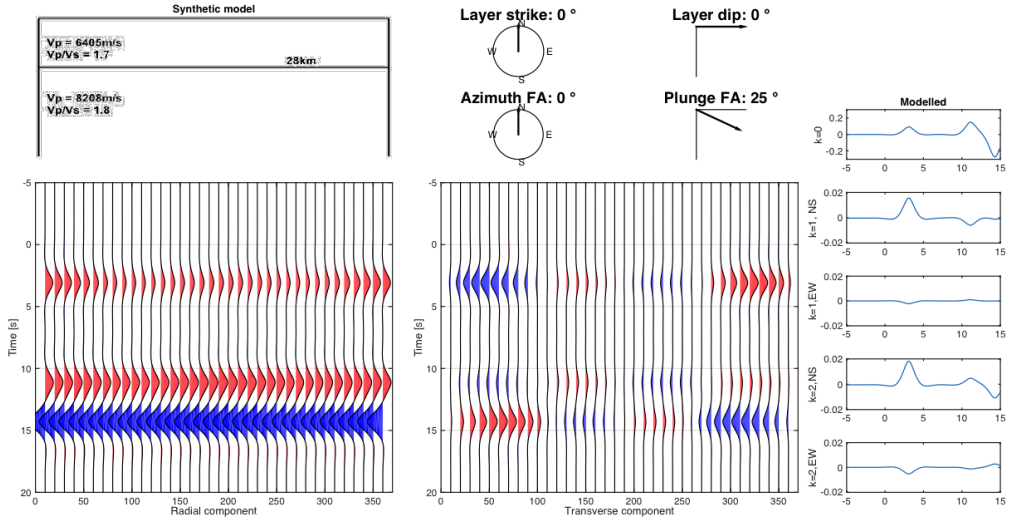

Figure B.25

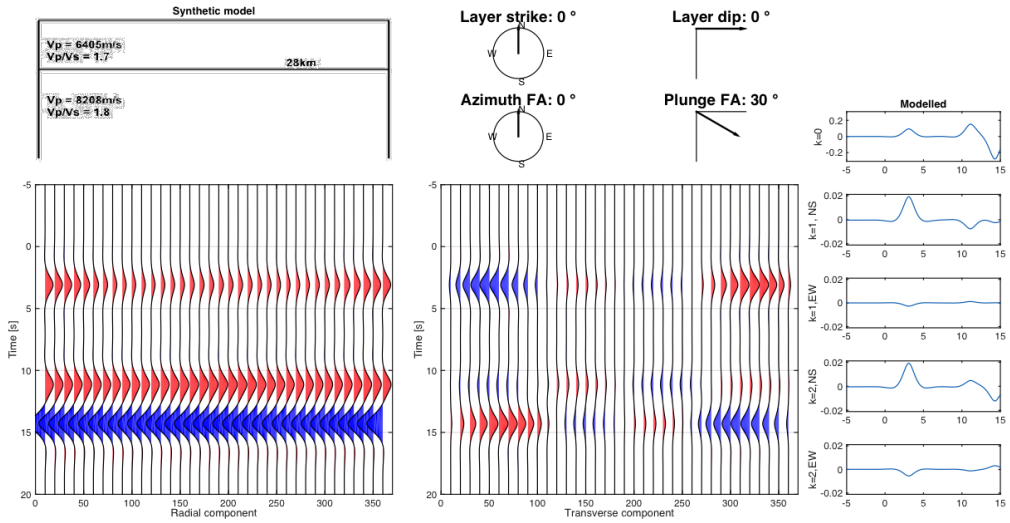

Figure B.26

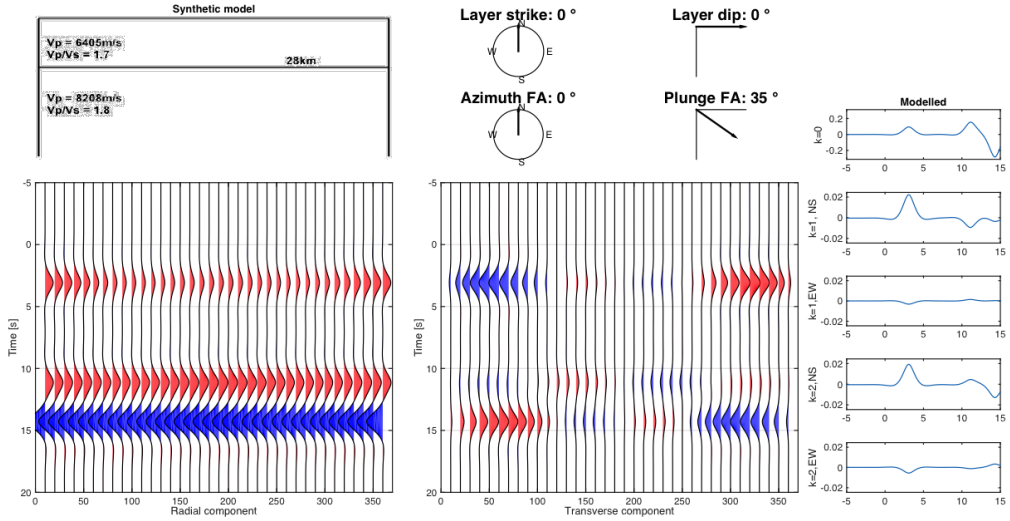

Figure B.27

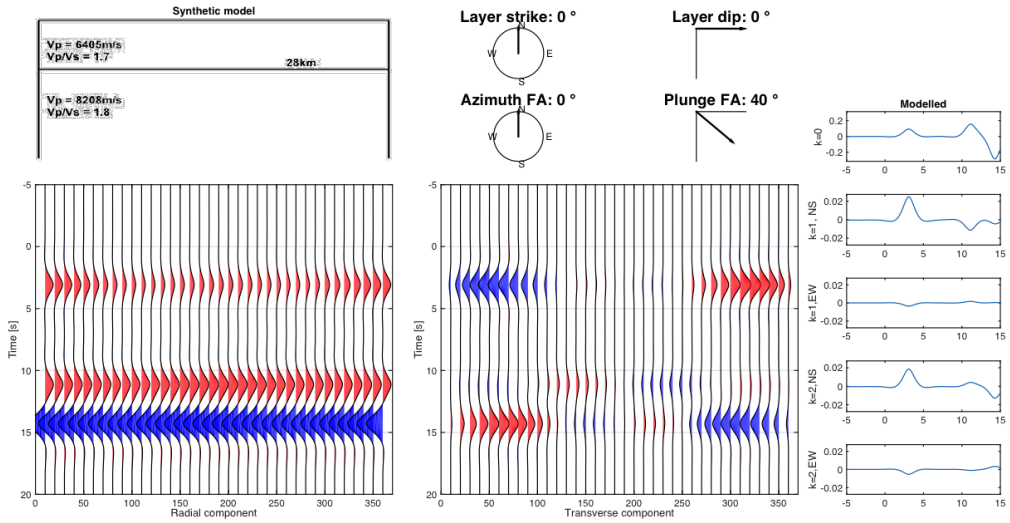

Figure B.28

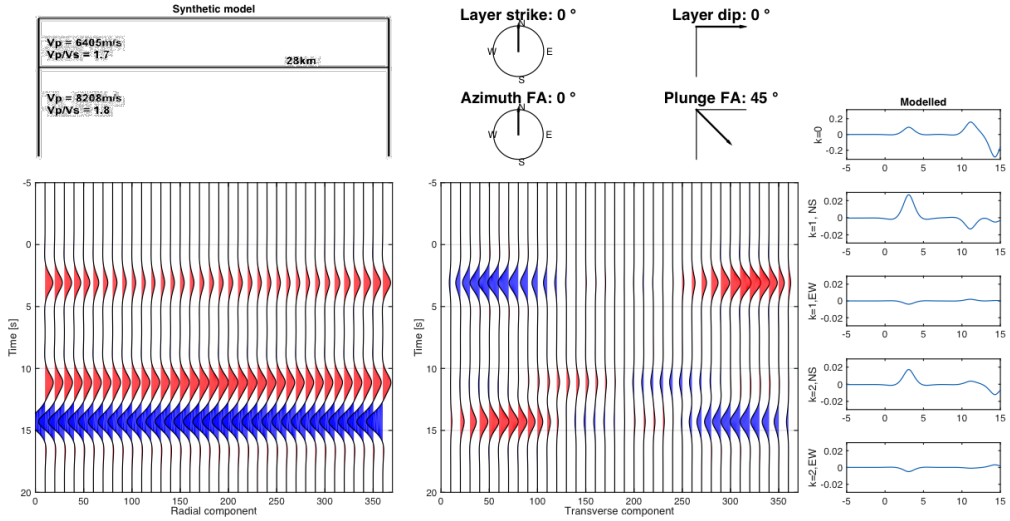

Figure B.29

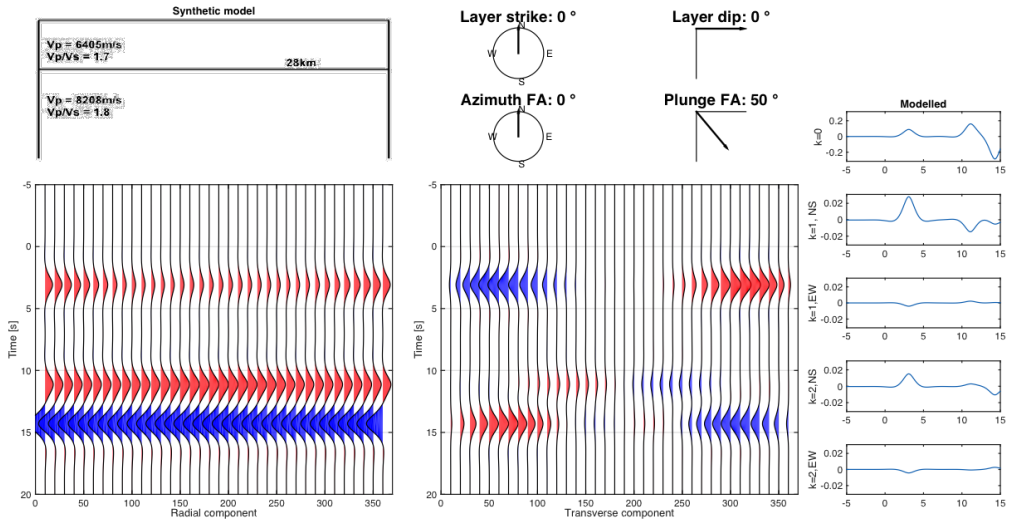

Figure B.30

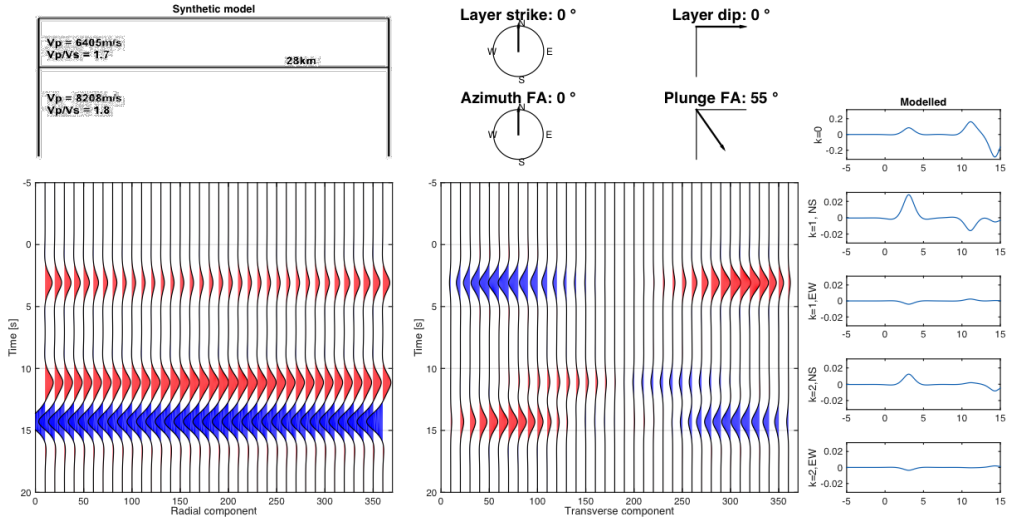

Figure B.31

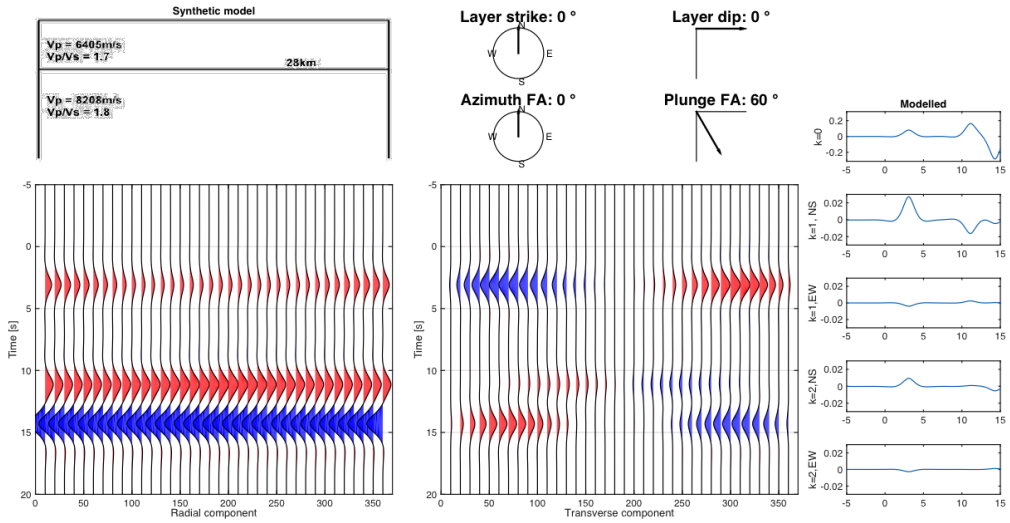

Figure B.32

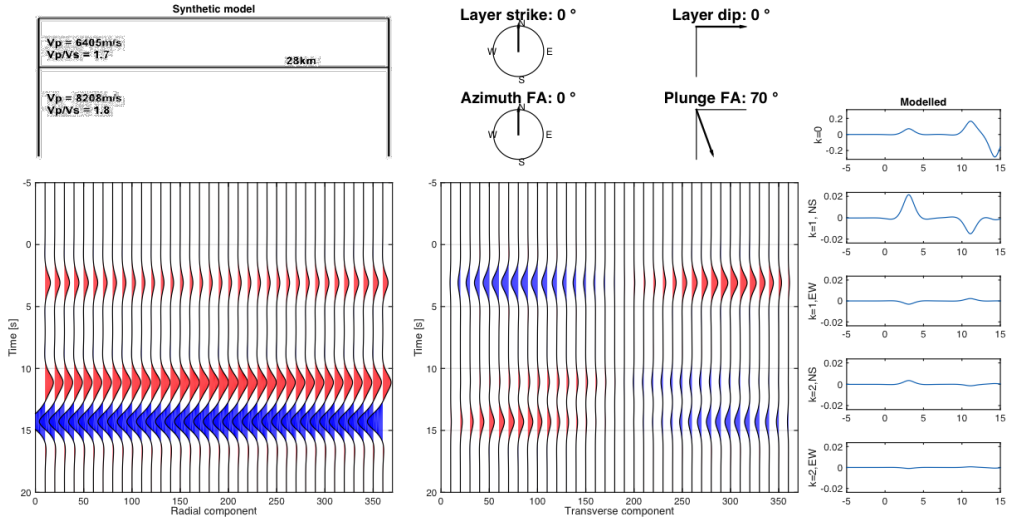

Figure B.33

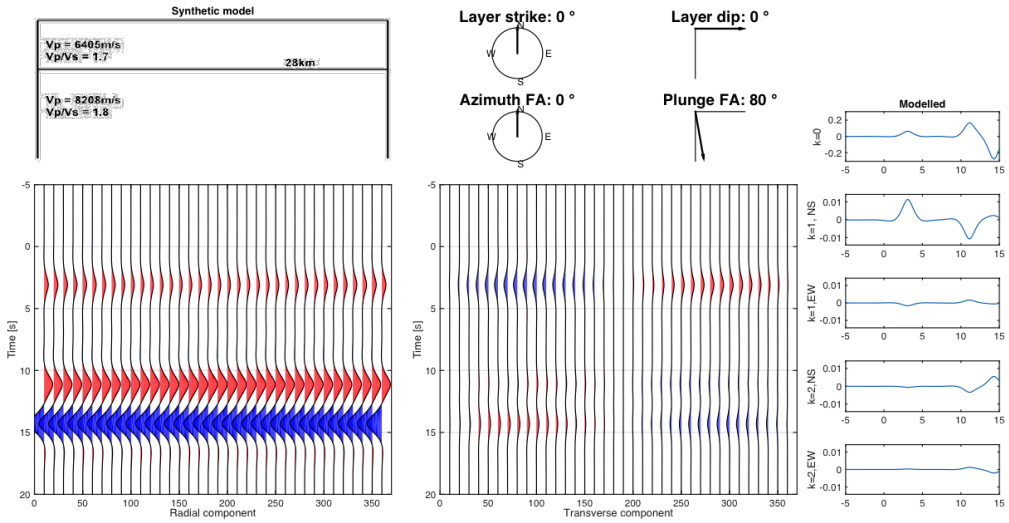

Figure B.34

B.1.5 Azimuthal directions of the plunging fast axis

In this section I investigate how the azimuthal direction of the plunging fast axis affects the components of the harmonic decomposition. Properties of the models are the same as in the section above, with changing azimuth. The plunge of the fast axis is fixed to 60°.

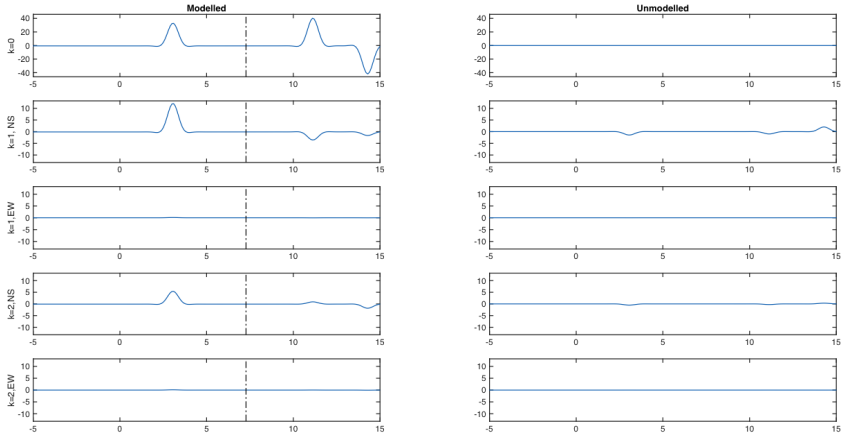

Figure B.35

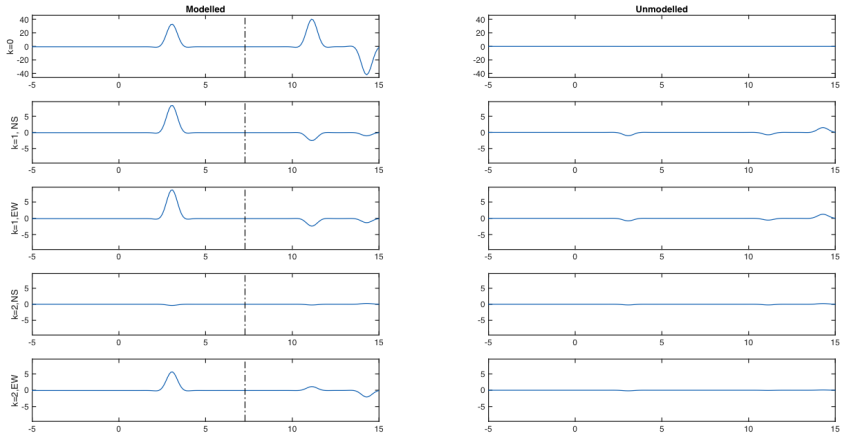

Figure B.36

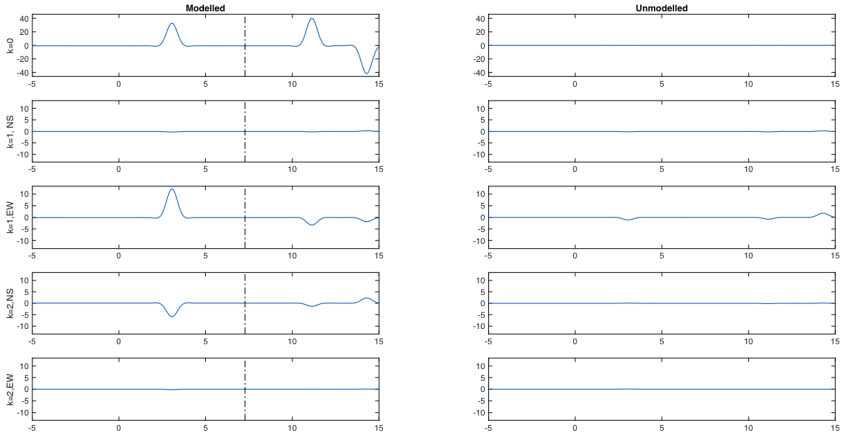

Figure B.37

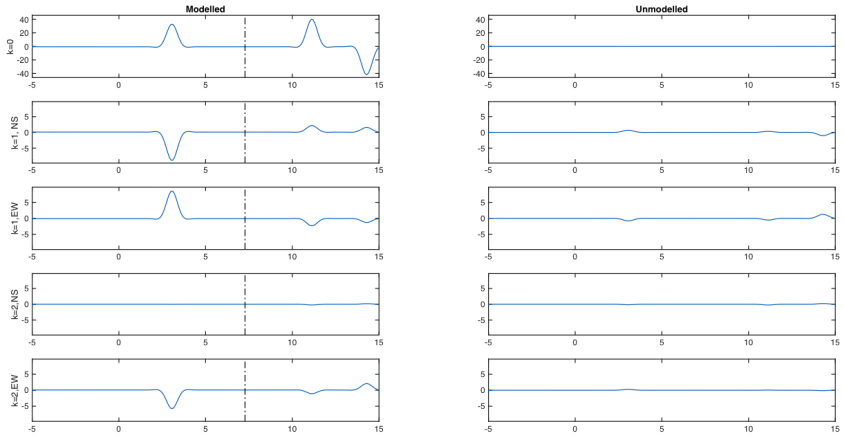

Figure B.38

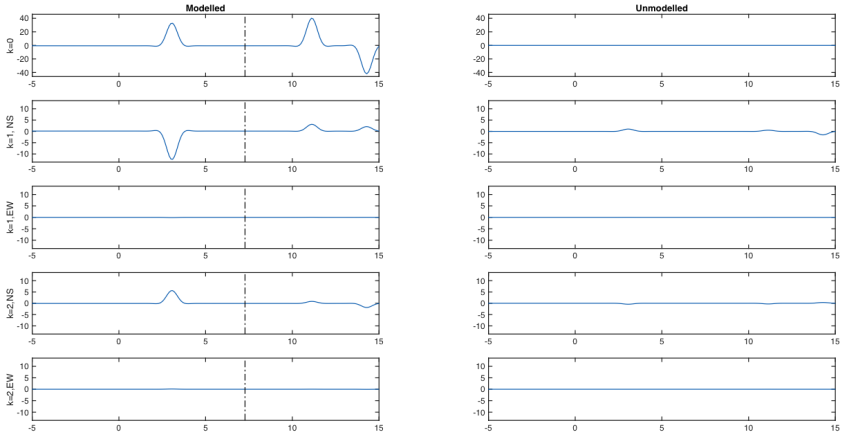

Figure B.39

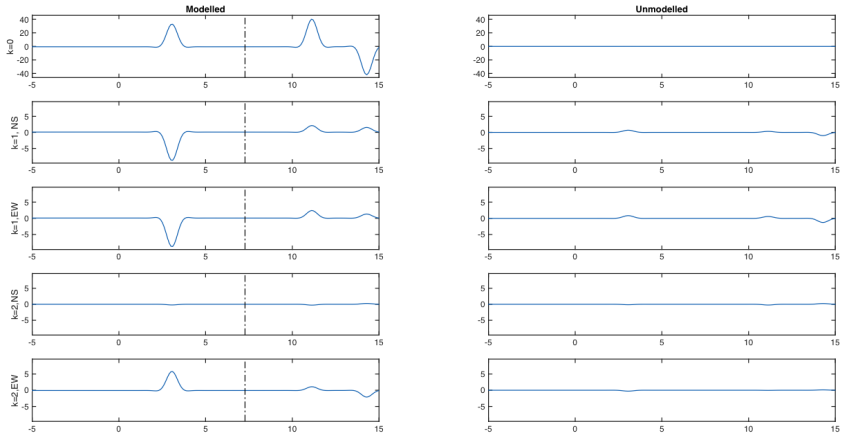

Figure B.40

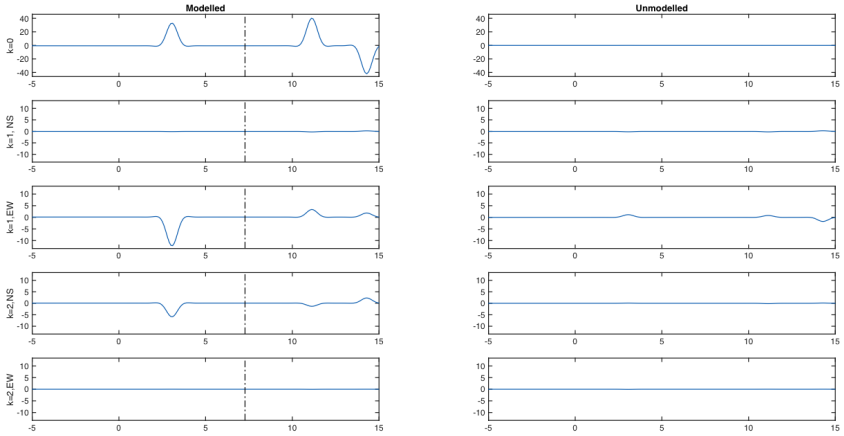

Figure B.41

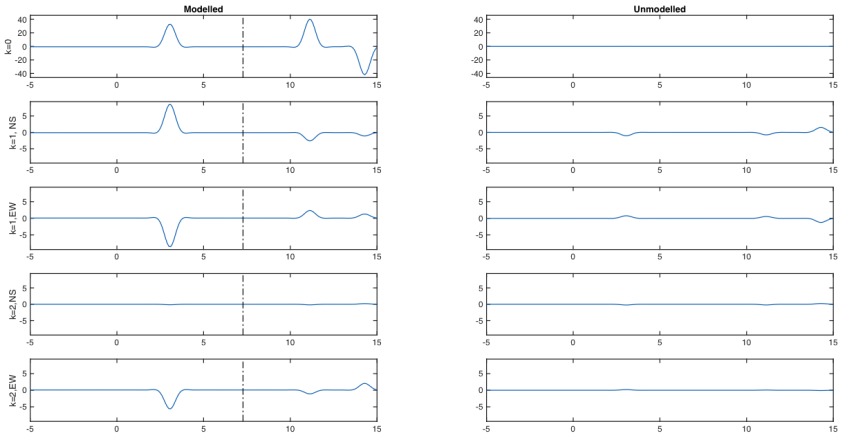

Figure B.42

B.2 Total energy of harmonic decomposition for the three types

This section displays how the signal strength and timing varies for different angles of horizontal FA, plunging FA, and dip.

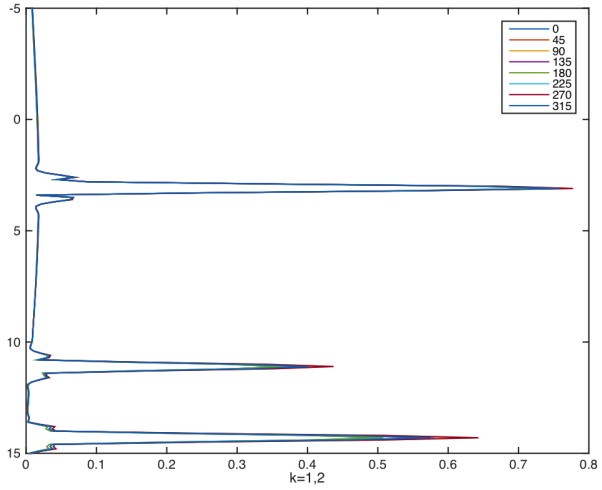

Figure B.43: *Total anisotropic/dip energy for a simple one-layer model. The change of total energy is periodic, with maximum occurring with a fast axis in the E-W direction (90 and 270°)*

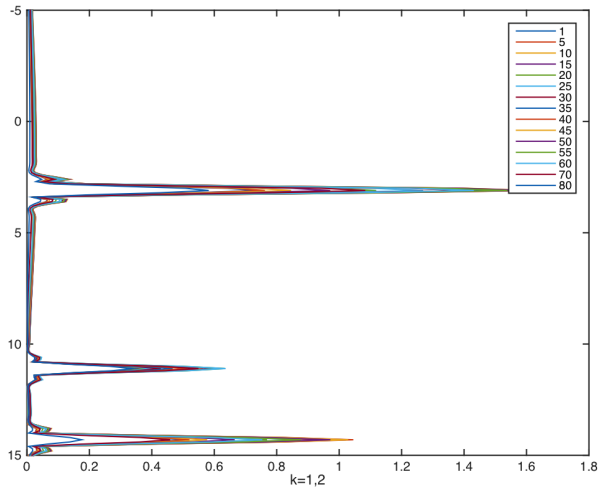

s

Figure B.44: *Total anisotropic/dip energy for higher order harmonics (k=1,2), for various plunging axes of anisotropy.*

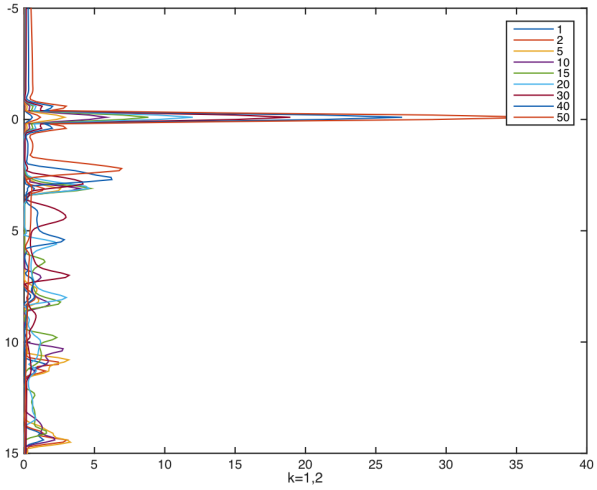

Figure B.45: *Total anisotropic/dip energy for all dips indicated by the legend. The total energy increases with increasing dip. The interface around 3s is the only signal appearing by a real phenomena. Note that multiples arrive at different times according to dip angle.*

B.3 Additional examples for chapter 8.4

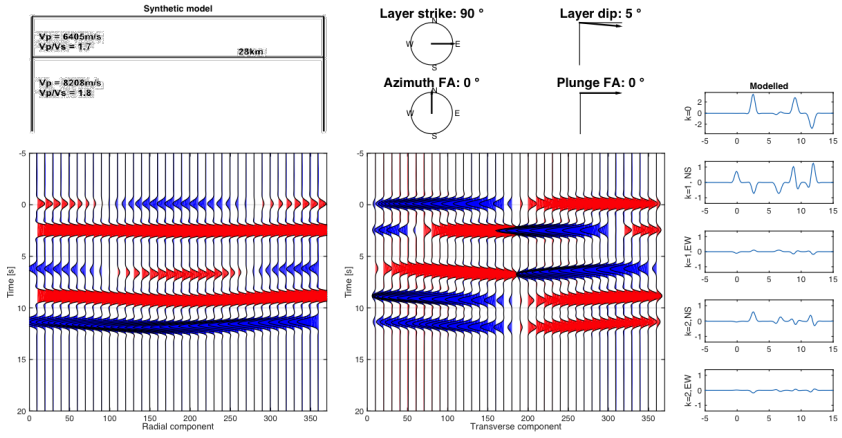

Figure B.46

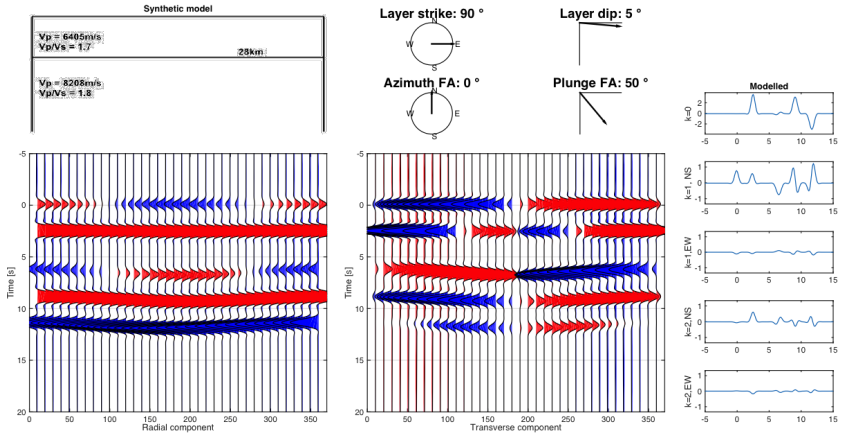

Figure B.47

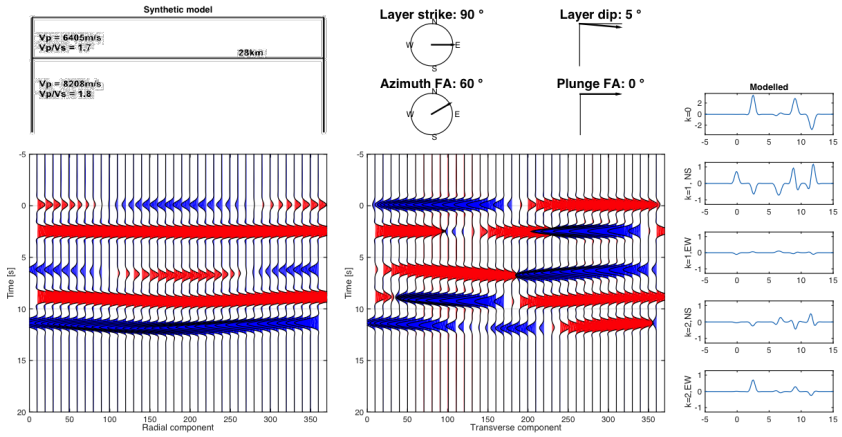

Figure B.48

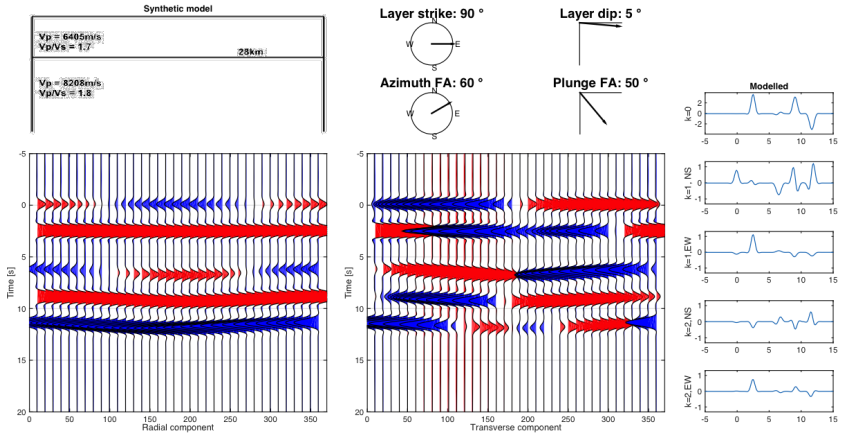
Synthetic model
Vp = 6405m/s
Vp/Vs = 1.7
28km
Vp = 8205m/s
Vp/Vs = 1.8
Layer strike: 90 °
Layer dip: 5 °
Azimuth FA: 60 °
Plunge FA: 50 °
N
W
E
S
Modelled
k=0
k=1, NS
k=1,EW
k=2,NS
k=2,EW
Time [s]
Radial component
Transverse component

Figure B.49

Appendix C

Forward modeling of synthetic data to match HRV

C.1 Best fit with velocity changes across the MLD

A low velocity layer was initially added to fit the signal above the Moho to the radial. This was later removed in order to obtain the simplest possible model. P13 provide a good fit for the radial, but the relative amplitude between k=1 and k=2 is off. HD10 is also a good radial fit, with a relatively good time shift between k0 and k=1/k=2, but amplitudes are too strong. M10 is a good model for the full harmonics, but with too little time shift between k0 and k=1/k=2, and is not a great match for the radial.

Table C.1: *M10 parameters (including a low velocity layer above Moho)*

Layer	**Thickness** [m]	**Vp** [m/s]	**Vs** [m/s]	ρ [kg/m^3]	**%**	**Trend**	**Plunge**
1	23000	6405	3790	2600	0	-	-
2	6380	6175	3529	2600	0	-	-
3	26800	7830	3915	3200	1	85	0
4	26450	7710	3671	3200	2.9	0	50
5	-	7640	3638	3200	0.5	45	0

Table C.2: *P13 parameters. % velocity reduction according to Rychert et al. 2005, including a low velocity layer above the Moho.*

Layer	**Thickness** [m]	**Vp** [m/s]	**Vs** [m/s]	ρ [kg/m^3]	**%**	**Trend**	**Plunge**
1	23000	6405	3790	2600	0	-	-
2	6380	6175	3529	2600	0	-	-
3	29800	7100	3945	3200	4	85	0
4	29450	6780	3767	3200	3	0	50
5	-	6508	3616	3200	2	45	0

Table C.3: *Parameters of HD10*

Layer	**Thickness** [m]	**Vp** [m/s]	**Vs** [m/s]	ρ [kg/m^3]	**%**	**Trend**	**Plunge**
1	23000	6405	3790	2600	0	-	-
2	6380	6175	3529	2600	0	-	-
3	26800	7830	3915	3200	6	85	0
4	26450	7710	3835	3200	6	0	50
5	-	7640	3820	3200	2	45	0

Table C.4: *Vp/Vs ratios for the three models*

Layer	**HD10**	**P13**	**Mari10**
1	1.69	1.69	1.69
2	1.75	1.75	1.75
3	2.0	1.80	2.0
4	2.0	1.80	2.1
5	2.0	1.80	2.1

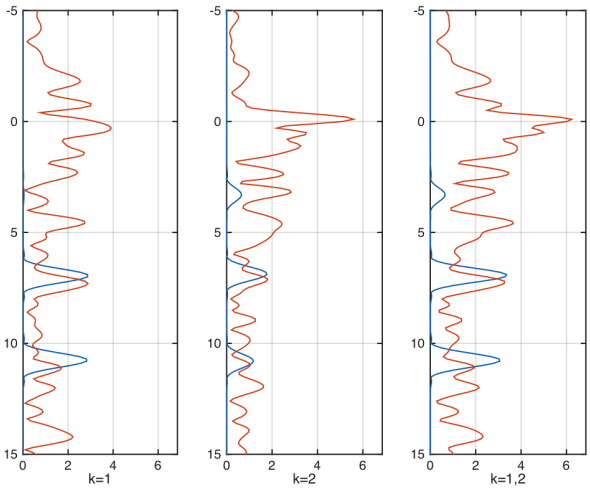

Figure C.1: *M10*

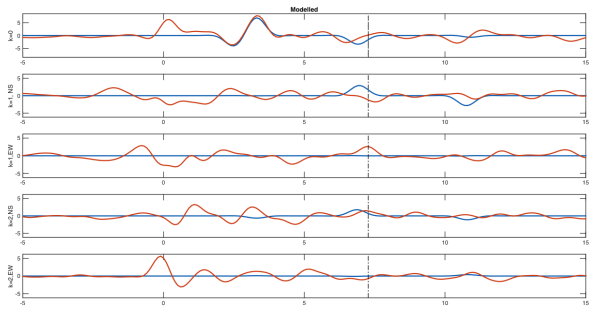

Figure C.2: *M10*

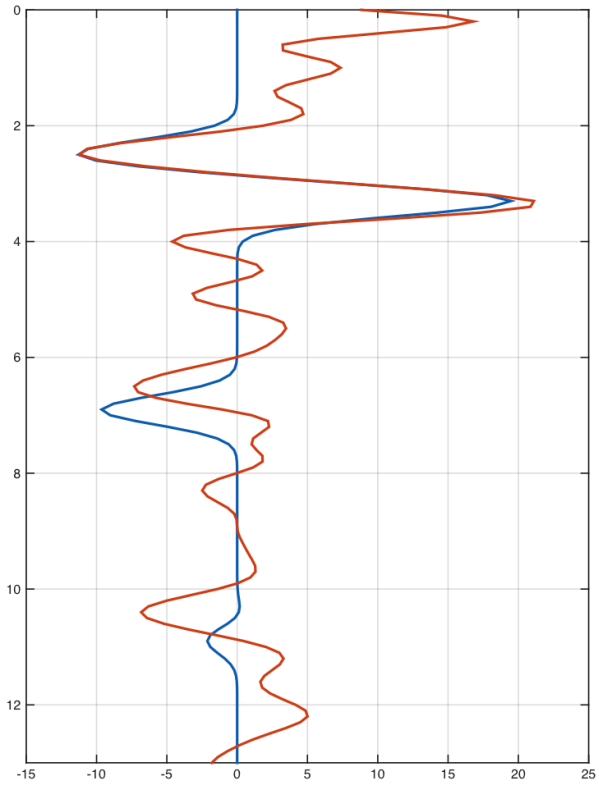

Figure C.3: *M10*

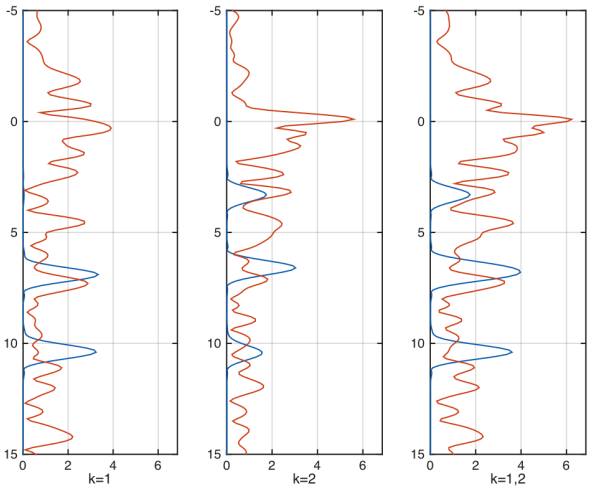

Figure C.4: *P13*

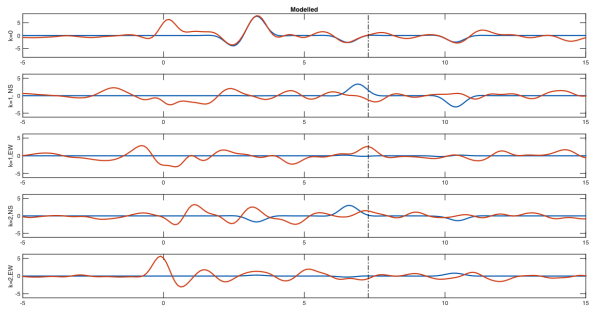

Figure C.5: *P13*

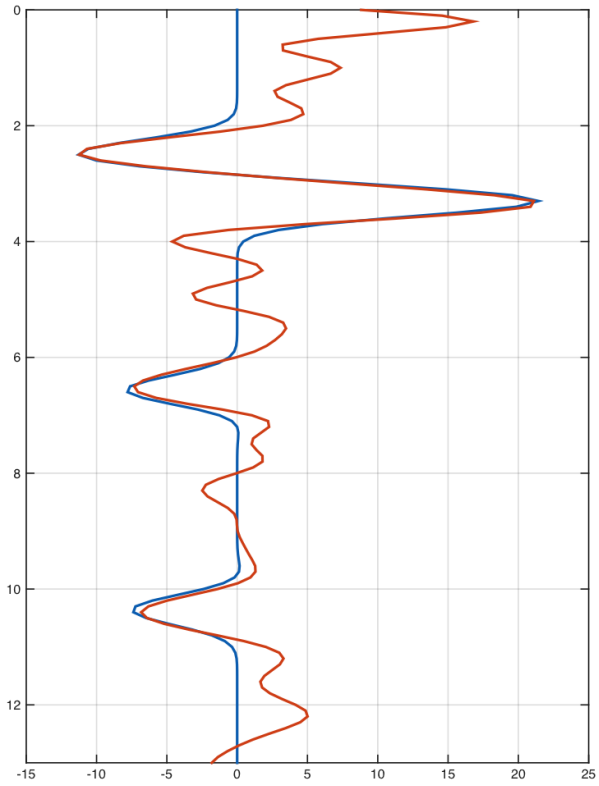

Figure C.6: *P13*

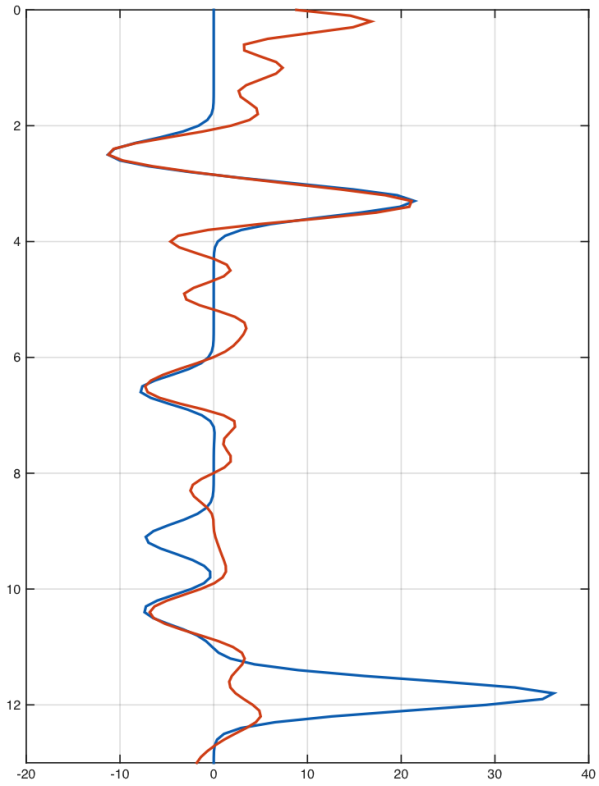

Figure C.7: *P13 with multiples*

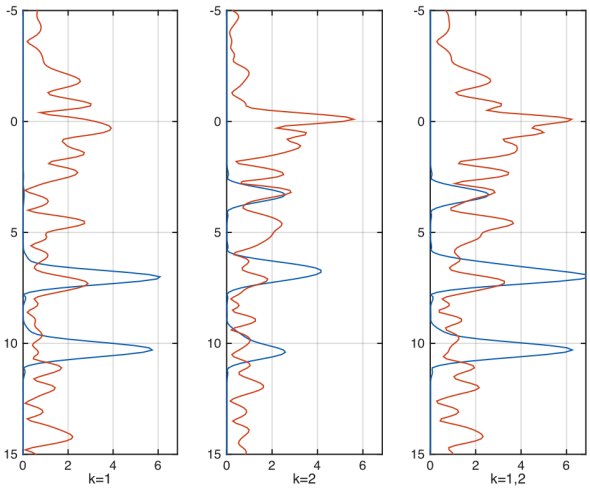

Figure C.8: *HD10*

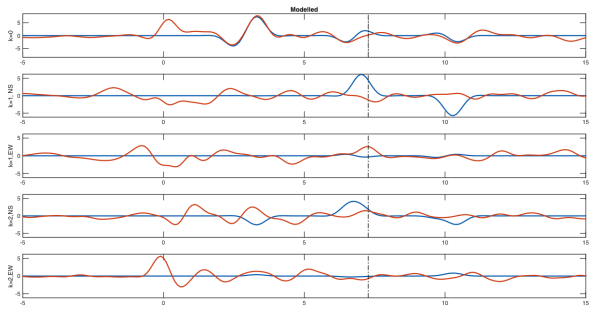

Figure C.9: *HD10*

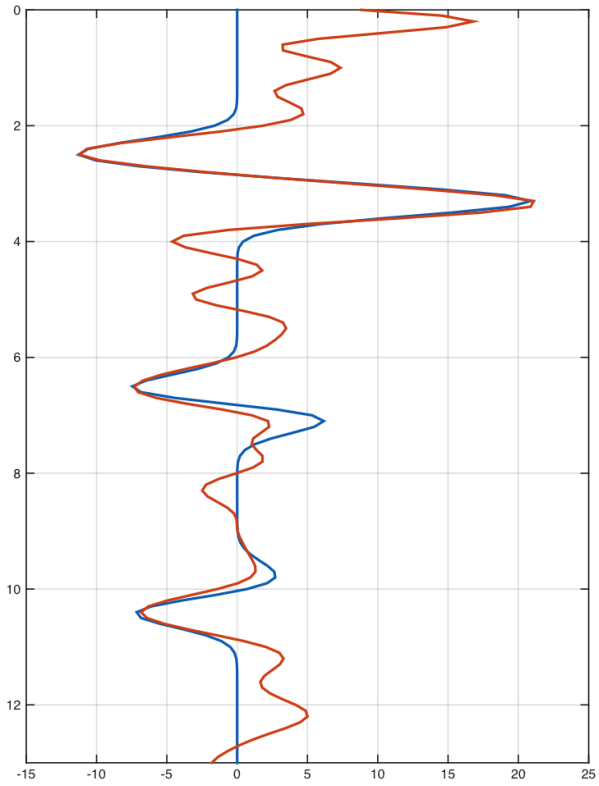

Figure C.10: *HD10*

C.2 Time difference between k=0 and higher order harmonics for different plunge models

Table C.5: *Model parameters for the test of time difference introduced between k=0 and higher order harmonics. Values of ∇_1 and ∇_2 is found in Table C.6.*

Thickness	ρ	α	β	iso	%P	%S	Trend	Plunge
29500	2600	6405	3790	N	-	-	-	-
36500	3200	8208	4557	Y	8.0	8.0	0	ζ_1
33000	3200	8202	4557	Y	3.0	3.0	90	ζ_2
0	3200	7747	4303	Y	3.0	3.0	0	0

Table C.6: *Plunge of the fast axis in the layer above (ζ_1) and below (ζ_2) a boundary.*

	ζ_1	ζ_2
T1	0 °	60°
T2	60°	0 °
T3	60°	60°

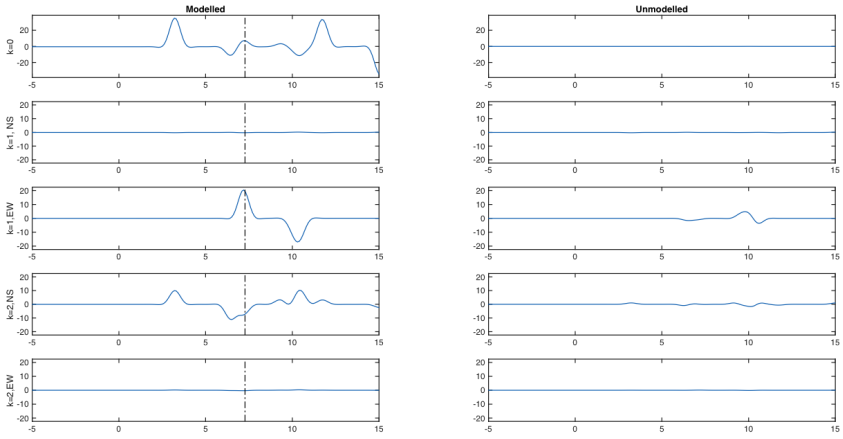

Figure C.11: *Harmonic decomposition of model T1 (see Table C.5 and C.6 for model parameters)*

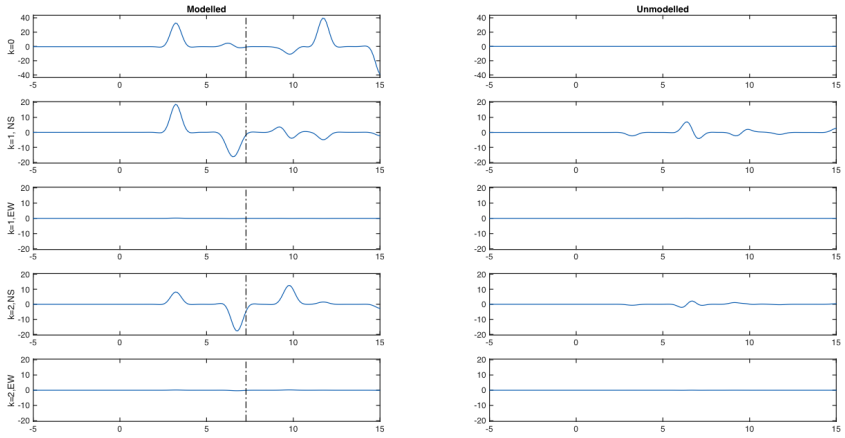

Figure C.12: *Harmonic decomposition of model T2 (see Table C.5 and C.6 for model parameters*

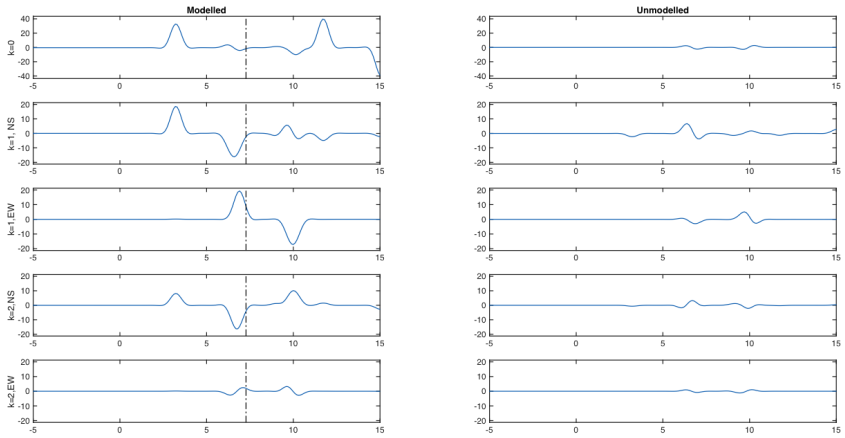

Figure C.13: *Harmonic decomposition of model T3 (see Table C.5 and C.6 for model parameters*

C.3 Azimuthal variations to the fast axis in upper layer, final model

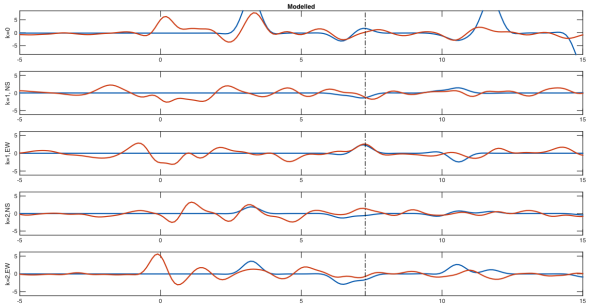

Figure C.14: *Azimuth FA: 30°.*

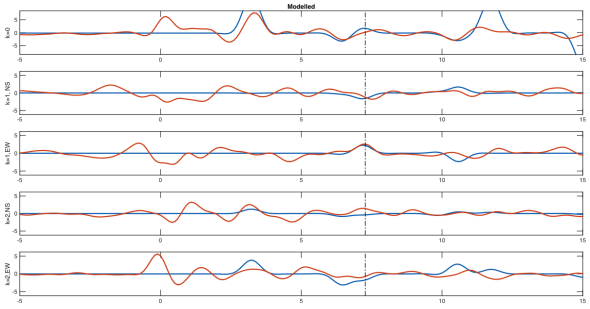

Figure C.15: *Azimuth FA: 35°.*

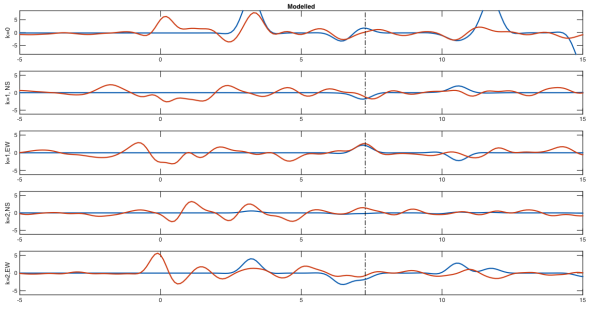

Figure C.16: *Azimuth FA: 40°.*

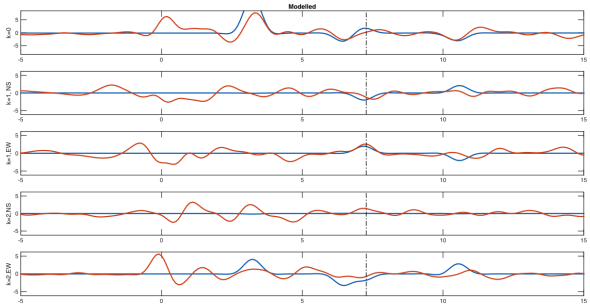

Figure C.17: *Azimuth FA: 45°.*

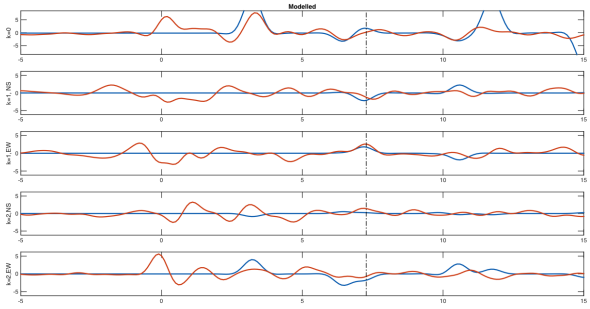

Figure C.18: *Azimuth FA: 50°.*

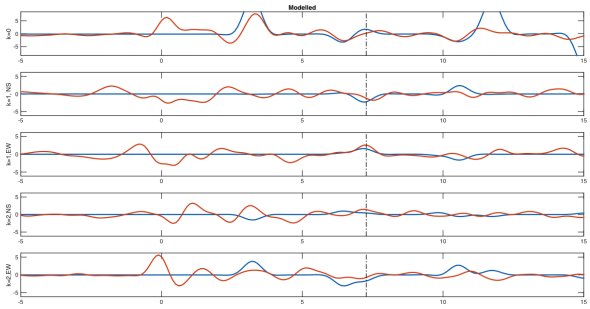

Figure C.19: *Azimuth FA: 55°.*

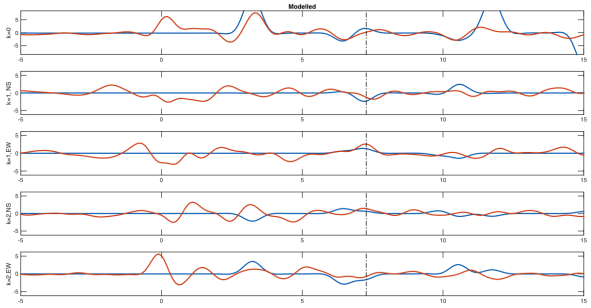

Figure C.20: *Azimuth FA: 60°.*

C.4 Variations around 60° plunge

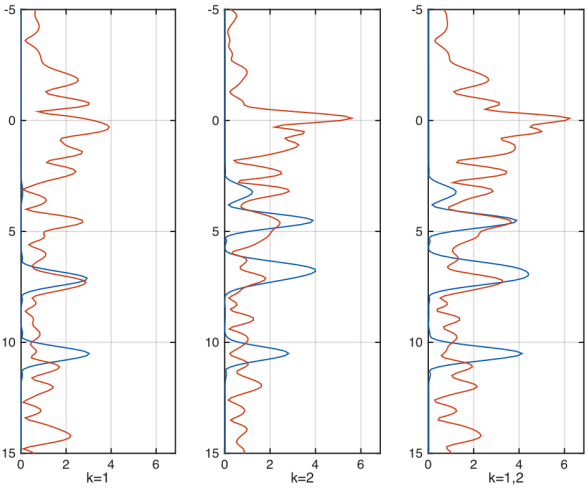

Figure C.21: *Plunge 57°*

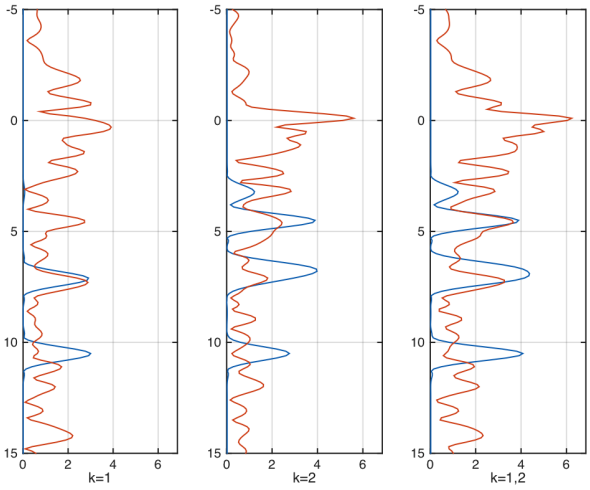

Figure C.22: *Plunge 58°*

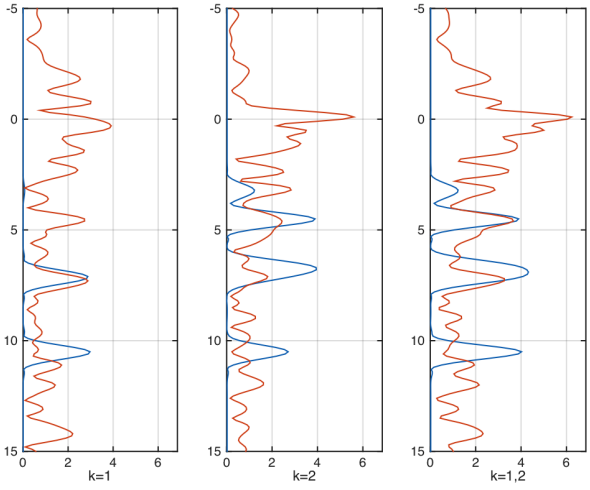

Figure C.23: *Plunge 59°*

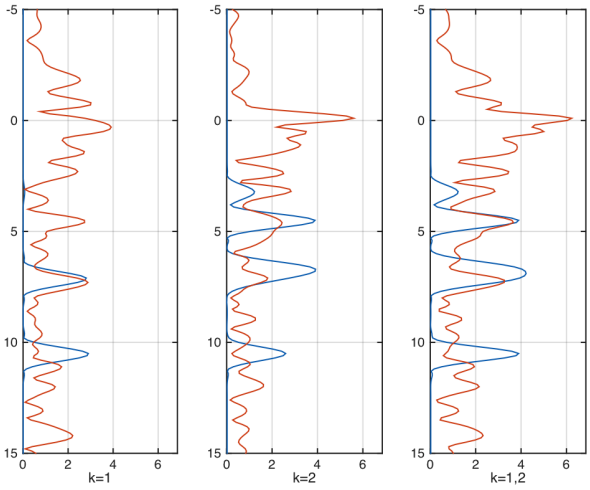

Figure C.24: *Plunge 61°*

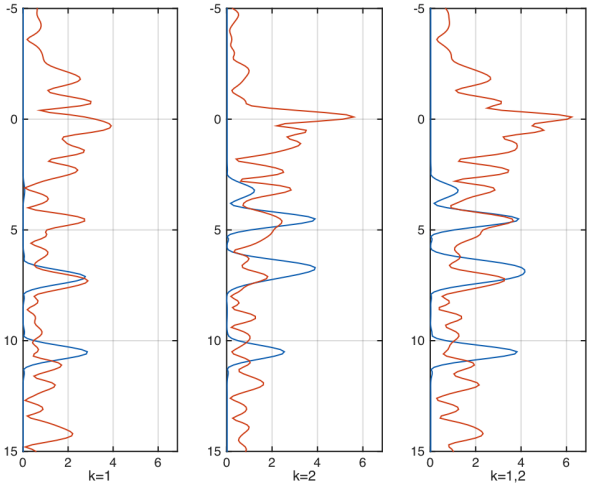

Figure C.25: *Plunge 62°*

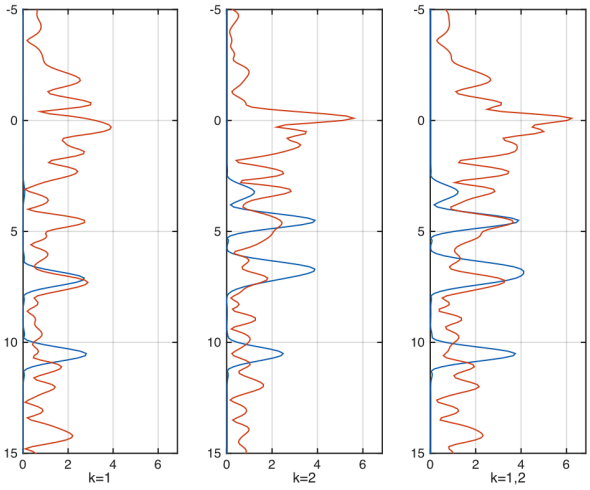

Figure C.26: *Plunge 63°*

C.5 Adding a boundary at 4.5s to the final model

Table C.7: *Including a 4.5s boundary to the final model, appearing due to change of anisotropy (Model* $N6_{8545}$*)*

Layer	**Thickness** [m]	**Vp** [m/s]	**Vs** [m/s]	ρ [kg/m^3]	**%**	**Trend**	**Plunge**
1	29500	6405	3790	2600	0	-	-
2	12500	8208	4557	3200	2	85	0
3	24000	8208	4557	3200	8	45	0
4	26450	8208	4557	3200	3	135	60
5	-	7747	4303	3200	2	45	0

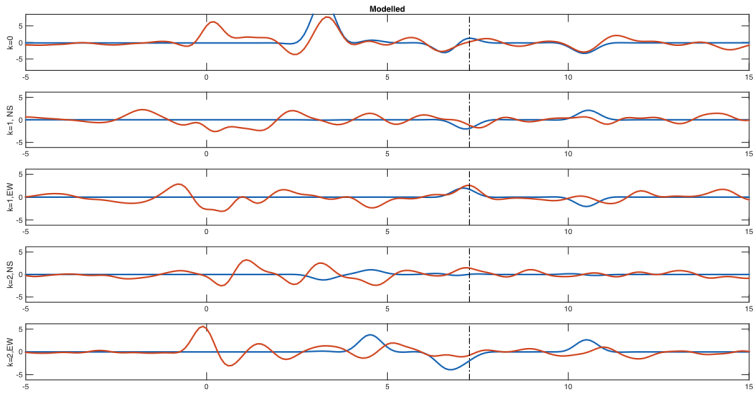

Figure C.27: $N6_{8545}$ *Harmonic decomposition*

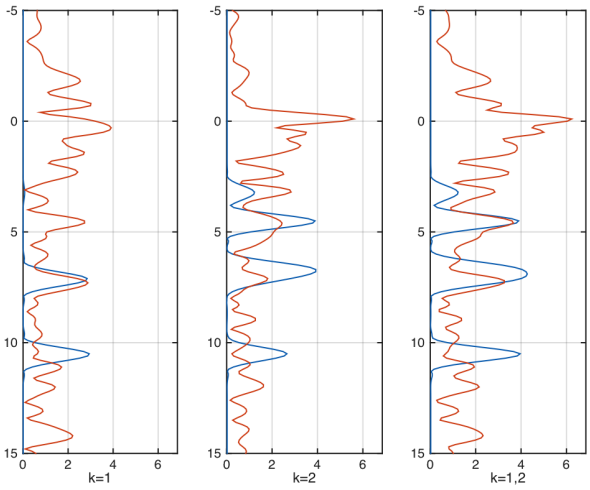

Figure C.28: $N6_{8545}$ *Full HD*

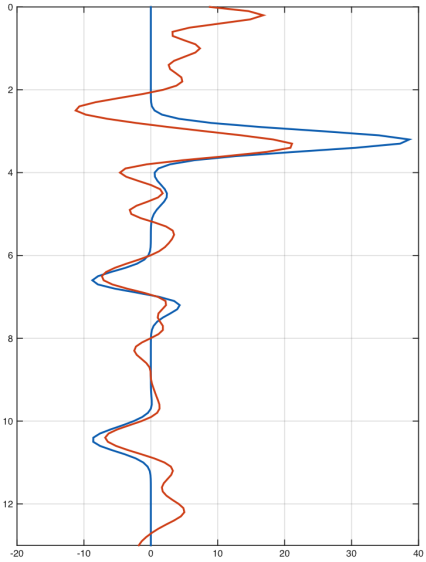

Figure C.29: $N6_{8545}$ *Radial*

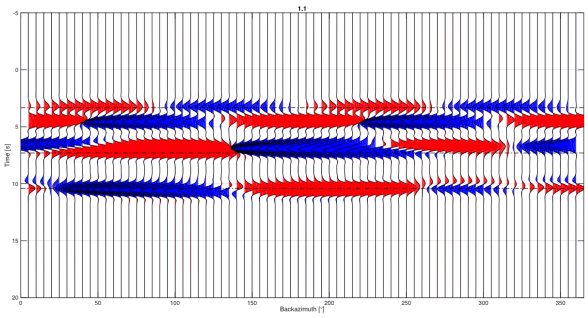

Figure C.30: $N6_{8545}$ *Transverse*